MEASUREMENTS OF KAON ELECTROPRODUCTION ON HYDROGEN AND DEUTERIUM

A Dissertation

By

JINSEOK CHA

Submitted to the Graduate College of
Hampton University
in partial fulfillment of the requirements
for the degree of

DOCTOR OF PHILOSOPHY

December 2000

This dissertation submitted by Jinseok Cha in partial fulfillment of the requirements for the degree of Doctor of Philosophy at Hampton University, Hampton, Virginia, is hereby approved by the committee under whom the work has been completed.

Benjamin Zeidman, Ph. D.
Chair

Oliver K. Baker, Ph. D.

Claudia Rankins, Ph. D.

Jörg Reinhold, Ph. D.

Rodney D. Smith, Ed.D.
Vice President for Planning and
Dean of the Graduate College

Date

ABSTRACT

Measurements of Kaon Electroproduction on Hydrogen and Deuterium

(December 2000)

Jinseok Cha, B.S., Soong-sil University at Seoul, Korea;

Ph.D, Hampton University

Chair of Advisory Committee: Dr. B. Zeidman

Kaon electroproduction for the reactions $\mathrm{H,D(e,e'K^+)}$ was studied as a function of the polar angle between the virtual photon and kaon. Coincidence measurements covered the angular range from zero to approximately 50 degrees in the $\gamma_\mathrm{v} - \mathrm{p}$ center of mass system for virtual photon momentum transfer $(Q^2) \approx$ 0.38 and 0.50 GeV^2 over a range of recoil energy, W, from approximately 1.70 to 1.97 GeV. The dependence of the cross section for $\mathrm{H(e,e'K^+)\Lambda}$ data was parameterized with kinematic variables (Q^2, W, and t), and interference terms, σ_{LT} and σ_{TT}, were determined by looking in a full coverage of azimuthal angle, ϕ. The angular dependence in the $\mathrm{D(e,e'K^+)YN}$ reaction was measured and compared with $\mathrm{H(e,e'K^+)Y}$ at the same kinematic conditions. Lambda spectrum in the missing mass spectrum was calculated in the partial wave born approximation and Jost function, and evaluated for different Λ-n potentials. The final-state interaction (FSI) between Λ and neutron for missing mass near the Lambda threshold was evaluated for different Λ-n models.

DEDICATION

Dedicated to my mom and wife.

ACKNOWLEDGMENTS

First I would like to thank my parents, Jinguy Cha and Jung-ki Lee, for the kindness and caring since the beginning.

I would like to thank my advisor, Dr. B. Zeidman, for his guidance, encouragement, kindness and patience during the entire course of this project. He has spent much of his time enduring long flights, even though his schedule was busy, in order to discuss physics and my preparation for the future. I am also appreciative to the other members of my thesis committee: Oliver K. Baker, Claudia Rankins, and Jörg Reinhold. Dr. Baker is more than a school professor and advisor to me. I really thank him for his long-term support, guidance, and encouragement. Dr. Reinhold gave me physics ideas and helped me to complete this research successfully. I am a very lucky person to have had such good teachers near me. Without them, my dissertation would not been possible.

I would like to thank the professors and postdocs at Hampton University: Keith Baker, Rolf Ent, Khin Maung Maung, Liquang Tang, Ketevi Assamagan and Paul Gueye. I also thank all the Hall C staff and postdocs: Roger Carlini, Rolf Ent, Keith Baker, Joe Beaufait, Jim Dunne, Dave Mack, Joe Mitchell, Hamlet

Mkrtchyan, Bill Vulcan, Steve Wood, and Chen Yan.

I wish to thank all the students who participated in the development of analysis routines and calibration of equipment in Hall C: Chris Armstrong, John Arrington, Chris Bochna, Dipangkar Dutta, Doug Koltenuk, Mark Harvey, Wendy Hinton, Richard Morning, Gabriel Niculescu, Ioana Niculescu, David Meekins, Bart Terburg, Alicia Uzzle, and Derek Van Westrum. I also thank my schoolmates at Hampton University: Steve Avery, Anthony Cochran, Mark Harvey, Wendy Hinton, Gabriel and Ioana Niculescu, and Alicia Uzzle.

I deeply thank the kaon farmers, all who were strongly involved in this analysis: Wendy Hinton, Doug Koltenuk, Richard Morning, Gabriel Niculescu, Jörg Reinhold and Paul Gueye. Special thanks go to Doug Koltenuk for his tremendous job on the Monte Carlo Simulation for kaon electroproduction.

Finally, but not least, I would like to thank my wife (Jungran Cho) , my daughters (Songhee and Sujung) and my son (Jamin) for understanding busy husband and dad, and for their smiles always.

Thank you all again.

TABLE OF CONTENTS

Page

LIST OF TABLES xiii

LIST OF FIGURES xvi

CHAPTER 1. INTRODUCTION AND MOTIVATION 1

1.1 $\mathrm{H}(\mathrm{e}, \mathrm{e}'\mathrm{K}^+)\mathrm{Y}$ Reaction 3

1.1.1 Formalism 3

1.1.2 Experimental Situation 7

1.2 $\mathrm{D}(\mathrm{e}, \mathrm{e}'\mathrm{K}^+)\mathrm{YN}$ Reaction 11

1.2.1 Previous Measurements 12

1.2.2 Y-N FSI in the $\mathrm{D}(\mathrm{e}, \mathrm{e}'\mathrm{K}^+)\mathrm{YN}$ Reaction 13

1.3 Organization 15

CHAPTER 2. EXPERIMENTAL APPARATUS 16

2.1 Overview 16

2.2 Accelerator and Hall C Beam Line 18

Page

2.2.1 CEBAF Accelerator 18

2.2.2 Hall C Arc and Beamline 18

2.2.3 Beam Measurements 20

2.2.4 Beam Rastering 24

2.3 Target 25

2.4 Spectrometers 28

2.4.1 High Momentum Spectrometer (HMS) 28

2.4.2 Short Orbit Spectrometer (SOS) 30

2.5 Detector Package 33

2.5.1 Drift Chambers 33

2.5.2 Hodoscopes 37

2.5.3 HMS and SOS Čerenkov 39

2.5.4 Lead Glass Calorimeter 44

2.6 Trigger 44

2.6.1 Spectrometer Triggers 45

2.6.2 Trigger Supervisor 46

2.6.3 Other Signals 48

Page

2.6.4 Data Rates 49

2.7 Data Acquisition 50

2.7.1 CODA - Physics Events 50

2.7.2 EPICS - Slow Controls 51

2.8 Kinematic setup 52

CHAPTER 3. DATA ANALYSIS 53

3.1 Overview 53

3.2 Hall C Engine 54

3.2.1 Initialization 55

3.2.2 Main Event Loop 55

3.2.3 Event Reconstruction 56

3.2.4 Output 58

3.3 Tracking 59

3.4 Reconstruction of Trajectory 59

3.4.1 Optimization of SOS Reconstruction 61

3.4.2 Optimization of HMS Reconstruction 62

3.5 Particle Identification 65

Page

3.5.1 Electrons 66

3.5.2 Aerogel Čerenkov 66

3.5.3 Coincidence Time 69

3.5.4 Hadron Beta 71

3.6 Kaon Decay Corrections 71

3.7 Absorption 75

3.8 Hodoscope Trigger Efficiencies 78

3.9 Dead Time Corrections 79

3.9.1 Electronic Dead Time 79

3.9.2 Computer Dead Time 79

CHAPTER 4. MONTE CARLO SIMULATION 81

4.1 Event Generation 81

4.2 Transport through Spectrometer 82

4.3 Radiative Corrections 83

4.4 Decay Weight 87

4.5 Weighted Yields and Cross Section 88

CHAPTER 5. PHYSICS ANALYSIS AND RESULTS 90

Page

5.1 Overview 90

5.2 $H(e,e'K^+)$ 92

5.2.1 Phase Space Distribution 93

5.2.2 Q^2, W, and t Dependence 99

5.2.3 The $H(e,e'K^+)\Lambda$ Differential Cross Section 104

5.2.4 Σ^0 Cross Section 109

5.3 $D(e,e'K^+)$ 111

5.3.1 Missing Mass Spectra 111

5.3.2 Final State Interaction 113

5.3.3 Spectra with FSI 121

5.3.4 D/H and $\mathbf{\Sigma^-/\Sigma^0}$ Ratio 129

5.3.5 Shadowing Effect 132

5.4 Discussion of Results 134

5.4.1 Proton 134

5.4.2 Deuteron 138

CHAPTER 6. SUMMARY AND CONCLUSION 140

APPENDIX A. AZIMUTHAL ANGLE (ϕ) DISTRIBUTION 149

Page

APPENDIX B. THE COMPARISON OF SOS DELTA SPECTRA . . . 155

APPENDIX C. SCATTERING PROBLEM IN P-SPACE 160

C.1 The Fortran Code for N-N scattering 164

VITA 179

LIST OF TABLES

Page

1.1 Primary exchanged particles in the Feynman diagrams, Fig. 1.2. 7

1.2 Exchanged particles and coupling constants for $K\Lambda$ channels from the models by AS [2], WJC [3], and SL [4]. 8

1.3 Exchanged particles and coupling constants for $K\Sigma$ channels from the models by MBH [5], WJC [3], and SL [4]. 9

1.4 Exchanged resonances and main coupling constants of models by AS [2, 6] MBH [5], WJC [3], and SL [4], with their broken SU(3)-symmetry values [2, 7]. 9

2.1 Hall C beam-line elements. 20

2.2 The target properties of LH2 and LD2 target under normal running conditions. 27

2.3 The properties of Aluminum targets. 28

2.4 Summary of the HMS performance. 30

Page

2.5 Summary of the SOS specifications. 32

2.6 8LM Trigger Logic. 48

2.7 Nominal kinematics for **E91-016** angular distributions for kaon electroproduction on hydrogen and deuterium targets, where $\theta_{\gamma K}^{CM}$ is for Λ production. 52

3.1 Tracking efficiencies and dead time inefficiencies. 60

3.2 Offset and modification for matrix reconstructed quantities. . . . 62

3.3 Kaon PID cut efficiencies for all settings. 64

3.4 All cuts summary table for kaon production data and SIMC. . . . 65

3.5 Comparison of normalized and efficiency corrected kaon yields within missing mass 1.1-1.14 GeVregion. 66

3.6 Table of K^+ decay channels. 72

3.7 Table of HMS materials. 76

3.8 Table of SOS materials. 77

3.9 Kaon absorption in the SOS [43]. 78

5.1 The mean kinematic values for $H(e, e'K^+)\Lambda$ for $1.74 < W < 1.80$ GeV. 93

Page

5.2 Comparison of the charge normalized yield for Λ production between the SOS delta normal and low settings for $1.74 < W < 1.80$ GeV. 95

5.3 Binned Λ cross sections for all angles at $Q^2 = 0.5$ GeV^2 for the $P_{SOS} = 1.077$ GeV/c settings for hydrogen. 99

5.4 Binned Λ cross sections for all angles at $Q^2 = 0.5$ GeV^2 for the $P_{SOS} = 0.929$ GeV/c settings for hydrogen. 100

5.5 Binned Λ cross sections for all angles at $Q^2 = 0.38$ GeV^2 settings for hydrogen. 101

5.6 Cross sections at central kinematics for Λ production on hydrogen. 104

5.7 The parameter values after fit. 106

5.8 Σ° cross sections at central kinematics for hydrogen. 109

5.9 The parameters for the various potentials used in Eq. 5.11. 115

5.10 The phase shift calculation results for different models. 119

5.11 Cross sections for Kaon electroproduction on deuterium. 129

LIST OF FIGURES

Page

1.1 Simplified diagram of $\mathrm{H(e, e'K^+)Y}$ Reaction. 3

1.2 Extended Born terms Feynman diagrams for the $\mathrm{p(e, e'K^+)Y}$ reaction. 6

1.3 W dependence of previous data [1] on $p(\gamma K^+)\Lambda$ Reaction. 10

2.1 CEBAF Accelerator. 17

2.2 Schematic of the Hall C arc and beamline. 19

2.3 Schematic of a Hall C superharp system. 21

2.4 Schematic of the Hall C Cryotarget Cell Block Stack. 26

2.5 Side view of the HMS. 29

2.6 Side view of the SOS. 31

2.7 Schematic diagram of the HMS detector hut. 34

2.8 Schematic diagram of the SOS detector hut. 35

2.9 Hodoscope electronics. The numbers indicate the number of channels used in the HMS/SOS. 38

Page

2.10 Cross section of aerogel detector. Total 14 PMT, 7 for each side, are connected. 41

2.11 HMS gas and SOS aerogel Čerenkov Electronics. 43

2.12 HMS/SOS single arm trigger electronics. 46

2.13 Trigger Supervisor Electronics. 49

3.1 Comparison of normalized yield with and without aerogel trigger. With this hardware cut, the number of photoelectrons in aerogel Čerenkov ≤ 7, was applied online and reduced the trigger rate by ~ 35 %. 67

3.2 Kaon inefficiency distributions with aerogel software cut, for fewer than 3 photoelectrons. 68

3.3 Real and random events in path-length corrected coincidence time. 70

3.4 Kaon decay rate within hut. 73

3.5 Beta vs. momentum for π, μ, and K^+. 74

4.1 Feynman diagrams for the internal soft corrections processes contributing to the measured cross section. 84

Page

4.2 Feynman diagrams for the internal hard corrections. 85

4.3 Radiated photon distribution for r=0.09, normalized such that the frequency at $\omega = 1$ is equal to one. 87

5.1 Raw missing mass spectra for real and background events for $H(e,e'K^+)Y$(top) and $D(e,e'K^+)YN$(bottom). 91

5.2 W vs. Q^2 coverage for $H(e,e'K^+)\Lambda$ data. 92

5.3 W vs. $\theta_{\gamma,K}$ phase space distributions at $Q^2 = 0.5$ GeV^2. 94

5.4 Comparison of the ϕ distributions between the SOS normal ($P_{SOS} = 1.077$ GeV/c) and low ($P_{SOS} = 0.929$ GeV/c) settings at $Q^2 = 0.5$ GeV^2 for $1.74 < W < 1.80$ GeV. 96

5.5 Comparison of the δ_{SOS} distribution between the SOS normal ($P_{SOS} = 1.077$ GeV/c) and low ($P_{SOS} = 0.929$ GeV/c) settings at $Q^2 = 0.5$ GeV^2 for $1.74 < W < 1.80$ GeV from our Monte Carlo simulation. 97

Page

5.6 Comparison of the cross section between $P_{SOS} = 1.077$ and $P_{SOS} = 0.929$ GeV/c settings for the same W and Q^2 cuts which correspond to mean values of $\bar{W}$ =1.77 GeV and $\bar{Q}^2 = 0.513$ GeV^2 for all points. 98

5.7 $H(e, e'K^+)\Lambda$ cross section W dependence for a narrow Q^2 cut after scaling to $t = t_{min}$. 102

5.8 $H(e, e'K^+)\Lambda$ cross section angular dependence without scaling. . . 103

5.9 Angular dependence of $H(e, e'K^+)\Lambda$ cross section. 105

5.10 Q^2 (top) and W (bottom) dependences of the $H(e, e'K^+)\Lambda$ cross section. 107

5.11 t (top) and ϕ (bottom) dependences of the $H(e, e'K^+)\Lambda$ cross section. 108

5.12 $H(e, e'K^+)\Sigma^0$ cross section; data (top) and MC simulation (bottom). 110

5.13 The missing mass spectra from data (points with error bars) and MC simulations (solid lines) for $D(e, e'K^+)YN$ reactions. The sum of the three simulations is the line through the data. 112

Page

5.14 Λ-n FSI influence factors for three different models. 120

5.15 $D(e,e'K^+)YN$ missing mass spectra of data and simulation with and without FSI for set numbers 1–4 as defined in Table 2.7 at $Q^2 \approx 0.5$ GeV^2. 123

5.16 $D(e,e'K^+)YN$ missing mass spectra of data and simulations with and without FSI for set numbers 9–11 as defined in Table 2.7 at $Q^2 \approx 0.38$ GeV^2. 124

5.17 Comparison of the three different Λ-n FSI models, mentioned in Table 5.9, with data near the threshold of Λ production on deuterium. 125

5.18 The measured Λ-n FSI influence factor from data as a function of missing mass (top) and relative Λ-n momentum (bottom) 126

5.19 Simple spin diagram for $D(e,e'K^+)\Lambda n$ reaction. 127

5.20 $D(e,e'K^+)YN$ missing mass plot with FSI MC simulation for $Q^2 = 0.38$ GeV^2 forward settings. 128

5.21 The cross section ratios between $H(e,e'K^+)\Lambda$ and $D(e,e'K^+)\Lambda$n for the setting in Table 5.11. 130

Page

5.22 Σ^-/Σ^0 cross sections for deuterium, where the Σ^0 cross sections are obtained from the free proton. 131

5.23 Schematic model of deuteron. 132

5.24 The Q^2 dependence of the unpolarized differential cross section for the reaction $\gamma^{(*)} + p \rightarrow K^+ + \Lambda$. 137

5.25 The remainder of the missing mass spectrum for two different Q^2 settings after the Monte Carlo simulations including FSI of $D(e,e'K^+)YN$ were subtracted from data. 139

A.1 ϕ distributions of Λ production for the four different angle settings at $P_{SOS} = 1.077$ GeV/c and $Q^2 = 0.50$ GeV^2. 151

A.2 ϕ distributions of Λ production for the four different angle settings at $P_{SOS} = 0.929$ GeV/c and $Q^2 = 0.50$ GeV^2. 152

A.3 ϕ distributions of Λ production for the three different angle settings at $Q^2 = 0.38$ GeV^2. 153

A.4 ϕ sum distributions of $P_{SOS} = 1.077$ and 0.929 GeV/c settings at $Q^2 = 0.50$ GeV^2. 154

Page

B.1 SOS delta, $\frac{P-P_0}{P_0}$, comparisons of data and MC for set numbers 1–4 as defined in Table 2.7 for $Q^2 = 0.50$ GeV^2 settings. 157

B.2 Figures similar to Fig. B.1, for set numbers 5–8, $Q^2 = 0.50$ GeV^2 settings. 158

B.3 Figures similar to Fig. B.1, for set numbers 9–11, $Q^2 = 0.38$ GeV^2 settings. 159

CHAPTER 1

INTRODUCTION AND MOTIVATION

Nuclei are complex media composed of nucleons, mesons, and other virtual particles. In turn, the structure of the various hadrons is described in terms of quarks, gluons, and their symmetries through quantum chromodynamics (QCD). Understanding the nucleon-nucleon interaction in the medium is one of the most significant objectives of nuclear physics. To investigate baryonic interactions in the nuclear many body system, it is necessary go beyond the simple nucleon description and utilize other members of the baryon mutiplet, namely the Λ and Σ hyperons, the lightest baryons that contain a strange quark. The flavor SU(3) triplet contains u-, d- and s-quarks, while ordinary matter is built solely of u- and d-quarks. Few body systems, D and ^{3,4}He, limit the complexity of possible interactions and provide information in systems that are amenable to detailed theoretical calculations that can elucidate features of hyperon-nucleon interactions in the nuclear medium. In order to have a comprehensive understanding of the strong interactions resulting from the additional degree of freedom (strangeness), there are several ways to investigate hyperon-nucleon interactions. One is to study the strangeness exchange reactions (K^-, π^-) or (π^+, K^+) which, because of complex pion interactions, makes it difficult to extract details of the underlying potential.

Another is a direct measurement of hyperon-nucleon scattering which is precluded by the difficulty of obtaining hyperon beams. Experiment **E91-016** is intended to be the initial step in a program that will provide basic data needed to obtain this information.

The Kaon (K meson) is the lightest hadron with constituent strangeness; i.e. to fully explain its existence and basic properties, the "strange" (**s**) quark must be part of the quark-antiquark pair. Although discovered in the first half of the 20-th century and studied ever since, the production mechanism for kaons is not well understood. In particular, determination of the kaon electroproduction cross-section on complex nuclei has not been possible because of the low duty factor of available electron accelerators. Experiment **E91-016** was designed to take advantage of the performance of the Jefferson Lab continuous wave (**CW**) electron beam and provide a detailed study of elementary K^+ electroproduction in both the reactions

$$e + p \longrightarrow e' + K^+ + Y \tag{1.1}$$

and

$$e + d \longrightarrow e' + K^+ + Y + N, \tag{1.2}$$

where Y can be a Λ, Σ^0, or Σ^-.

Electron scattering is a useful tool for studying nuclear structure and, given enough incident energy, the structure of nucleons themselves. The interaction in electron scattering, the electromagnetic interaction, is well understood and produces minimal disturbance to the target when compared with other means of investigation such as hadronic probes.

1.1 $\mathrm{H(e, e'K^{+})Y}$ Reaction

1.1.1 Formalism

The elementary process of kaon electroproduction is illustrated briefly in the Fig. 1.1. In this figure,

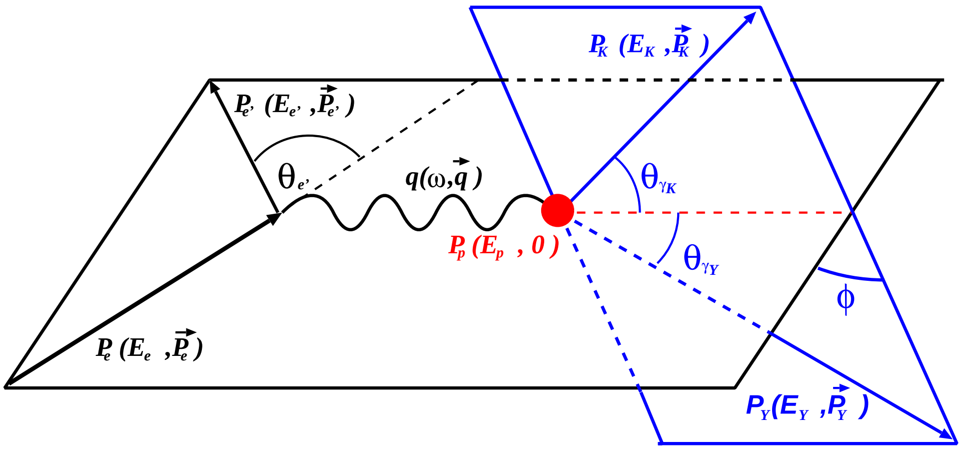

Figure 1.1: Simplified diagram of $\mathrm{H(e, e'K^{+})Y}$ Reaction.

- P_e and $P_{e'}$ are the four momenta of incoming and outgoing electron, respectively,

- q is the four momentum transfer to the target with energy, ω, and three momentum, $\vec{q}$, i.e. the virtual photon,

- θ_e is the scattering angle of electron,
- P_K is the four momentum of kaon,
- $\theta_{\gamma K}$ is the kaon scattering angle w.r.t. $\vec{q}$,
- the Lorentz invariant quantities are

$$q^2 = -Q^2 = (P_e - P_{e'})^2, \tag{1.3}$$

$$s = W^2 = (q + M_p)^2, \tag{1.4}$$

$$t = (q - P_{K^+})^2, \tag{1.5}$$

In the center-of-mass system, the cross section for electroproduction, Eq. 1.1, can be expressed [3] as

$$\frac{d\sigma}{d\Omega^*} = \frac{|\vec{P}_k|}{|\vec{q}|}\frac{M_p M_Y}{16\pi^2 s} < |\mathcal{T}_{fi}|^2 >, \tag{1.6}$$

where * indicate the c.m., $< |\mathcal{T}_{fi}|^2 >$ is defined to be the averaged square amplitude, and M_p and M_Y are the mass of proton and hyperon, respectively. In the Eq. 1.6

$$\frac{|\vec{P}_k|}{|\vec{q}|}\frac{M_p M_Y}{16\pi^2 s} \tag{1.7}$$

is equivalent to the phase space factor. The $< |T_{fi}|^2 >$ factor can be re-expressed [3] as

$$
\begin{aligned}
< |T_{fi}|^2 > \;&=\; \sum_{\lambda,\lambda'}[\frac{1}{2}(|H_x|^2 + |H_y|^2) + \varepsilon_L|H_z|^2 + \frac{\varepsilon}{2}(|H_x|^2 - |H_y|^2) \\
&\quad -\sqrt{2\varepsilon_L(\varepsilon+1)}(H_x{}^*H_z + H_xH_z{}^*)], \qquad (1.8)
\end{aligned}
$$

where H_x, H_y, and H_z are the components of hadronic current in x, y, and z directions, respectively.

Quantum electrodynamics, QED, which describes the electromagnetic interaction, is the most accurate physical theory extant [9]. The elementary cross section, Eq. 1.6, for electroproduction in the center-of-mass system can be rewritten as

$$
\begin{aligned}
\frac{d\sigma}{d\Omega^*}(Q^2, W, t) \;&=\; \frac{d\sigma_T}{d\Omega^*} + \varepsilon_L\frac{d\sigma_L}{d\Omega^*} + \sqrt{2\varepsilon_L(\varepsilon+1)}\sin\theta^*_{\gamma K}\cos\phi\frac{d\sigma_{LT}}{d\Omega^*} \\
&\quad +\varepsilon\sin^2\theta^*_{\gamma K}\cos 2\phi\frac{d\sigma_{TT}}{d\Omega^*} \qquad (1.9)
\end{aligned}
$$

where

$$
\varepsilon = \frac{1}{1 + 2\frac{|\vec{q}|^2}{Q^2}\tan^2\frac{\theta_{e'}}{2}}, \qquad (1.10)
$$

$$
\varepsilon_L = \frac{Q^2}{\omega^2}\varepsilon, \qquad (1.11)
$$

and the kinematic variables are defined in Fig. 1.1. ε and ε_L are the virtual photon degree of transverse and longitudinal polarization, respectively, σ_T is the cross section for an unpolarized incident photon beam, and the σ_{TT} term is the asymmetry contribution of a transversely polarized beam. σ_L is the cross section contributed by longitudinal components of the virtual photon and σ_{LT} is due to interference effects between longitudinal and transverse components. All cross section terms can be written as functions of Q^2, W, and t. Coincidence kaon electroproduction from the nucleon can be calculated with the use of the effective Lagrangian approach that contains Born terms and resonance contributions. The cross sections σ_{TT} and σ_{TL} may be very sensitive to the resonance contributions [10]. Fig. 1.2

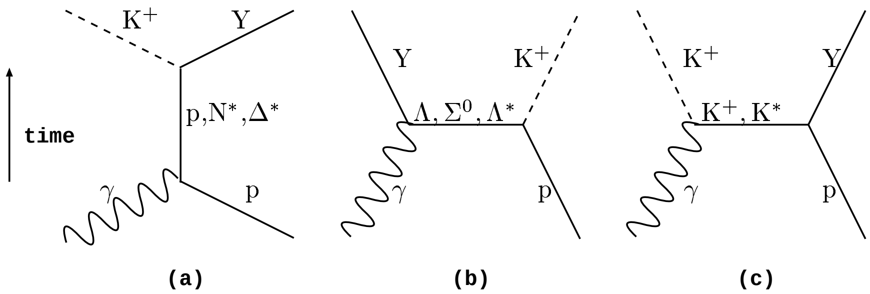

Figure 1.2: Extended Born terms Feynman diagrams for the $p(e, e'K^+)Y$ reaction. (a), (b), and (c) are s-, u-, and t-channel exchanges, respectively.

show the three different channel (s, u, and t) Feynman diagrams for a $p(e, e'K^+)Y$ reaction. In these exchange Born term diagrams, s-, u-, and t-channel are determined by whether the propagator is a baryon (p, N^*, or Δ^*), a strange baryon $(\Lambda, \Sigma^0, or \Lambda^*)$, or a strange meson ($K^+$, K^*). The exchanged particles considered in the p(e, e′K$^+$)Y reaction are listed in Table 1.1. Each vertex in these diagrams is associated with a particular coupling constant. The coupling constants used in several isobaric models are listed for comparison in Table 1.2 and 1.3. The various isobaric models share the property that they initially include only spin 1/2 baryonic resonances (although the specific resonances differ, referenced in Table 1.4) and determine the remaining coupling constants by performing phenomenological fits to the data. The differences arise not only because of variation in theoretical frameworks, but also due to the lack of available experimental data.

Notation	Particle	(I)J^π	Mass (MeV)	Width (MeV)
	p	$(\frac{1}{2})\ \frac{1}{2}^+$	938.272	
	K$^+$	$(\frac{1}{2})\ 0^-$	493.677	
	Λ	$(0)\ \frac{1}{2}^+$	1115.68	
	Σ^0	$(1)\ \frac{1}{2}^+$	1192.55	
K*	K*(892)	$(1)\ 1^-$	891.59	49.8
K1	K1(1270)	$(\frac{1}{2})\ 1^+$	1273.0	90.0
N1	N(1440)	$(1)1/2^+$	1440	350
N4	N(1650)	$(0)1/2^-$	1650	150
N6	N(1710)	$(1)1/2^+$	1710	100
N7	N(1720)	$(1)3/2^+$	1720	150
L1	Λ(1405)	$(0)1/2^-$	1405	50
L3	Λ(1670)	$(0)1/2^-$	1670	35
S1	Σ(1660)	$(1)1/2^+$	1660	100

Table 1.1: Primary exchanged particles in the Feynman diagrams, Fig. 1.2.

1.1.2 Experimental Situation

E91-016 includes the coincidence measurement of the H(e, e′K$^+$)Y reaction with high statistics and complements data from experiment **E93-018**. Prior to

Particle	Coupling	AS	WJC	SL
Λ	$\mathrm{g_{K\Lambda N}}/\sqrt{4\pi}$	-4.17±0.75	-2.38	-3.16±0.01
Σ	$\mathrm{g_{K\Sigma N}}/\sqrt{4\pi}$	1.18±0.66	0.27	0.91±0.10
K*	$G_V/4\pi$	-0.43±0.07	-0.16	-0.05±0.01
	$G_T/4\pi$	0.20±0.12	0.08	0.16±0.02
K1	$G_{V1}/4\pi$	-0.10±0.06	0.02	-0.19±0.01
	$G_{T1}/4\pi$	-1.21±0.33	0.17	-0.35±0.03
N1	$G_{N1}/\sqrt{4\pi}$	-1.42±0.60		-0.01±0.12
N4	$G_{N4}/\sqrt{4\pi}$		-0.04	
N6	$G_{N6}/\sqrt{4\pi}$		-0.06	
N7	$G^a_{N7}/4\pi$			-0.04±0.01
	$G^b_{N7}/4\pi$			-0.14±0.04
	$G^b_{N8}/4\pi$			-0.05±0.56
L1	$G_{L1}/\sqrt{4\pi}$		-0.07	-0.31±0.06
L3	$G_{L3}/\sqrt{4\pi}$	-3.17±0.86		1.18±0.09
S1	$G_{S1}/\sqrt{4\pi}$			-4.96±0.19

Table 1.2: Exchanged particles and coupling constants for $K\Lambda$ channels from the models by AS [2], WJC [3], and SL [4].

Particle	Coupling	MBH	WJC	SL
Λ	$g_{K\Lambda N}/\sqrt{4\pi}$	0.51	-2.38	-3.23±0.17
Σ	$g_{K\Sigma N}/\sqrt{4\pi}$	0.13	0.27	0.80±0.10
K^*	$G_V/4\pi$	0.05	0.11	0.02±0.01
	$G_T/4\pi$	0.05	-0.14	-0.07±0.02
K1	$G_{V1}/4\pi$		-0.13	-0.05±0.01
	$G_{T1}/4\pi$		0.07	0.23±0.04
N1	$G_{N1}/\sqrt{4\pi}$			-0.95±0.11
N4	$G_{N4}/\sqrt{4\pi}$	0.08	0.09	
N6	$G_{N6}/\sqrt{4\pi}$	0.57	0.47	
N7	$G^a_{N7}/4\pi$			-0.04±0.02
	$G^b_{N7}/4\pi$			-0.53±0.06
L1	$G_{L1}/\sqrt{4\pi}$		0.46	-0.42±0.03
L3	$G_{L3}/\sqrt{4\pi}$			-1.10±0.09
S1	$G_{S1}/\sqrt{4\pi}$			-1.72±0.21

Table 1.3: Exchanged particles and coupling constants for $K\Sigma$ channels from the models by MBH [5], WJC [3], and SL [4].

Theory	s-channel	u-channel	t-channel	$g_{K\Lambda N}/\sqrt{4\pi}$	$g_{K\Sigma N}/\sqrt{4\pi}$
AS	N1	L3	K^*, K^1	-4.17±0.75	1.18±0.66
WJC	N4,N6,D1,D2,D3	L1	K^*, K^1	-2.38	0.27
MBH	N4,N6,D2,D3	-	K^*	0.51	0.13
SU(3)				-3.7±0.7	1.1±0.2

Table 1.4: Exchanged resonances and main coupling constants of models by AS [2, 6] MBH [5], WJC [3], and SL [4], with their broken SU(3)-symmetry values [2, 7].

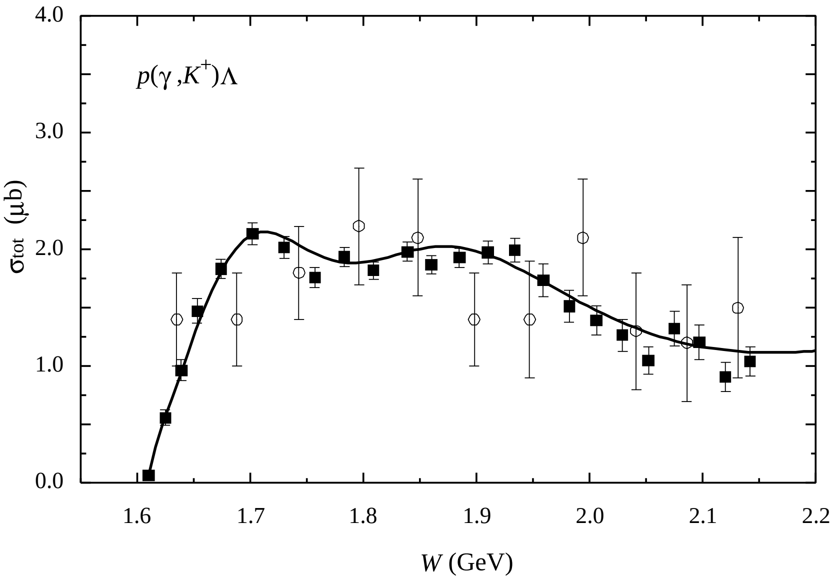

Figure 1.3: W dependence of previous data [1] on $p(\gamma K^+)\Lambda$ Reaction.

these experiments kaon data on hydrogen were sparse. Most of the data were taken before 1980 with poor statistics and resolutions ([12], [13], and [1] etc.). All of the data, electro- and photo-production, were obtained with W greater than $\sim$ 1.9 GeV, except SAPHIR photo-production which is shown in Fig. 1.3. The data have some enhancement at $W \sim 1.7$ GeV.

Experiment, **E93-018**, run during the same time period as **E91-016**, has already published the separated cross sections for σ_T and σ_L at $Q^2 \sim 0.5$ GeV^2, the Q^2 point common to both experiments, and other values of Q^2 [11]. Therefore, the evaluation and extraction of remaining two terms of the cross section provides full understanding of kaon electroproduction cross sections at these specific kinematics.

1.2 $\mathrm{D(e,e'K^+)YN}$ Reaction

The deuteron is the simplest complex nucleus. It is a very weakly bound two-body system consisting of a proton and a neutron. Therefore, in reactions with sufficiently high momentum transfer, the nucleons can be regarded as almost free particles. This feature is explored in a number of experiments which use deuterium targets as a laboratory to study the properties of the neutron. Thus, properly treated, kaon electroproduction on deuterium should allow the extraction of the reaction mechanism on the neutron. The initial momenta (Fermi motion) of the proton and the neutron inside the deuteron are equal and opposite to each other. The quasi-free assumption can be tested by direct comparison of Λ production from deuterium and hydrogen. The weak binding in the deuterium nucleus, and hence low Fermi momentum, still leaves the two distinct reaction channels for producing a Λ- or Σ hyperon separable from each other. Using the impulse approximation, we expect the cross sections for Λn and Σ^0n to have the same kinematic (W, Q^2, and t) dependences as the corresponding Λ and Σ cross sections for hydrogen. The mass of the two nucleons in the deuteron are off-shell, the mass being less than the rest mass of the nucleon. The particles in final states, however, are assumed to be on-shell. The off-shell effects are less than 3 % of the total cross section strength [14]. The basic form [14] of the formula comparing deuterium cross sections to elementary hydrogen cross sections is

$$d\sigma_{deuterium} = d\sigma_{hydrogen}(1 + \beta_n \cos\theta_n)|\Psi(\vec{p_n})|^2 d^3p_n, \tag{1.12}$$

where Ψ is the deuterium wave function and β_n represents the velocity of the spectator in the lab frame. The effect of this term is expected to be small for kaon photo-production [15].

Recently, it has been suggested to measure Λ-n interactions via the final-state interaction in $D(\gamma K^+)$, and $D(e, e'K^+)$ reactions. There are theoretical predictions for the final-state Λ-n interaction with various models. In this experiment we study the hyperon-nucleon interaction in the frame-work of the final-state interactions (FSI) [14].

1.2.1 Previous Measurements

To our best knowledge, the only previous measurement of kaon electroproduction on deuterium was performed about 25 years ago with very poor statistical accuracy and resolution [12] even in hydrogen. There are two more measurements, [16] and [17], of kaon photo-production on deuterium. All previous measurements have published poorly reproduced missing mass spectra from hydrogen data only. The results are not consistent between electro-production and photo-production, even though the two photo-production results are close, but not within errors. The two photo-production experiments presented their measurments of the

Σ ratio of deuterium to hydrogen with dubiously small errors, < 10 %, in contrast to the quality of data; even the resolution of hydrogen is poor. These previous publications have never shown the missing mass spectra on deuterium. The angular dependence of kaon electroproduction on deuterium had never been measured.

In photoproduction experiments, [16] and [17], Boyarski found the ratio of Λ cross sections on deuterium and hydrogen to be $1.02 \pm 0.04 \pm 0.05$, consistent with a simple absorption model estimate of 0.96. The ratio of Σ cross sections on deuterium to those on hydrogen was found to be $2.37 \pm 0.11 \pm 0.12$ in Boyarski's and 2.73 ± 0.18 in Quinn's. Both experiments claimed the result to be consistent with the calculated result, 2.87, which assumed the reaction was dominated by pure isospin-$\frac{1}{2}$ exchange with simple absorption corrections. These results did not agree with Bebek's numbers [12]. Because of the poor quality and discrepancies in the previous data, theorists hesitate to fit the data. Consequently, the existing models can have very different predictions for charged Σ production. **E91-016** presents the first precise measurement for Σ hyperon production on the neutron.

1.2.2 Y-N FSI in the $\mathrm{D(e,e'K^+)YN}$ Reaction

The possible final-state interactions of kaon electroproduction reactions on deuterium can be K-Y, K-N, Y-N, and K-Y-N as combinations of the three final particles (K, Y, and N) shown in the right-hand side of Eq. 1.2. Since the interaction between K and Y is already present in hydrogen, it can be ignored. The

K-N interaction, between kaon and spectator nucleon, is small ([18], [19], and [20]) compared to the Y-N interaction which is most dominant in the FSI. There is no investigation of possible K-Y-N interactions in the final state. Therefore, our work will concern the FSI due to Y-N scattering; i.e. Λ-n, Σ^0-n, or Σ^--p.

There are several theoretical papers, such as [8] and [14], introducing the final-state Λ-n interaction. Some of models, mentioned in the papers, already parameterize hyperon-proton scattering on the basis of the existing, inadequate photo production data. Among them, X. Li and L. E. Wright [8] have discussed Λ-n FSI in photo-production with three different potential models. Each model is again associated with two different spin states, singlet and triplet. These models have quite different scattering lengths and effective ranges. Since, generally, the N-N interaction has a maximum value at low relative momentum, there is strong enhancement near the Λ threshold. However, they claim that the Λ-n FSI causes a significant enhancement for the exclusive measurement, $D(\gamma, K^+\Lambda)n$ near threshold, but is not as significant for the inclusive process, $D(\gamma, K^+)\Lambda n$, the current measurement.

There are few direct measurements of hyperon-nucleon interactions, and these involved at least one charged particle. There is no data as yet for the neutral hyperon-n interaction, even though there are many theoretical predictions. The present experiment is the first reasonable measurement for the hyperon-nucleon FSI and allows evaluation of the existing theoretical models for Λ-n FSI. Since the

Σ is an isospin-1 hyperon, the Σ can interact strongly with nucleons via one pion exchange in contrast to the Λ that cannot exchange isospin-1. In this case, the Σ-N FSI in the intermediate state can be much stronger than that in Λ-n. In addition, we might expect a Σ^--p bound state because of the Coulomb attraction [54].

One very important benefit of obtaining high quality precision measurements for kaon electroproduction on deuterium is not only understanding of the additional interactions contributed by the quantum number, s, but also the additional possibility of charged hyperon-nucleon interactions in the Coulomb field.

1.3 Organization

In the following discussions, the experimental facilities, analysis techniques, Monte Carlo simulations and results will be discussed in Chapters 2, 3, and 4, respectively. Data analysis and results will be represent in Chapter 5 and summarized in Chapter 6.

CHAPTER 2

EXPERIMENTAL APPARATUS

2.1 Overview

Experiment **E91-016**, "Electroproduction of Kaons on Hydrogen and Deuterium", performed at Jefferson Lab in 1996, was carried-out in Hall C, the only operational experimental area at that time.

During **E91-016** the scattered electrons were detected in coincidence with the leptoproduced kaons, detected before their in-flight decay. The data have been taken with the 4-cm hydrogen, deuterium and aluminum dummy targets for the background measurement. A number of single events were also recorded for both the electron and the hadron arm. Elastic scattering off hydrogen (using the same target cell as in the experiment) was measured for calibration purposes.

The experimental equipment used in **E91-016** was the standard equipment available in Hall C consisting of

- target assembly (this includes the targets themselves);
- a pair of focusing electromagnetic spectrometers, namely:
  - the High Momentum Spectrometer (**HMS**),

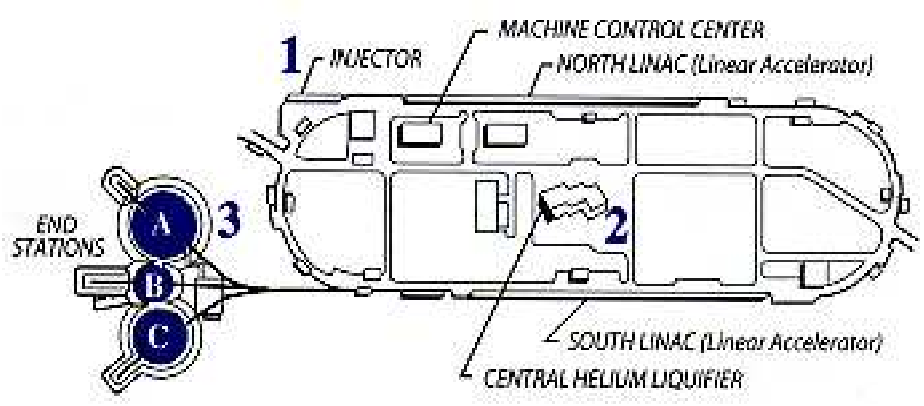

Figure 2.1: CEBAF Accelerator.

– and the Short Orbit Spectrometer (**SOS**).

Each one these spectrometers has its own set of detectors comprised of:

* Drift chambers,
* Scintillator hodoscopes,
* Gaseous and solid Čerenkov counter,
* Shower counter.

In order to address the specific problems related to kaon detection, two additional Čerenkov counters, Lucite and Aerogel, were added to the hadron arm detector stack. However, only the Aerogel Čerenkov counter was used for the trigger mentioned in Sec. 2.6. The systems enumerated above will be described in the rest of this chapter and have also been discussed previously [21], [22], and [23].

2.2 Accelerator and Hall C Beam Line

2.2.1 CEBAF Accelerator

The CEBAF accelerator, shown schematically in Fig. 2.1, is a high-intensity, continuous wave (**CW**) electron accelerator. The microstructure of the beam consists of short (1.67 ps) bursts of beam at 1497 MHz. Each of three experimental halls receives every third of these bursts, for an "effective" frequency of 499 MHz in each hall. Typical beam emittance was around 2×10^{-9} m·rad, with an energy spread, $\Delta E/E$, of 10^{-4}. The relative beam energy can be measured to 10^{-4} and is known absolutely to 10^{-3} deviation. During the data acquisition period of Experiment **E91-016**, Jefferson Lab provided unpolarized, **CW** electron beams with energies in the 2.445–3.245 GeV range, and currents between 10 and 30 μA.

Finally, the accelerated beam was transported to the experimental Hall C through the beam switch yard.

2.2.2 Hall C Arc and Beamline

The Hall C 41.6 m arc beamline consists of 8 dipoles, 12 quadrupoles, 8 sextupoles, and 8 pairs of beam correctors, which transport the beam from the beam switch yard to the target. The total deflection angle of the arc is 34.3 degrees. The arc is also equipped with several monitors to measure the energy, current, position, and profile of the beam. Fig. 2.2 shows the hardware in the Hall C Arc and beamline.

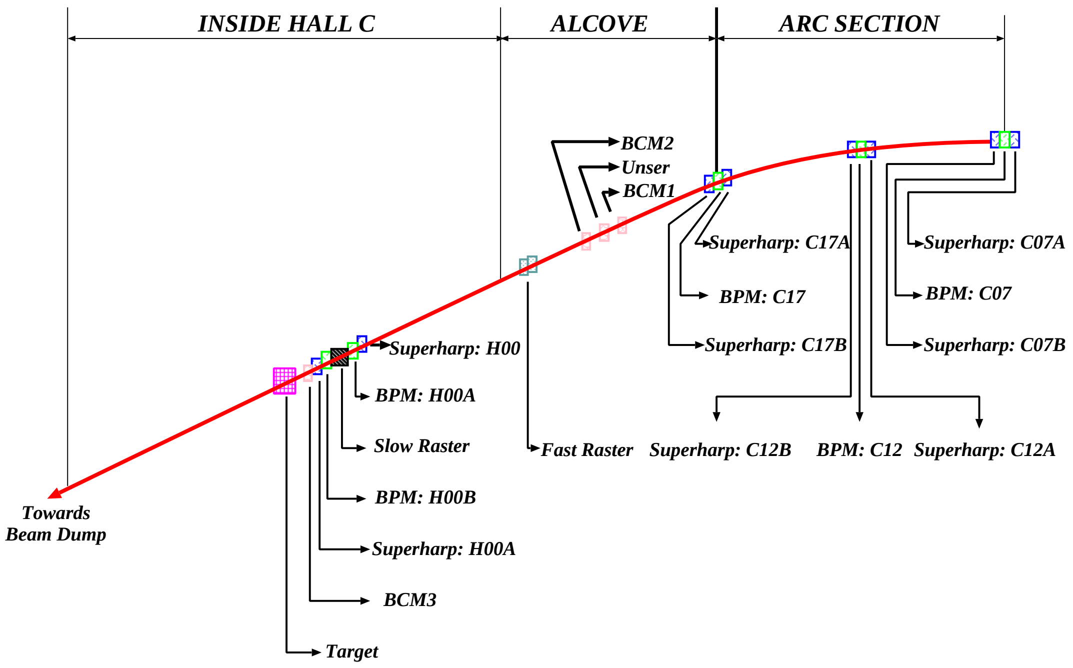

Figure 2.2: Schematic of the Hall C arc and beamline.

In the Hall C arc, there are three pairs of superharps (described in Sec. 2.2.3), which are used for beam energy measurement and to measure the beam profile for machine operation. Each pair of superharps is located at the beginning, the mid-point, and the end of Hall C arc. These superharps provide the position and orientation of the incident electron beam at the given location. Using this information, the bending trajectory of beam within the arc dipoles is determined. From this trajectory, the energy of beam can be calculated with the field maps of the arc bending magnets.

In the Hall C beamline, two additional superharps (H00 and H00A) and two beam position monitors (BPM:H00A and BPM:H00B) (described in Sec. 2.2.3) were located close to the target. The distances from the target are shown in Table 2.1.

Element	Name	Distance from target (m)
BPM	H00A	3.445
BPM	H00B	1.637
Superharp	H00	3.290
Superharp	H00A	1.473

Table 2.1: Hall C beam-line elements.

2.2.3 Beam Measurements

Precise information, such as energy and intensity (current), of the incident electron beam is needed for accurate physics measurements. The energy of incident beams is calculated from the BPM information at the Hall C arc, as mentioned briefly in the previous section. The intensity of beam was measured using three devices, a Unser monitor and two beam current monitors (BCM, discussed in next subsection).

Beam Position Monitors

The position of the beam in Hall C was monitored using four beam position monitors (BPM), which are shown in Fig. 2.2 and Table 2.1. A harp consists of a

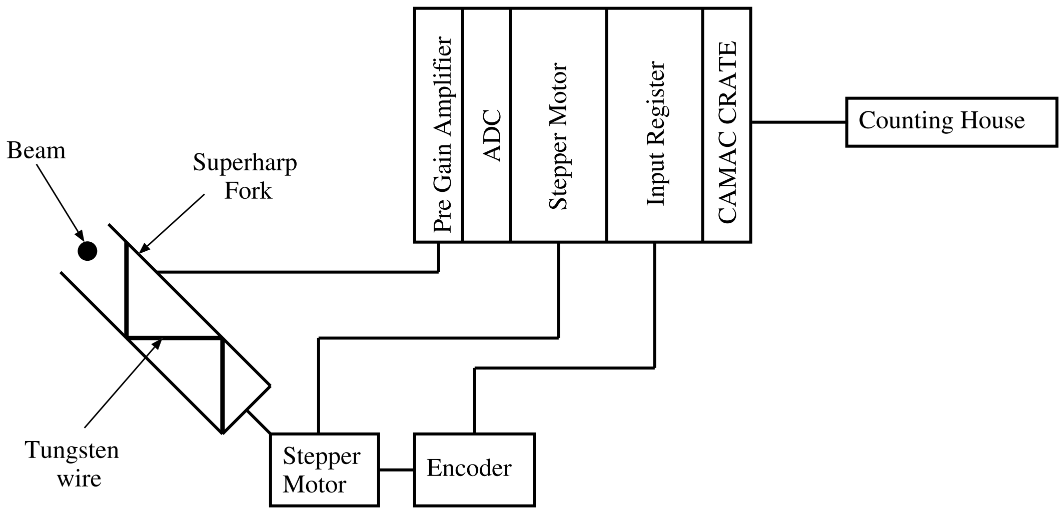

Figure 2.3: Schematic of a Hall C superharp system. When the fork is moved in the beam by the stepper motor, each wire crosses the electron beam and secondary emitted electrons produce a signal that is detected and amplified.

wooden frame and three tungsten wires. Two of them measure the beam profile in the horizontal X direction, the third one in the Y direction. The superharps are essentially the same as the harps. Fig. 2.3 shows the schematic of a superharp ensemble and its associated electronics. Since the superharp is the direct measure of the beam hitting the wires, their positions were surveyed more accurately to provide not only absolute position measurements but also the widths of the beam in the X and Y directions. The accuracy of the superharp readout is $\sim 10\mu$m. This is adequate for reconstructing the actual width of the beam which is about $100\mu m$ (FWHM) in both directions.

A BPM is a resonant cavity mounted in the beamline such that its axis will coincide with the nominal axis of the beam. In each BPM, four antennae are rotated $\pm 45^o$ from the horizontal and vertical. Each antenna picks a signal from the fundamental frequency of the beam which is proportional to the distance from the antenna when the beam is near the center of the cavity. From these four antennae, the relative (X, Y) position of the beam can be determined once the signals from the four antennae have been calibrated. The final accuracy of the beam position measurement was ± 1.02 mm, with a relative position uncertainty of 0.1–0.2 mm. The beam position from the BPMs was compared to the Arc C superharps in order to calibrate the absolute position for the BPMs.

Beam Energy Measurement

The energy of the incident electrons were measured in the Hall C arc. The beam momentum P can be determined examining the fields in the magnets in the last recirculating arc of the accelerator via

$$P = \frac{e}{\Theta} \int B \, dl \quad , \tag{2.1}$$

where $\int B \, dl$ is the magnetic field integral over the path of the electron beam, Θ is the bending angle through which the electron beam is deflected, and e is the electron charge. Alternatively, the settings in the Hall C arc are used in conjunction with measuring the beam position with the superharps and BPMs. The superharp scan provides the most accurate measurement. During production runs, however, the BPM information, which is less precise, was stored because the superharp scan is destructive for the beam. The accuracy of the absolute measurement is at the 10^{-3} level while the relative energy measurement accuracy is much better, $\sim 10^{-4}$.

Beam Current Monitors

The beam current in the hall was measured with three resonant cavity beam current monitors (BCM1, 2, and 3) and a parametric DC current transformer (Unser monitor), as shown in Fig. 2.2. The design of the BCMs is similar to that of the BPMs. In this case, one is interested in coupling to the TEM modes that are sensitive to the beam current and relatively insensitive to the beam position inside the cavity. The wave guides inside cavity contain wire loop antennas which couple to the resonant modes; the signal being proportional to the beam current for all resonant modes. The BCMs were calibrated using a parametric DC current transformer (Unser monitor). The Unser monitor measures the total charge passing through the device and its absolute gain can be measured to 10^{-7}. However, the Unser monitor can have large drifts in its offset and is therefore not useful for direct current measurements for the experiment. Calibration runs were taken about once a day in which the beam was alternately turned off and on over 2 minute intervals. During the beam off periods, the offsets of the Unser and cavity monitors could be determined and during the beam on periods, the gains of the cavity monitors could be calibrated against the fixed gain of the Unser. The Unser gain is calibrated by sending a precisely measured current through a wire that ran along the beam axis, thus simulating the effect of the electron beam. More detail for the beam current measurements is described in reference [24].

2.2.4 Beam Rastering

Since the Jefferson Lab accelerator generates a high current beam with small transverse size ($\leq$ 200 μm FWHM), in order to prevent damage to the target or the beam dump, two rastering systems that increase the effective size of the beam spot are used in Hall C.

The slow raster system was located just upstream of the target and was designed to protect the beam dump. The fast raster system was situated 25 m upstream of the target. It was designed to prevent the melting of the solid targets and to prevent localized boiling in the cryogenic targets. It consisted of two sets of steering electromagnets, one vertical and one horizontal. The current through the magnets was varied sinusoidally, at 17.0 kHz (vertical direction), and 24.2 kHz in the horizontal direction. The frequencies were chosen to be different so that the beam motion would not form a stable figure at the target. The typical raster size used in **E91-016** was $\pm$0.5 mm in both the horizontal and vertical direction (i.e. a 1 mm $\times$ 1 mm box). As the rastering signals were sinusoidal, the beam spent more time at the the edges of the box than it did at the center, thus the power was not uniformly distributed over the entire area of the raster pattern.

Despite this technical inconvenience, the reduction in power density due to the raster was enough to prevent significant density fluctuations (localized boiling) in the cryogenic target. The beam position at the target is monitored by BPMs, so that the rastering can be verified and the central beam position can be monitored and adjusted.

2.3 Target

The electron beam travels through the Hall C beam arc, into the Hall C experimental area through a beam pipe, and then into the scattering chamber where the cryogenic targets are located. The Hall C targets used for this experiment are shown in Fig. 2.4.

The target assembly used during **E91-016** consisted of two separate target ladders, one for solid targets and one for the cryogenic targets. Remotely controlled stepper motors allowed the vertical movement of each ladder (such that the desired target could be positioned in the beam path).

During **E91-016**, two solid targets (^{12}C and BeO) were in the solid target ladder. ^{12}C was used in the additional measurement, the $^{12}\mathrm{C}(\mathrm{e},\mathrm{e}'\mathrm{K}^+)$ reaction [25], and BeO and slanted ^{12}C for the sieve slit calibration runs for optics studies. The cryotarget is a set of loops through which liquid hydrogen or liquid deuterium flow [26]. The gases are cooled through heat exchange with liquid helium, the flow is regulated by fans, and the temperature is stabilized by heaters. The target

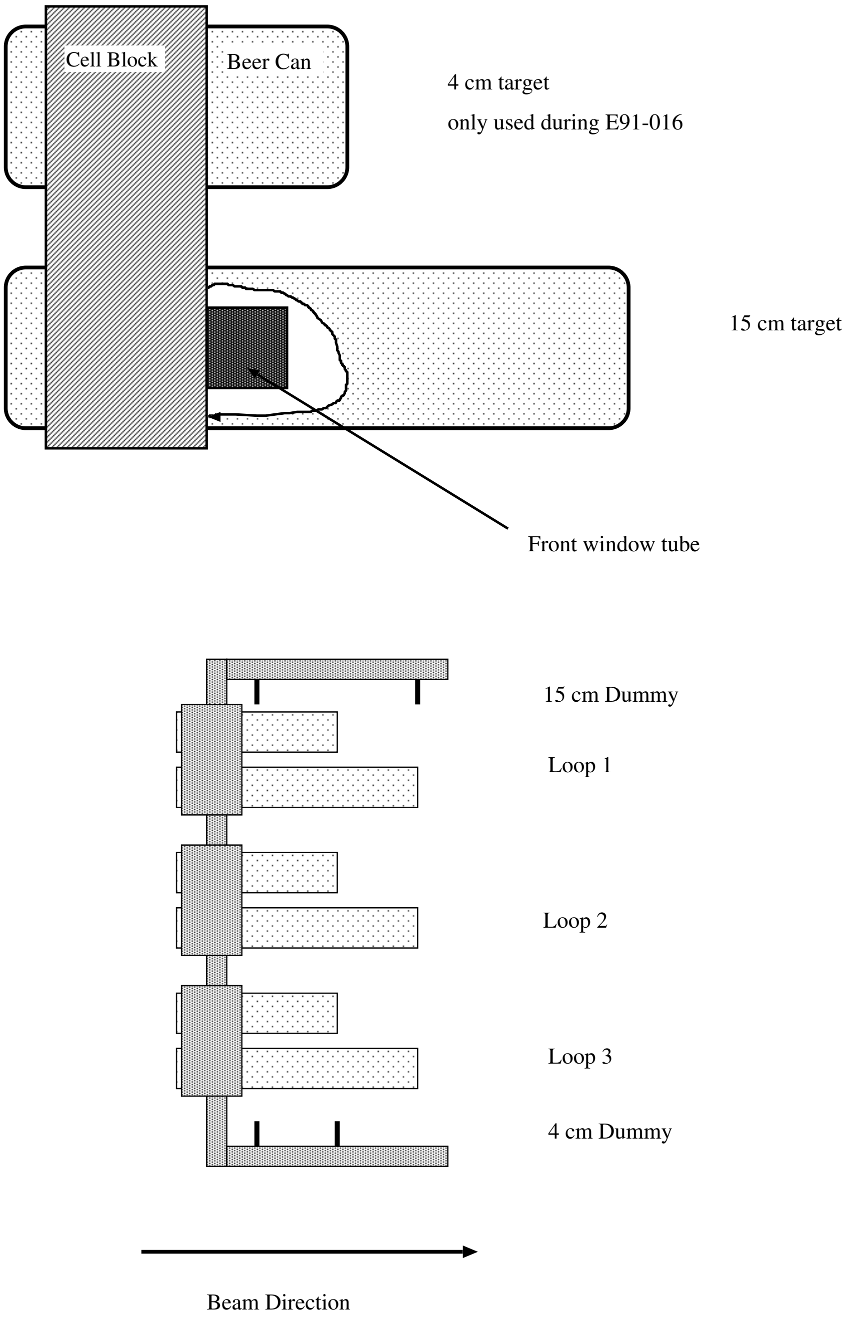

Figure 2.4: Schematic of the Hall C Cryotarget Cell Block Stack.

Target	Temperature (K)	Density (g/cm^3)	Purity (%)
Hydrogen	19.0 ± 0.05	0.07230 ± 0.0003	99.8 ± 0.10
Deuterium	22.0 ± 0.05	0.16708 ± 0.0007	99.2 ± 0.13

Table 2.2: The target properties of LH2 and LD2 target under normal running conditions.

configuration is in the shape of a beer can approximately 4 cm long in the direction of the incoming beam. Temperature is measured by Cernox resistors to a precision of 0.05 K. The nominal temperature and pressure for hydrogen is 19 K and 24 psi, and for deuterium is 22K and 20 psi. Since the density of the target material is a function of temperature, the temperature was kept constant by two pairs of heaters, a fast high power heater that matched the heat-load of the beam when it was on or off, and a low power heater that adjusted for slow variations in the cooling system. Target temperature was kept stable to $\lesssim 0.2^\circ$ for the majority of the experiment. Local density fluctuations due to the electron beam were minimized by rastering beam and fluid flow. To calculate the contribution of the walls of the beer cans to the data, empty targets with aluminum walls ten times thicker than those of the cryotargets were included in the target stack. The empty target walls were thicker than the cryotarget walls in order to increase the statistics in empty target runs. The thicknesses and properties of these aluminum targets are listed in table 2.3.

Switching from one target to another was done from the counting house, and the temperature and pressure of the targets were continuously monitored.

Target	Al 4 cm	Al 4 cm	Al 15 cm	Al 15 cm
Al Alloy	5052	3004	5052	3004
Density (g/cm^3)	2.57	2.64	2.57	2.64
Thickness (cm)	0.0960	0.0967	0.0960	0.0967
X_0 (g/cm^2)	23.63	23.64	23.63	23.64
Rad. Length	0.0109	0.0112	0.0109	0.0112

Table 2.3: The properties of Aluminum targets.

2.4 Spectrometers

The standard equipment configuration in Hall C at CEBAF consists of two highly flexible spectrometers. The High Momentum Spectrometer (HMS) has a large solid angle and momentum acceptance and is capable of analyzing high-momentum particles (up to 7.6 GeV/c). The Short Orbit Spectrometer (SOS) also has a large solid angle and momentum acceptance for central momenta up to 1.8 GeV/c. It is primarily used for detecting hadrons in coincidence with electrons in the HMS, but its detector package provides all of the particle identification necessary for use as a stand-alone electron spectrometer.

2.4.1 High Momentum Spectrometer (HMS)

The HMS is a 25^o vertical bend spectrometer, with superconducting magnets in a $Q\ \overline{Q}\ Q\ D$ design. The magnets are supported on a common carriage that rotates around a rigidly mounted central bearing. The detector support frame is supported by the same carriage as the magnets, thus fixing the detector frame

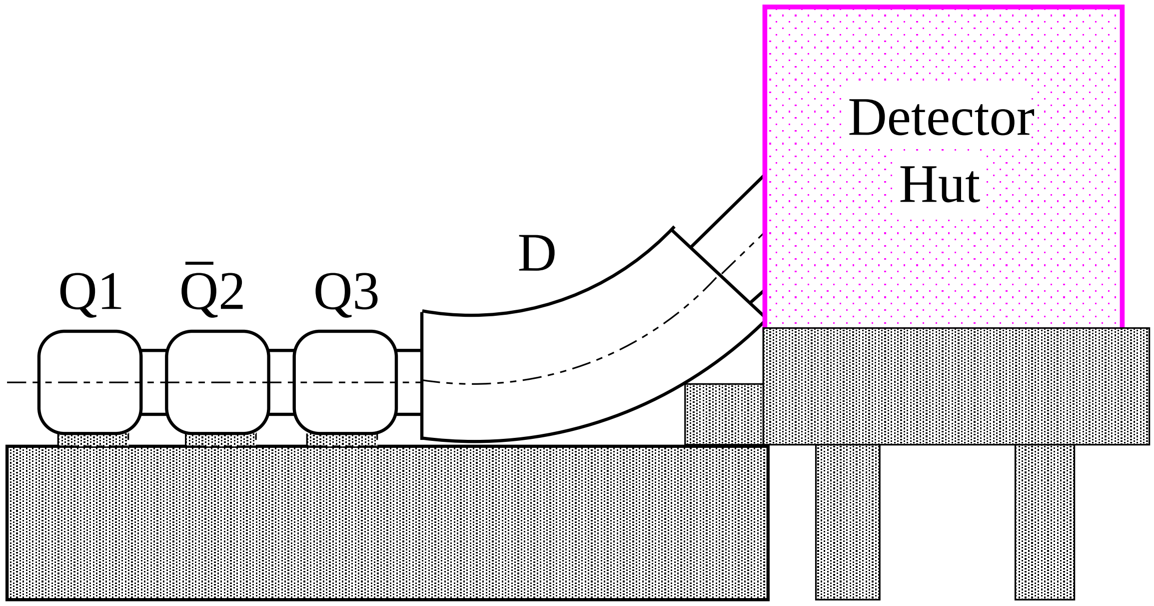

Figure 2.5: Side view of the HMS.

with respect to the optical axis, while the shielding hut is supported on a separate carriage. Fig. 2.5 shows a side view of the HMS spectrometer and detector hut.

The HMS was operated in its standard tune, point-to-point in both the dispersive and non-dispersive direction. This tune provides a large momentum, solid angle, and extended target acceptance. In this tune, Q1 and Q3 focus in the dispersive direction and Q2 focuses in the transverse direction. Most data were taken with an octagonal collimator designed to limit the solid angle. For a δ cut, $(p - p_0)/p_0$, of ± 10 % , the collimator limited the acceptance to 6.8 msr with greater than 90 % of the nominal acceptance for a point target. Table 2.4.1 summarizes the nominal performance parameters of the HMS.

Maximum central momentum	7.4 GeV/c
Momentum bite$[(p_{max} - p_{min})/p_0]$	18 %
Momentum resolution $[\delta p/p]$	< 0.1 %
Solid angle (no collimator)	> 6 msr
Angular acceptance - scattering angle	±32 mr
Angular acceptance - out of plane	±85 mr
Min. central scattering angle	12.5°
Scattering angle reconstruction	0.4 mr
Out of plane angle reconstruction	0.9 mr
Useful extended target acceptance	10 cm
Horizontal vertex reconstruction	∼ 1 mm
Momentum setting flexibility	0.5 ⇒ 7.4 GeV/c
Angle setting flexibility	12.5° ⇒∼ 90°

Table 2.4: Summary of the HMS performance.

2.4.2 Short Orbit Spectrometer (SOS)

The SOS was used to detect hadrons in coincidence with the HMS and was designed to be compact in order to allow detection of short lived particles (kaons and low momentum pions). It has a large solid angle and very large momentum bite (±20 %), but a somewhat limited extended target acceptance (∼ 2–3 cm).

The SOS was based on a QD$\bar{\mathrm{D}}$ design developed for the MRS (medium resolution spectrometer) at LAMPF. It consists of a quadrupole (Q) which focuses in the horizontal (non-dispersive) direction followed by two dipoles (BM01 and BM02) which bend the beam up 33^o and then down 15^o. All three magnets (as well as the detector hut) rest on a common carriage assembly, and the dipoles share a common yoke. The spectrometer rests 0.15° below the horizontal. Fig. 2.6 shows a schematic side view of the SOS spectrometer.

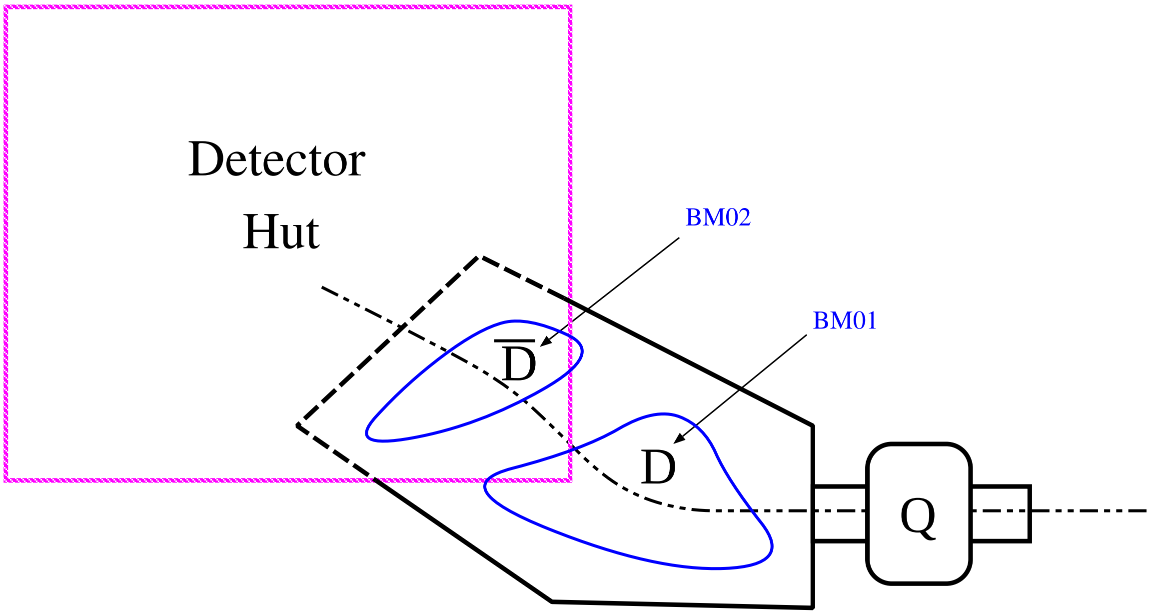

Figure 2.6: Side view of the SOS.

The quadrupole and dipoles are water cooled iron magnets powered by three separate InverPower power supplies which can be remotely controlled from the counting house. The power supplies can reverse the output polarity, allowing running for positive and negative particles.

For this experiment the SOS was operated in the point-to-point (PT-PT) tune, with point to point focusing in both the dispersive and non-dispersive directions. The ratio of the dipole fields ($\mathrm{D}/\bar{\mathrm{D}}$) was determined by integrating the field for the central trajectory using field maps of the dipoles. Because the Q was never mapped, the quadrupole field settings were determined using optics models generated with the COSY INFINITY program [27].These settings were examined by comparing the model to elastic scattering data taken with a sieve-slit (described

Maximum central momentum	1.8 GeV/c
Momentum bite$[(p_{max} - p_{min})/p_0]$	40 %
Momentum resolution $[\delta p/p]$	$<$ 0.1 %
Solid angle (no collimator)	$\sim$ 9 msr
Angular acceptance - scattering angle	$\pm$60 mr
Angular acceptance - out of plane	$\pm$40 mr
Min. central scattering angle	14.5°
Scattering angle reconstruction	0.5 mr
Out of plane angle reconstruction	1.0 mr
Useful extended target acceptance	4 cm
Horizontal vertex reconstruction	2-3 mm
Momentum setting flexibility	0.1 $\Rightarrow$ 1.8 GeV/c
Angle setting flexibility	14.5° $\Rightarrow\sim$ 169.4°

Table 2.5: Summary of the SOS specifications.

below), and the quadrupole field was lowered 7 % in order to better agree with the model. Table 2.5 summarizes the nominal specifications of the SOS.

A slit system installed in front of the SOS quadrupole allowed remote insertion of various collimators. There are three HEAVYMET (machinable Tungsten with 10 % CuNi; density=17 g/cc) collimators, namely the “large”, “small” and “sieve slit”, and one blank space in the slit box. The first collimator is a 1.25” thick sieve slit used for acceptance testing. It is an array of small holes (0.2” diameter) used to compare focal plane distributions to data with known angular distributions in order to study the optics of the spectrometer. The other two collimators are octagonal apertures designed to limit the solid angle acceptance of the SOS. Both are 2.5” thick and have flared holes that match the acceptance of the spectrometer. The large slit has a solid angle of $\sim$ 7.55 msr and was designed to keep losses within the spectrometer low for a point target ($\lesssim$ 2 % for a momentum bite of $\pm$15 %). The small slit was designed to give small losses in the spectrometer for an extended target (almost no loss for $\pm$20 % for a 2 cm target). All of our data were taken using the large octagonal collimator.

2.5 Detector Package

The standard HMS and SOS detector packages are nearly identical. Each spectrometer contains two drift chambers, two sets of x-y hodoscopes, a gas Čerenkov detector, and a lead-glass shower counter. In addition, the SOS has an aerogel Čerenkov detector between the back hodoscope pair. The drift chambers provided tracking information, the hodoscopes were used to form the primary trigger, and the calorimeter and Čerenkov signals were used for particle ID (pion rejection) in the trigger and in the offline analysis. Schematics of the HMS and SOS hut are shown in Fig. 2.7 and 2.8, respectively. The layout of the SOS detector package is more compact, but is otherwise nearly identical except for the addition of an aerogel Čerenkov detector between S2X and S2Y.

2.5.1 Drift Chambers

The HMS drift chambers consist of six planes, two measuring x (the dispersive direction), two measuring y (the non-dispersive direction), and two that were rotated $\pm 15^o$ from the x planes (the u and v planes). The planes were ordered

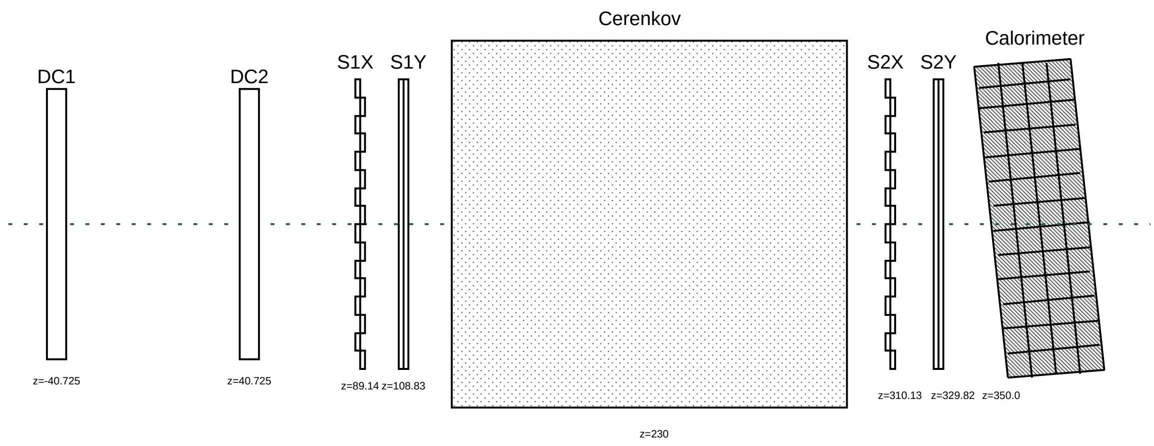

Figure 2.7: Schematic diagram of the HMS detector hut.

x, y, u, v, y', x' as seen by incoming particles. The chambers had an active area of approximately 107 cm (x) by 52 cm (y) with a wire spacing of 1 cm. The planes were spaced 1.8 cm apart and the two drift chambers were separated by ~ 80 cm.

Both the HMS and SOS wire chambers were filled with a argon/ethane mixture (50/50 by weight) and operated at a high voltage of -2.5 kV. The position resolution per plane is 300 μm (FWHM) for the HMS.

In the front of the SOS detector package, there are two chambers, DC1 and DC2, which were constructed at Brookhaven National Laboratory. Each chamber is composed of sixteen layers of 1/8 inch G10 plates, sandwiched between two 1/2 inch Al plates. The G10 plates support alternating planes of wires and cathode foils. The wire planes consist of alternating sense and field wires. The sense wires (30 μm diameter) are separated by 1 cm within the plane and detect the electrons and ions caused by the incoming particle ionizing the gas in the chamber. The field

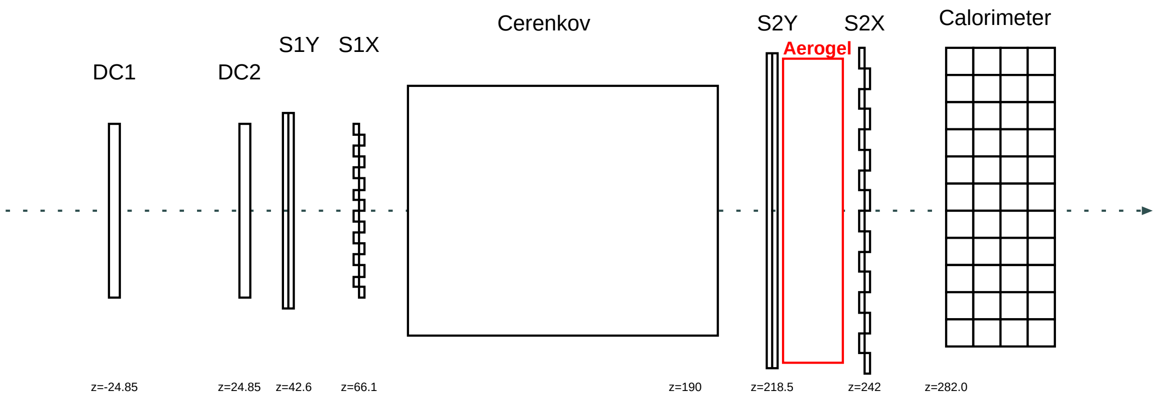

Figure 2.8: Schematic diagram of the SOS detector hut.

wires (60 μm diameter) alternate with the sense wires. The field wires and cathode foils are maintained at a large positive high voltage in order to isolate the sense wires. The wire planes come in pairs that measure position in the same direction and have their wires offset by 0.5 cm. The wire positions were measured during chamber construction and matched the expected values within the uncertainty of the measurement ($\pm$87 μm). The x and x' planes measure the position in the dispersive direction, the u/u' planes are rotated 60^o clockwise from the x plane, and the v/v' planes are rotated 60^o counterclockwise from x. There are 64 wires in the x and x' planes and 48 wires in the u, u', v, and v' planes.

The sense wires are read out in groups of 16, each connected to a LeCroy 2735DC or Nanometric N-277-L amplifier/discriminator card. The signals are read out from the discriminator cards on twisted pair ribbon cable and go to LeCroy multi-hit TDCs (LC1877) stored in the electronics shack located behind the detector hut. After the trigger is formed in the counting house and sent back to the hall, the TDCs read out all hits (up to 16 per wire) in the last 32 μ; the total time between a particle in the spectrometer and the trigger arriving at the TDC is less than 2 μs. The particle position is determined by using the TDC to determine the time between the particle passing through the chambers and the wire detecting the electrons created by the ionization of the chamber gas. This drift time is converted into a drift distance which is then added to the wire position in order to get the position of the event by comparing the distribution of times in the drift chamber with the expected position distribution in each cell. The hits in the other planes are used to determine on which side of the wire the event occurred. The final position resolution per plane is 250 μm FWHM.

The drift chamber position are known to 0.4 mm and the differences between the drift chamber positions and their desired positions is corrected for in the tracking software. The other detector positions are known to within a few mm from measurements in the huts and surveys of the detector stands. Using the precise measurements of the drift chamber positions, we used data from electron scattering to determine the positions of the other detectors with respect to the chambers. These numbers are put into the analysis code so that all positions measured by the detectors are translated into the focal plane coordinate system defined by the optics.

2.5.2 Hodoscopes

The HMS and SOS each have two pairs of x-y planes of hodoscopes, identical except for size of the elements. Each hodoscope plane is constructed of 9 to 16 elements. The hodoscope elements are long narrow strips of BC404 scintillator with light guides and phototubes on each end. The scintillators are wrapped with one layer of aluminized Mylar and two layers of Tedlar (PVF) to make them light tight with a minimum amount of additional material. The scintillators have approximately 0.5 cm of overlap between the elements in order to avoid missing particles. In the HMS, all of the scintillators are 2.12 cm thick and 8 cm wide. The x elements are 75.5 cm long, and the y elements are 120.5 cm long. The x planes have 16 elements each and the y planes have 10 elements each, giving each x-y pair an active area of 120.5 cm by 75.5 cm. The front and back planes are separated by approximately 230 cm. In the SOS, the front hodoscope pair is smaller than the back. The front x plane (S1X) has 9 elements, 36.5 cm $\times$ 7.5 cm $\times$ 1.0 cm and the front y plane (S1Y) has 9 elements that are 63.5 cm $\times$ 4.5 cm $\times$ 1.0 cm. The total active area of the front hodoscope is 63.5 cm $\times$ 365 cm. The rear hodoscope planes are larger versions of the front planes. The S2X plane is made of up 16 elements, each 36.5 cm $\times$ 7.5 cm $\times$ 1.0 cm and S2Y has 9 elements, 112.5 cm $\times$ 4.5 cm $\times$ 1.0 cm. Once again, the widths and lengths of the planes were matched so that the full area (112.5 cm $\times$ 36.5 cm) is active. The front and back planes in the SOS are separated by roughly 180 cm.

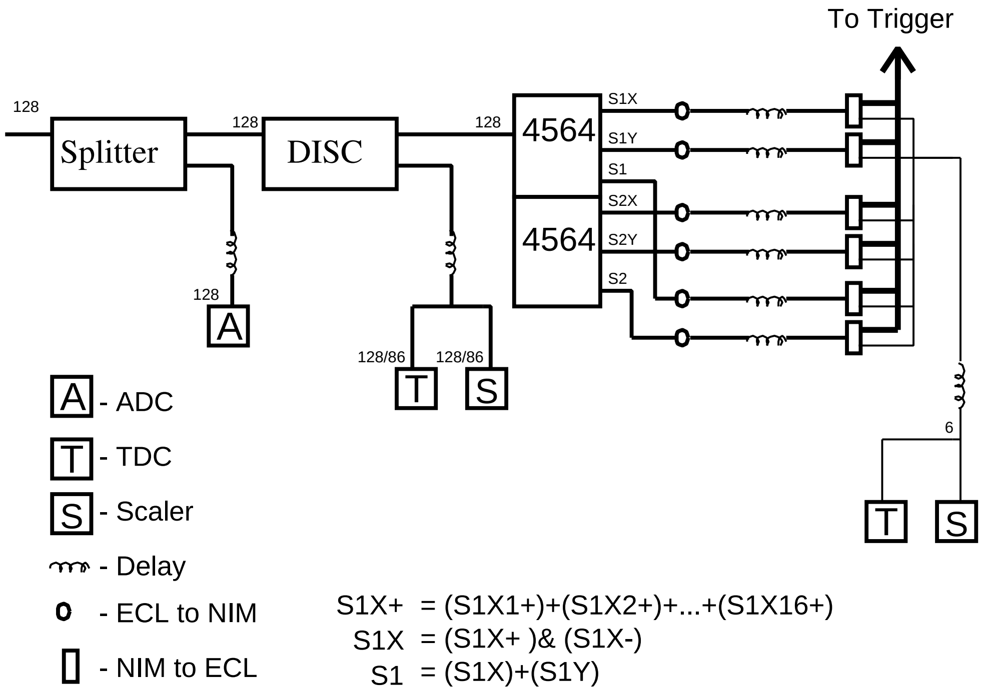

Figure 2.9: Hodoscope electronics. The numbers indicate the number of channels used in the HMS/SOS.

Each scintillator is read out from each end by Philips 2282, 8-stage PMTs. The output from the bases is sent to a patch panel in the detector hut through ~30 feet of RG58 cable, and then goes upstairs to the counting house through ~450 feet of RG8 cable. The signals are run through a splitter, giving two signals with 1/3 and 2/3 of the input signal. The smaller signal is put through ~ 400 ns of RG58 cable delay and then to the ADCs. The other output goes to discriminators. One set of outputs from the discriminators goes through logic delay modules to TDCs and VME scalers. The other set of outputs is sent to a LeCroy 4654 logic module. This module generates the OR of all tubes on one side of a given plane (e.g. S1X+). The outputs we use for the trigger logic are the AND of the sets of tubes on each side of a plane (S1X = S1X+ & S1X-), as well as the OR of the front (and back) pairs of planes (e.g. S1 = S1X + S1Y). Fig. 2.9 is a diagram of the electronics for the hodoscopes.

The hodoscopes were calibrated by gain matching the tubes with a ^{60}Co gamma ray source. Timing calibrations of the scintillators is done using data taken during running. Corrections for the "time walk" due to variations in pulse height and offsets between the individual elements are determined using an offline fitting procedure.

2.5.3 HMS and SOS Čerenkov

In order to improve particle identification, each spectrometer has a threshold gas Čerenkov detector between the front and back pairs of hodoscopes. In addition, an aerogel Čerenkov was inserted between X and Y planes of the rear hodoscope in SOS.

Gas Čerenkov Counters

The HMS tank is approximately 152 cm long and was filled with 0.9 atmospheres of nitrogen, giving a pion threshold of 4.9 GeV/c (and electron threshold of 17.9 MeV/c) and an average of 7 photoelectrons. There were two mirrors at the back of the tank which reflected the Čerenkov light into the two mirrors mounted on the side of the tank.

The SOS Čerenkov detector is a nearly rectangular aluminum box, 99 cm high, 73.7 cm wide, and 111 cm long. The detector was filled with 1 atmosphere of Freon 12 (CCl_2F_2). The index of refraction for Freon 12 is 1.00108, giving an electron threshold of 11 MeV and a pion threshold of 3 GeV(well above the SOS maximum momentum). The expected signal is 11 photoelectrons for a relativistic electron. The light is reflected onto four phototubes by four spherical mirrors. Each phototube has a Winston cone (a reflective cone around the phototube front face) designed to increase the effective solid angle of the tube.

For both spectrometers, the electron detection efficiency for a 2 photoelectron cut is $\sim$ 98 %. At high momentum, the pion contamination is dominated by the production of δ-electrons above the electron threshold. This limits the pion rejection to $\sim$ 500:1 for the HMS and $\sim$ 1000:1 for the SOS at the highest spectrometer momentum.

The gas Čerenkov signals were calibrated using the electron beam. A clean sample of detected electrons is chosen using the calorimeter to reject pions and tracking to insure that the event points to the center of one of the mirrors. For each mirror-PMT combination, the distribution of signals is fit to a Gaussian, and the average number of photoelectrons per event was determined by comparing the mean signal to the width. A Gaussian gave a good fit to the data, which should have a Poisson distribution, because of the large ($>$ 10) photoelectron yield. Once the mean number of photoelectrons is fit, the conversion from ADC channel to

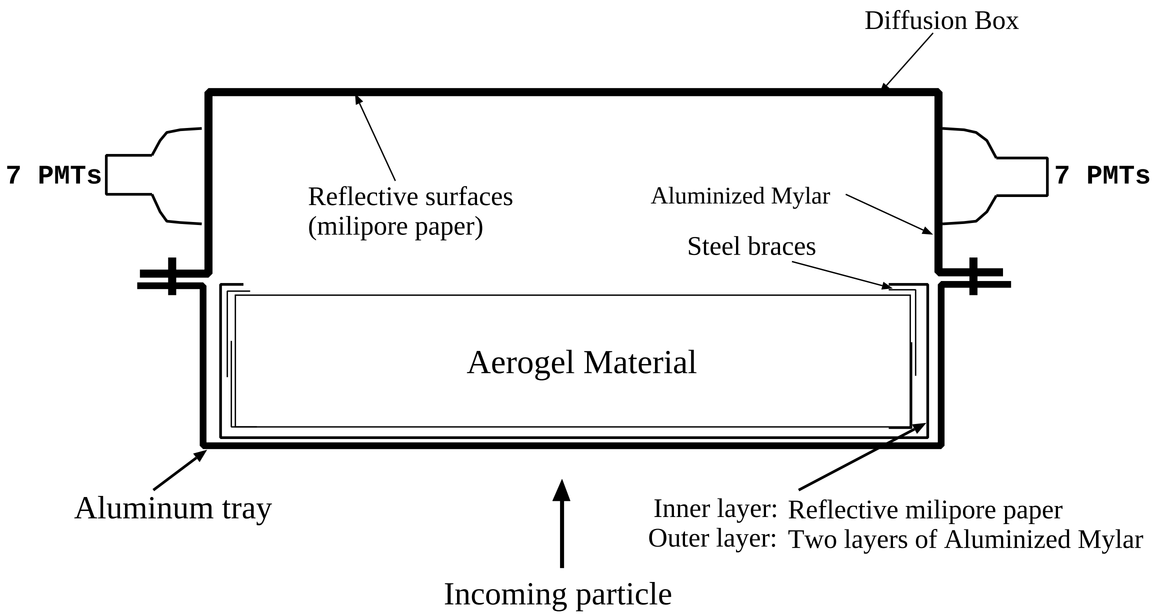

Figure 2.10: Cross section of aerogel detector. Total 14 PMT, 7 for each side, are connected.

photoelectrons is determined. Because the signal from the Čerenkov was used in the trigger, the high voltages were adjusted so that each tube gave the same signal to within about 10 %.

The HMS gas Čerenkov was in an "OR logic" trigger with the shower counter detector during **E91-016** data taking. The SOS gas Čerenkov was used for some of calibration runs during magnet setup for negative polarity.

SOS Aerogel Čerenkov

The aerogel Čerenkov detector is part of the standard SOS detector package. The aerogel detector is used to separate high momentum pions from heavier (slower) hadrons. The aerogel material (n(SiO_2)+2n(H_2O)) has an index of refraction of 1.034±0.001, giving a pion threshold of 510 MeV and a kaon threshold of 1.8 GeV/c. The material came in 25 cm × 25 cm × 3 cm tiles, and was cut and stacked in three 98 cm × 39 cm layers. The entire block, 98 cm × 39 cm × 9 cm, was wrapped in one layer of Millipore filter paper (∼ 97 % reflection) and two layers of aluminized Mylar on the sides but not the top. The block was then placed, uncovered side up, in an aluminum tray. Thin steel brackets held the aerogel material in place and thin wires strung across the open face. Opposite the open face was an inverted tray with a reflective lining of Millipore paper. The light is reflected several times in the diffusion box and is detected by fourteen phototubes in the side of the box. When the entire detector is in place, the incoming particles come through the aluminum tray, and produce light in the aerogel material. The light escapes through the open face and is collected by the phototubes mounted on the sides of the diffusion box (see Fig. 2.10). The useful active area is 95 cm × 35 cm and is mounted between the S2Y and S2X hodoscope planes. The diffusion box has ports for fourteen Burle 8854 photomultiplier tubes (seven on each side of the box), two gas feedthroughs, and 2 light fiber feedthroughs. The gas feedthroughs were used to maintain a clean, dry atmosphere by flowing dried nitrogen gas through the diffusion box. More detail description of the aerogel Čerenkov detector is discussed in a previous thesis [23]. The veto signal from the aerogel Čerenkov detector was used in the trigger for all production runs.

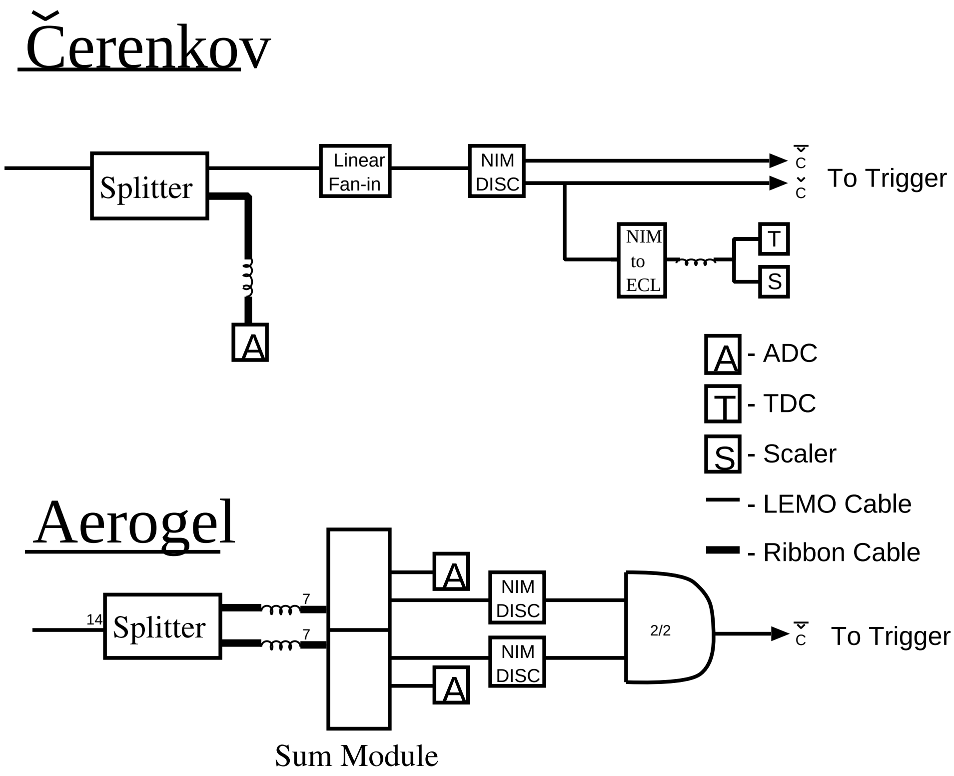

Figure 2.11: HMS gas and SOS aerogel Čerenkov Electronics.

The electronics for both the Gas and SOS aerogel Čerenkov detectors is shown schematically in Fig. 2.11. Signals from both detectors come up from the detector hut to the counting house through $\sim$ 30 feet of RG58 cable and $\sim$ 450 feet of RG8 cable. The signals are run through a 50–50 splitter and one set of outputs goes through 360 ns of RG58 cable delay to an LC1881M ADC. For the aerogel, the other output goes through a custom made amplifier module. The amplified signals, as well as a summed output go through delay cable and to the same ADC.

For the HMS gas Čerenkov signals, the second set of outputs was summed in an LC740 linear fan-in module and put through a discriminator to give signals for the trigger logic as well as outputs for TDCs and scalers.

2.5.4 Lead Glass Calorimeter

Both the HMS and SOS both had lead glass calorimeters used to identify electrons. The calorimeters were of identical design and construction except for their total size. The shower counters are constructed from 10 cm $\times$ 10 cm $\times$ 70 cm blocks of TF1 lead glass. The blocks are stacked transversely to the incoming particles, four layers deep. The stack is 13 blocks high in the HMS (11 in the SOS), for a total of 52 (44) modules and an active area of 130 cm $\times$ 70 cm (110 $\times$ 70 cm in the SOS). The calorimeters are rotated $\sim 5^\circ$ from the optical axis in order to avoid loss through the cracks between the modules (see Fig. 2.7).

2.6 Trigger

Because of high counting rates, selection of appropriate particles had to be provided. Since kaon detection required coincidence counting, each spectrometer also had some particle selection.

2.6.1 Spectrometer Triggers

The HMS and SOS had separate trigger systems which provided triggers for 'good' events in each spectrometer. The first part of the trigger came from the hodoscope signals which were generated when a charged particle passed through the spectrometer. The gas Čerenkov counter and calorimeter signals were used to label the trigger as having come from an electron or a pion. If an event had either a Čerenkov signal or a large shower counter signal, it was counted as an electron. This was highly efficient for electrons, but limited the hardware pion rejection to 10:1. In the HMS, triggers with no Čerenkov signal were labeled as pions. The electron events were all recorded, and the pion triggers were prescaled so that a sample of the pions would also be taken. After the raw spectrometer trigger was formed (the 'pretrigger'), additional logic provided the final trigger for the trigger supervisor and ADC gates and TDC start/stops for the event.

In the SOS which detected the slower moving kaons, the primary particle separation required was between pions and kaons. For this purpose the aerogel counter was inserted into the trigger in a manner analogous to that used in the HMS for pion-electron separation. Particles with no aerogel signal were labeled kaons subject to further analysis. The full trigger logic for the single spectrometer trigger is shown in Fig. 2.12 and is described below.

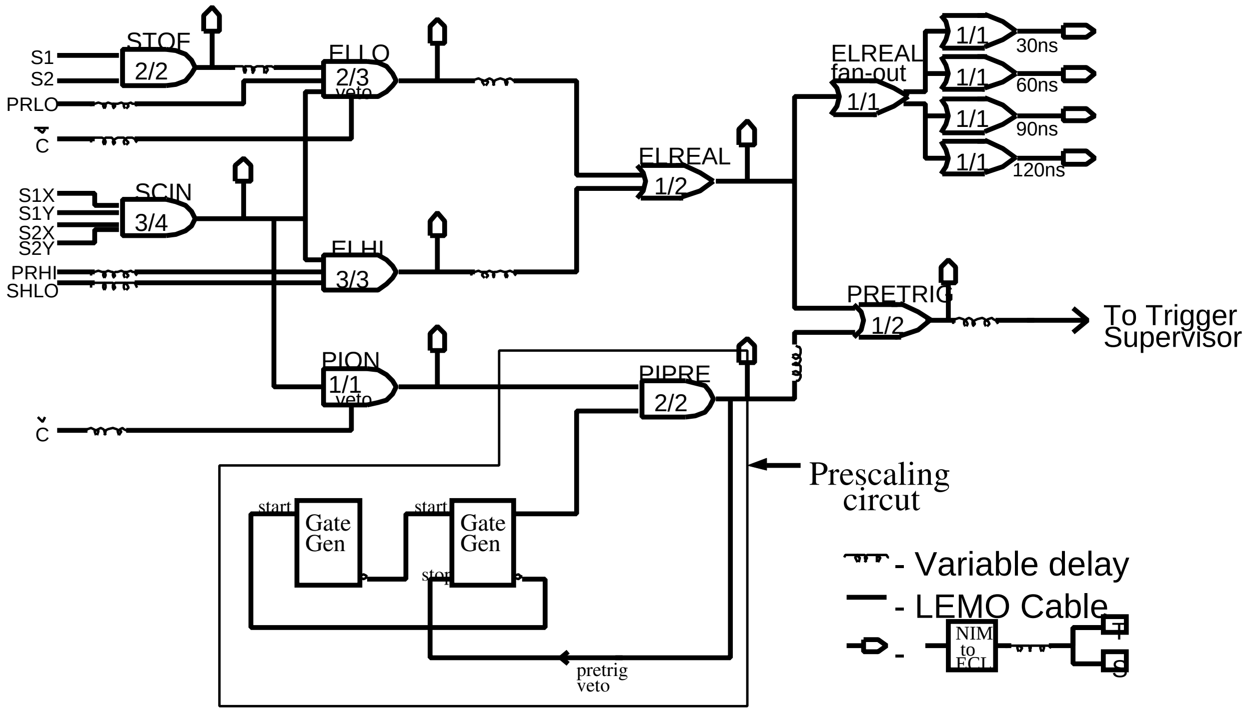

Figure 2.12: HMS/SOS single arm trigger electronics.

2.6.2 Trigger Supervisor

The interface between the trigger hardware and the computer data acquisition system is the trigger supervisor (TS). The TS makes all of the 'decisions' about how to process the triggers it receives, choosing which triggers to respond to as well as determining what state the run is in. In order to reduce the event size, we use the sparsification feature of our ADCs and TDCs. The TDCs normally operate in sparsified mode, not giving an event for a channel if there was no stop signal after the common start. The data acquisition mode is controlled using the TS status outputs. There are two outputs from the TS that determine how events will be processed. The TS GO signal is active at all times when a run is in progress. The TS EN1 signal indicates that a run is in progress and normal data taking in enabled. Finally, the TS BUSY signal is active whenever the TS is busy processing an event. During a normal run, the following sequence of events occurs: first, the TS GO signal comes on, and we allow pedestal triggers (from a pulser). After 1000 events the ADCs change over to sparsified mode and the TS enables the physics triggers and blocks the pedestal triggers. In addition, the TS provides a busy signal that blocks triggers whenever the TS is busy processing an event.

The Trigger Supervisor provides all of the control signals, but in order to have an 'external' record of the logic that went into processing the event, the blocking of trigger due to the status of the run or the TS is done in external logic and the intermediate steps are sent to scalers and TDCs to be recorded. The trigger signals (HMS, SOS, and PED triggers) and the TS control signals are fed into an 8LM programmable logic module. The 8LM has eight outputs. Four are used for the HMS, SOS, COIN, and PED pretriggers. Table 2.6 shows the programming of the 8LM.

In addition to determining what types of triggers are to be processed, the trigger supervisor determines what hardware needs to be read out based on the trigger type. When a trigger arrives at the TS, it waits 10 ns and then latches all of the enabled trigger types into a data word. It then uses a lookup table to determine what event type the trigger corresponds to and what gates need to be

output signal		definition
HMS PRETRG	=	$(HMS)\&(EN1)$
SOS PRETRG	=	$(SOS)\&(EN1)$
COIN PRETRG	=	$(COIN)\&(EN1)$
PED PRETRG	=	$(PED)\&(GO)\&(\overline{EN1})$
HMS TRIG	=	$(HMS)\&(EN1)\&(\overline{BUSY})$
SOS TRIG	=	$(SOS)\&(EN1)\&(\overline{BUSY})$
COIN TRIG	=	$(COIN)\&(EN1)\&(\overline{BUSY})$
PED TRIG	=	$(PED)\&(GO)\&(\overline{EN1})\&(\overline{BUSY})$

Table 2.6: 8LM Trigger Logic.

generated for data readout. There are four defined event types: HMS, SOS, COIN, and PED events. These do not exactly correspond to the incoming trigger types, because if multiple triggers come in, the TS has to decide what kind of trigger it is. For example, if both the HMS and SOS triggers come (or the COIN with anything else), the TS treats the event as a coincidence.

After the TS sends out the gates, each spectrometer retimes the gates it receives with respect to the single arm trigger for that spectrometer. This is necessary for coincidences because the ADC gates must come at a fixed time with respect to the time the particle passed through the detector.

2.6.3 Other Signals

In addition to providing signals for the trigger, all of the intermediate signals are sent to scalers and TDCs. The TDCs are used mainly as latches, and tell which signals were present when the trigger was taken. This allows us to determine what kind of event formed the trigger. The scalers allow us to quickly look for certain

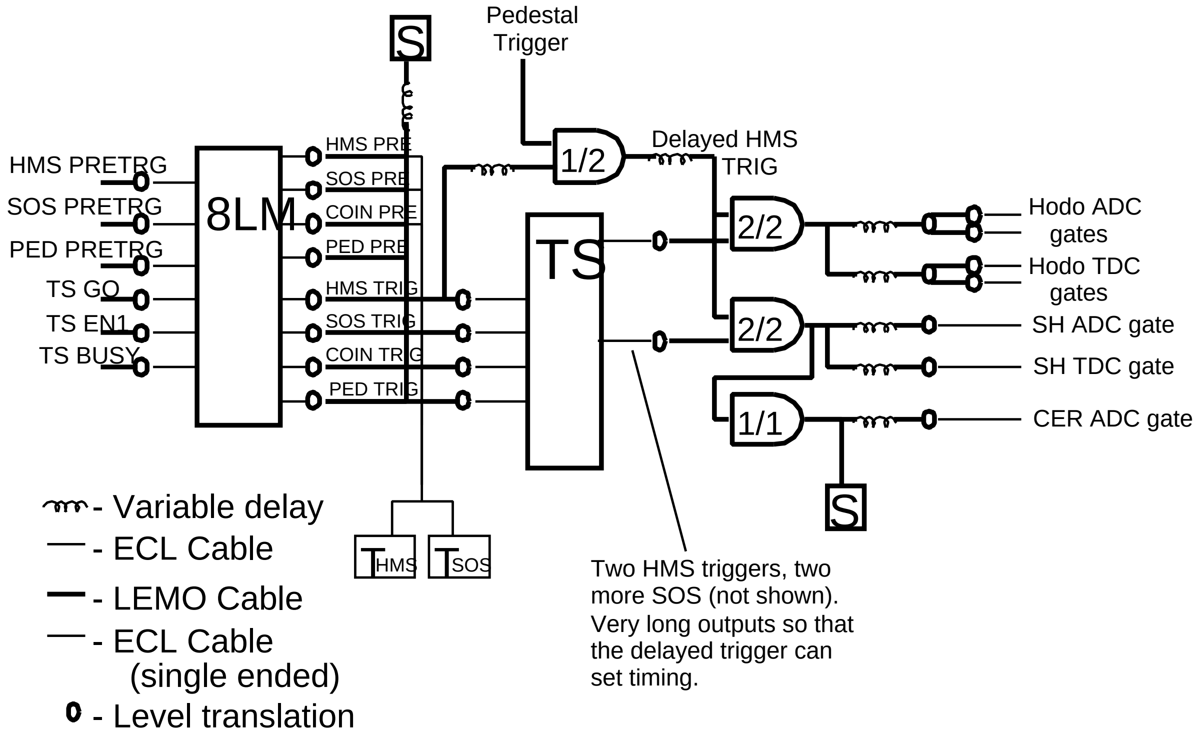

Figure 2.13: Trigger Supervisor Electronics.

types of electronics problems in the intermediate steps of trigger formation. We also use the scalers to measure computer and electronics dead time.

2.6.4 Data Rates

The maximum data taking rate is limited by the Fastbus conversion and data readout time. In basic data acquisition mode, the total time to process an event is just under 1 ms. The time is broken up as follows: $\sim$ 100 μs for Fastbus data conversion, 400 μs for Fastbus readout, and 400 μs for transporting the Fastbus information through the VME readout. This limits data acquisition to $\sim$ 1 kHz, but gives large computer dead times even at lower rates. Several improvements have been made to improve the data rate and decrease dead time. Optimization of the Fastbus reading and utilization of the multi-block read feature of the ADCs reduced the Fastbus processing time to 300 μs, giving a total time to process the event of $\sim$ 400 μs and a trigger rate limit of $\sim$ 2 kHz.

2.7 Data Acquisition

The data files for the runs contained both event information and slow controls readout. These two types of information were read out separately. CODA (the CEBAF Online Data Acquisition system) was the data acquisition system developed by the data acquisition group at CEBAF and used for this experiment. Information on CODA and RunControl (a graphical user interface) can be found in [28, 29]. The system in place for Hall C experiments is described in reference [30].

2.7.1 CODA - Physics Events

CODA provides the user interface and manages the DAQ sub-systems. When a run has been started, CODA determines how to handle triggers from the trigger supervisor (TS) module. The events are processed by the event builder (EB) which reads data fragments from the Fastbus and VME crates which house the ADCs and TDCs. The data from these crates, or ROCs (Readout Controllers) is passed to the event builder which puts together the raw data along with the header information into the event file. In addition, the data can be sent through an analyzer subsystem to allow for full or partial online analysis of the data or preprocessing of the events before they are recorded to disk or tape. The default analyzer is a dummy routine and is combined with the event builder into one program to improve performance.

For our experiment, the spectrometers provided independent triggers, and the physics events contained only data for the associated spectrometer. The TDCs were sparsified, so that only channels with stops were read out. The ADCs had programmable thresholds for each channel, allowing sparsified readout of the ADCs as well. The thresholds were typically set to be 15 channels above the pedestal. The 1000 random triggers were generated at the beginning of the run with sparsification disabled in order to measure the centroids and widths of the pedestals. In addition to the spectrometer information, some beam related quantities were read out on an event-by-event basis. Beam position monitors, beam loss monitors, and beam raster readback values were recorded for each event.

2.7.2 EPICS - Slow Controls

In addition, other event types can be defined in CODA, allowing readout of hardware scalers or execution of user scripts. Readout of the hardware HMS and SOS scalers was triggered every two seconds by an asynchronous process. Slow controls were read out by a script triggered by CODA every 2 minutes.

The values for the slow controls variables were read out from the CEBAF EPICS database. Values such as spectrometer magnet settings, accelerator settings, and target status variables were accessed this way. In addition, separate processes allowed independent target data logging and magnet status logging.

2.8 Kinematic setup

The kinematics settings for the angular dependence of kaon electroproduction are shown in Table 2.7. All indicated values are the mean of given kinematic variable for the Λ production.

Set	E_e (GeV)	$p_{e'}$ (GeV/c)	p_{K+}	$\theta_{e'}$ Degree	θ_{K+}	Q^2 (GeV^2)	W (GeV)	$-t$ (GeV^2)	$\theta_{\gamma K}^{CM}$ Degree	ϵ
1	3.245	1.723	1.077	17.19	17.67	.499	1.799	.247	10.7	.79
2	3.245	1.723	1.077	17.19	22.00	.499	1.799	.257	16.0	.79
3	3.245	1.723	1.077	17.19	26.45	.499	1.799	.289	26.9	.79
4	3.245	1.723	1.077	17.19	30.96	.499	1.799	.344	39.0	.79
5	3.245	1.723	.929	17.19	17.67	.499	1.799	.340	12.3	.81
6	3.245	1.723	.929	17.19	22.00	.499	1.799	.349	15.1	.81
7	3.245	1.723	.929	17.19	26.45	.499	1.799	.376	26.1	.81
8	3.245	1.723	.929	17.19	30.96	.499	1.799	.423	38.8	.81
9	3.245	1.594	1.240	15.46	15.48	.374	1.898	.172	9.7	.76
10	3.245	1.594	1.240	15.46	19.92	.374	1.898	.194	17.4	.76
11	3.245	1.594	1.240	15.46	25.00	.374	1.898	.251	29.9	.76

Table 2.7: Nominal kinematics for **E91-016** angular distributions for kaon electroproduction on hydrogen and deuterium targets, where $\theta_{\gamma K}^{CM}$ is for Λ production. All variables are defined in Eq. 1.11 and Fig. 1.1.

CHAPTER 3

DATA ANALYSIS

3.1 Overview

The analysis of the raw data files was done using the Hall C Engine. The engine reads the raw events, decodes the detector hits, and generates tracks and particle identification information for each event. In addition, it keeps track of the hardware scalers and generates software scalers for the run. The detector calibrations were done using separate code and the results were taken as input to the engine. The data is output in three forms: (i) Report files contain the hardware and software scalers, as well as calculated detector efficiencies. (ii) PAW HBOOK files contain the standard set of histograms which can be used to check detector performance and monitor the hardware during the run. (iii) PAW ntuple files contain the event by event information, and are the main output used in the final physics analysis. Histograms and ntuples are generated using the CERN HBOOK libraries. Input parameters, software scalers, histograms and tests are handled using the CEBAF Test Package (CTP).

3.2 Hall C Engine

The Cebaf Test Package (CTP) software was written at CEBAF to provide a flexible way to store and modify histogram, test, and scaler definitions and other analysis parameters. CTP is modeled loosely on the LAMPF Q system [31]. In order for CTP to 'share' variables with the Fortran code, the variables must be 'registered' using calls to CTP C subroutines. When the code is compiled, all of the variables defined in the common blocks are automatically registered. They are then accessible from both the Fortran source code and from CTP so that the variables can then be examined or changed without recompiling code. In addition, variables that are not part of the engine's Fortran code can be defined and used to create tests and to define histograms.

The analysis engine primarily uses CTP to input parameters and run time flags that control the analysis, and to define the histograms, tests, and scalar reports for output. The parameters and histogram and test definitions are stored in ASCII files and read in at the beginning of the analysis code. At the end of each event, the CTP tests are evaluated. The histograms are filled and software scalers incremented using the results of the tests. In addition to setting the input parameters and defining the output files, CTP allows the user to examine and modify variables when running the event display code. This allows one to select events by setting a CTP test, and then study the event in detail. The ability to examine and modify the Fortran variables through CTP makes the event display a useful debugging tool. The flow of the analysis code is has been described previously [32].

3.2.1 Initialization

The engine starts by reading in the main configuration file, defined by an environment variable. This file gives the names of the data file, and the input and output filenames and test/histogram definition files. Some of these files are used to set the parameters that define the locations, calibrations, and decoding of the detector elements. Others are used to define the CTP variables used in the histograms and tests. Kinematics and other quantities that vary from run to run are read in separately from a parameter file. After all of the run parameters are defined, the PAW HBOOK and ntuple initializations are performed, and the raw data file is open. The engine then begins looping through the events in order to analyze the beginning of run information events. These include readback values from the ADCs and TDCs, runtime options, and kinematics input by hand at the beginning of each run. Once these initialization events have been analyzed, the main event loop begins.

3.2.2 Main Event Loop

In the main event loop, each event is read in and then processed according to the event type. If the event is a scaler read, it is analyzed and the total counts and change in counts are recorded. In addition, the time and accumulated charge since the last event are calculated, and the total charge is incremented. If the event is an EPICS read event, the EPICS variables are stored. Finally, if it is a physics event, it is analyzed if its enable flag has been set. There are four types of physics triggers. At the beginning of each run, 1000 pedestal triggers are generated. The physics events are HMS, SOS, and COIN triggers and are the events generated by the real spectrometer triggers. The raw detector hits are read in for these events and passed to the main reconstruction routine for the HMS and/or SOS. The event is reconstructed, particle ID information stored for each spectrometer, and then physics quantities are calculated for singles triggers in each spectrometer and for coincidence events, if both spectrometers fired.

3.2.3 Event Reconstruction

The reconstruction code for each spectrometer is nearly identical, except for the aerogel analysis code in the SOS. The data structures and analysis code are the same for the HMS and SOS detectors and, for the most part, only the names and parameters are different for the two spectrometers.

First, the hodoscope hits are translated from raw ADC and TDC values to times and pulse heights. Timing corrections due to pulse height variations and cable length offsets are applied, and events outside of a user defined timing window are discarded to eliminate random hits. The hits are used to determine the velocity of the particle and the time that the particle passed through the drift chambers. This time is used as the start time for the drift chambers when calculating the distance of the particle from the wires that were hit. After the hodoscopes have been decoded and the start time determined, the drift chamber, calorimeter, and Čerenkov hits are decoded and track independent quantities, total calorimeter energy and Čerenkov signal, are calculated.

Next, the tracking routine is called. The drift chamber hits are used to identify clusters of hits (space points) in each chamber. To reduce the time of the tracking, we use a small angle approximation for all of the SOS planes and the y,y' planes in the HMS. If there are hits in both the x and x' planes (or any two parallel planes), one can choose the left-right combination that makes the particle go between the wires, since the wires are spaced by 1 cm, but the parallel planes are offset by 0.5 cm. For planes that are close together and incoming particles that are nearly perpendicular to the drift chambers, this is a very good approximation. Finally, for each pair of stubs in the front and back chambers, a full track is fit if the two stubs were consistent. Each of these tracks is recorded along with the χ^2 of the fit.

Information used for particle identification is then calculated for each track that was found. The time of flight through the hodoscopes (i.e. the particle velocity) was calculated for all hits that were on the track. At least one hit in the front planes and one in the back was required in order to have a good time of flight measurement. The energy in the calorimeter for each track is determined by finding clusters of hits in the lead glass blocks, and then summing the hits within each cluster. The calorimeter signal associated with each track is the energy in the clusters that track points to, if any. Finally, each track is reconstructed to the target to give the angle in the dispersive direction, position and angle in the non-dispersive direction, and the momentum.

If there are multiple tracks, the best track is selected by applying cuts on the particle velocity, and the calorimeter signal. If all tracks pass these cuts, then the track with the best χ^2 is selected as the final track. For the final track, the desired physics quantities are calculated, and the tests and histograms for the singles events are filled. If there was a final track in both spectrometers, the coincidence physics quantities are calculated, and coincidence tests and histograms are filled.

3.2.4 Output

When the end of the run is encountered, the engine dumps the output files. Scaler report files contain the final values for the hardware and software scalers, as well as measured detector efficiencies, beam current, and dead time correction factors. The histogram files primarily contain detector summary histograms, so that the detector performance can be measured online and the calibrations can be checked offline. The ntuple files contain the event by event information. Tracking information, reconstructed quantities, and particle ID information are contained in the ntuple, so that cuts on the reconstructed or PID quantities can be applied.

3.3 Tracking

The tracking information (x, y, x′, y′ at the focal plane) has been extracted by the χ^2 fitting to the space points of all 12 planes inside two drift chambers and was briefly described in Section 2.5.1. If the five out of six planes provide the space points in each chamber and the fitted track from one chamber connects to the track from the other chamber, the events are labeled as true track. These true track events remain in the final ntuple files.

The events with multi-tracking, i.e. more than one track, or no track are eliminated by the replay engine tracking algorithm, see [33] for details. The tracking efficiencies in both spectrometers are extracted by looking at the fiducial regions and are shown in Table 3.1. The data yields are corrected for tracking efficiencies.

3.4 Reconstruction of Trajectory

After the tracking information (x, x′, y, y′) at the focal planes is calculated from the space points inside two drift chambers, these quantities are transformed back to the target position. Since the experiment studies the reaction at the target, the four quantities, momentum (δ), slopes (x′, and y′), and y at the target

Set	Target	Tracking		Computer	Electronic	Correction	
		HMS	SOS	D.T (%)	D.T (%)	Factor	Err.(%)
1	H	$.9574 \pm .0035$	$.9097 \pm .0014$	$6.380 \pm .139$	$.942 \pm .019$	1.238	.426
	D	$.9620 \pm .0002$	$.8836 \pm .0011$	$12.642 \pm .400$	$1.424 \pm .019$	1.379	.476
2	H	$.9591 \pm .0029$	$.9138 \pm .0010$	$6.912 \pm .230$	$.908 \pm .011$	1.237	.406
	D	$.9586 \pm .0001$	$.8848 \pm .0005$	$17.033 \pm .512$	$1.517 \pm .010$	1.460	.624
3	H	$.9519 \pm .0025$	$.9290 \pm .0010$	$5.637 \pm .147$	$.689 \pm .003$	1.207	.322
	D	$.9540 \pm .0008$	$.9122 \pm .0012$	$12.378 \pm .268$	$1.149 \pm .008$	1.332	.342
4	H	$.9574 \pm .0006$	$.9378 \pm .0004$	$5.350 \pm .026$	$.557 \pm .002$	1.183	.084
	D	$.9518 \pm .0002$	$.9267 \pm .0002$	$11.796 \pm .093$	$.936 \pm .003$	1.298	.110
5	H	$.9620 \pm .0007$	$.8997 \pm .0065$	$6.679 \pm .511$	$1.092 \pm .045$	1.258	.905
	D	$.9593 \pm .0002$	$.9103 \pm .0004$	$8.458 \pm .061$	$1.359 \pm .006$	1.268	.083
6	H	$.9603 \pm .0017$	$.9091 \pm .0018$	$7.671 \pm .319$	$1.073 \pm .034$	1.254	.439
	D	$.9559 \pm .0002$	$.9073 \pm .0004$	$12.596 \pm .271$	$1.519 \pm .011$	1.340	.316
7	H	$.9585 \pm .0012$	$.9192 \pm .0040$	$6.878 \pm .466$	$.894 \pm .038$	1.233	.672
	D	$.9536 \pm .0003$	$.9101 \pm .0002$	$13.759 \pm .085$	$1.428 \pm .003$	1.356	.105
8	H	$.9575 \pm .0004$	$.9292 \pm .0004$	$6.767 \pm .044$	$.812 \pm .004$	1.216	.079
	D	$.9525 \pm .0002$	$.9131 \pm .0002$	$14.981 \pm .156$	$1.370 \pm .005$	1.371	.187
9	H	$.9574 \pm .0003$	$.9230 \pm .0018$	$6.858 \pm .553$	$.812 \pm .038$	1.234	.629
	D	$.9569 \pm .0002$	$.9183 \pm .0004$	$15.840 \pm .904$	$1.064 \pm .010$	1.390	.930
10	H	$.9602 \pm .0003$	$.9254 \pm .0004$	$8.420 \pm .278$	$.882 \pm .004$	1.242	.309
	D	$.9595 \pm .0001$	$.9249 \pm .0003$	$11.072 \pm .172$	$1.007 \pm .015$	1.281	.198
11	H	$.9597 \pm .0004$	$.9246 \pm .0007$	$8.097 \pm .552$	$.768 \pm .024$	1.242	.611
	D	$.9574 \pm .0001$	$.9245 \pm .0003$	$10.626 \pm .316$	$.894 \pm .004$	1.279	.357

Table 3.1: Tracking efficiencies and dead time inefficiencies.

are determined by the matrix transformation which is a polynomial function of the four quantities at the focal plane. The set of traceback matrix elements were obtained from the inverse of the forward matrix set which was generated by COSY INFINITY on the basis of measured field maps and spectrometer design specifications. These were also used in the Monte Carlo simulations. Many elements of the matrix are zero as a result of the midplane symmetry, especially for the SOS side. All elements of the HMS matrix, up to the 4th order, are involved because of the vertical offset and rotation of the center quad, Q2; also seen in the RAYTRACE simulation. All coefficients of the SOS matrix elements were optimized by fitting optics calibration data.

3.4.1 Optimization of SOS Reconstruction

To optimize the elements of the SOS matrix set, the previous optics calibration data, namely sieve slit and elastic delta scan runs on the ^{12}C (taken in November 95 and April 96) were used. The fitting code [34] used for this optimization was developed by K. A. Assamagan, D. Dutta, and P. Welch. The holes in the sieve slit, located in the first collimator position, correspond to the angle or slope information at the point target. In the fitting code, the events at the each hole are carefully selected from the pattern at the focal plane and then forced to fit the given hole. The sets of sieve slit runs from the various z-positions at the target provided the optimization of y position and two slopes (x', and y') to

Quantity	Modified quantities
hsdelta	hsdelta+.1
hsxptar	no offset
hsyptar	hsyptar - .001
ssdelta	(ssdelta+.35)-ssxptar×8
ssxptar	ssxptar - .0005
ssyptar	no offset

Table 3.2: Offset and modification for matrix reconstructed quantities.

account for extended targets. For delta reconstruction fitting, only elastic events from $^{12}\mathrm{C}(\mathrm{e},\mathrm{e}')$ runs are selected. The angle information extracted from previous sieve slit fitting was used to calculate the momentum and convert to delta ($\frac{p-p_\circ}{p_\circ}$). After deltas are determined, the fitting routine optimized all elements for delta as a function of the four focal plane quantities. The detailed description of the fitting procedure is in the reference [34]. The SOS matrix reconstruction elements [35] distributed by K. A. Assamagan in October 97 were used. The first order offset components for each reconstructions element which was extracted during the analysis of calibration data, such as $H(e,e'p)$ elastic runs, are shown in Table 3.2.

3.4.2 Optimization of HMS Reconstruction

To study the HMS optics, the sieve slit pattern at the focal plane simulated by RAYTRACE was compared with sieve slit data taken during **E91-016**. The events generated at the point target, because of the width of sieve slit, are selected only if the events passed through the back holes. The generated events included the .49 mm offset of sieve slit which was measured in a later survey report [36]. The starting RAYTRACE code for HMS provided by Y. Chen was generated according to measured field maps and TOSCA simulations; the code included octupole effects in the quadrupoles. The octupole effect in the quadrupoles was seen during the field mapping [37].

The events generated at the target are traced to the focal plane by the forward RAYTRACE code. The simulated patterns at the focal plane were compared with the same patterns from data. The code was optimized until the patterns of the data and simulation were consistent with each other. During this optimization, the two major offsets for Q2 and others are applied to better describe data. The major offsets for Q2 are 1 mm down and 1.5 mrad clockwise rotation with respect to the central line. Others are small adjustments for the fields of magnets, distances between each system, and x' offsets at the focal plane.

After the forward RAYTRACE code was optimized, matrix elements were generated by fitting from the focal plane information produced by forward simulation back to the target. The HMS matrix elements so generated include beam position variations. The fitting code was a modified version of that used for SOS fitting. The offsets of the generated matrix elements in HMS also were calibrated and shown in Table 3.2.

Set	Target	Aerogel		Beta		$Beta = 0$		Correction	
		Ineff.	Error	Ineff.	Error	Ineff.	Error	Factor	Err.(%)
1	H	.0714	.0062	.0320	.0034	.0494	.0031	1.1704	0.82
	D	.0948	.0083	.0528	.0054	.0659	.0022	1.2486	1.10
2	H	.0725	.0061	.0363	.0036	.0532	.0027	1.1818	0.81
	D	.0955	.0072	.0554	.0048	.0720	.0022	1.2613	0.97
3	H	.0552	.0067	.0238	.0033	.0477	.0029	1.1385	0.84
	D	.0671	.0069	.0316	.0040	.0646	.0024	1.1835	0.88
4	H	.0393	.0075	.0212	.0051	.0539	.0053	1.1241	1.09
	D	.0441	.0078	.0316	.0060	.0553	.0034	1.1436	1.08
5	H	.0654	.0098	.0408	.0072	.0548	.0041	1.1802	1.36
	D	.0521	.0053	.0330	.0040	.0362	.0020	1.1320	0.73
6	H	.0621	.0122	.0288	.0063	.0547	.0046	1.1615	1.53
	D	.0494	.0073	.0350	.0058	.0609	.0036	1.1608	1.05
7	H	.0559	.0112	.0293	.0076	.0629	.0050	1.1644	1.52
	D	.0607	.0089	.0296	.0051	.0408	.0023	1.1437	1.11
8	H	.0457	.0087	.0280	.0071	.0462	.0039	1.1303	1.24
	D	.0400	.0063	.0288	.0059	.0230	.0013	1.0978	0.91
9	H	.0567	.0035	.0362	.0029	.0513	.0025	1.1594	0.55
	D	.0582	.0031	.0347	.0025	.0648	.0017	1.1763	0.45
10	H	.0581	.0063	.0424	.0055	.0493	.0030	1.1661	0.94
	D	.0552	.0052	.0406	.0046	.0603	.0025	1.1740	0.78
11	H	.0529	.0045	.0513	.0050	.0402	.0024	1.1596	0.75
	D	.0544	.0043	.0306	.0027	.0427	.0014	1.1395	0.55

Table 3.3: Kaon PID cut efficiencies for all settings.

Acceptance cuts for both data and SIMC		
$\lvert hsdelta \rvert$	$<$	8. (%)
$\lvert hsxptar \rvert$	$<$	0.08 (rad)
$\lvert hsyptar \rvert$	$<$	0.04 (rad)
$\lvert ssdelta \rvert$	$<$	20. (%)
$\lvert ssxptar \rvert$	$<$	0.04 (rad)
$\lvert ssyptar \rvert$	$<$	0.07 (rad)
		PID cuts only for data
$\lvert cointime - 0.25 \rvert$	$<$	1.002 (ns) ; coincidence time cut for real events
$\lvert \beta - \beta_p \rvert$	$<$	0.04 (rad) ; SOS beta
saernpe	$<$	3. ; number of aerogel Čerenkov photoelectron
hcernpe	$>$	2. ; number of HMS Čerenkov photoelectron

Table 3.4: All cuts summary table for kaon production data and SIMC.

3.5 Particle Identification

During the analysis of the **E91-016** data, the preliminary step is to select a clean sample of kaons free of contamination by other charged particles, especially pions. Fortunately, the detector packages in the HMS and SOS, operating within design specifications, yielded clean samples of kaons coincident with scattered electrons. All of the cuts to select good coincidence kaons are shown in Table 3.4. Especially good scintillator hodoscope timing resolution ($\sim$ 150 ps σ) provided good separations between kaons, pions, and protons. This led to a precise evaluation of the cut inefficiencies that are presented in Table 3.3.

3.5.1 Electrons

Since pions and electrons are not separable by TOF at high momentum, to select clean electrons in HMS, a Čerenkov cut ($>$ 2 photo-electrons), was applied to eliminate the pion background. In a detailed study [38], the efficiency of this cut is $>$ 99.8 %.

3.5.2 Aerogel Čerenkov

In order to reduce data counting rates, and unnecessary random background, the aerogel Čerenkov veto trigger in the SOS was set to veto particles with $\beta > 0.98$. Also, runs with no aerogel veto in the trigger runs had been taken to calibrate the kaon efficiency. From the comparison between runs with and without aerogel trigger, shown in Fig. 3.1, the extracted pion rejection efficiencies were found to be about 85%.

In addition, possible kaon losses resulting from the aerogel trigger were carefully tested by comparison of lambda yields within defined missing mass spectrum regions. The test results for these kaon losses are shown in Table 3.5.

	Normalized kaon yield
Without aerogel TR. runs	311.2 $\pm$7.1
With aerogel TR. runs	305.0 $\pm$4.8

Table 3.5: Comparison of normalized and efficiency corrected kaon yields within missing mass 1.1-1.14 GeVregion.

Therefore, an Aerogel trigger inefficiency correction was not applied during

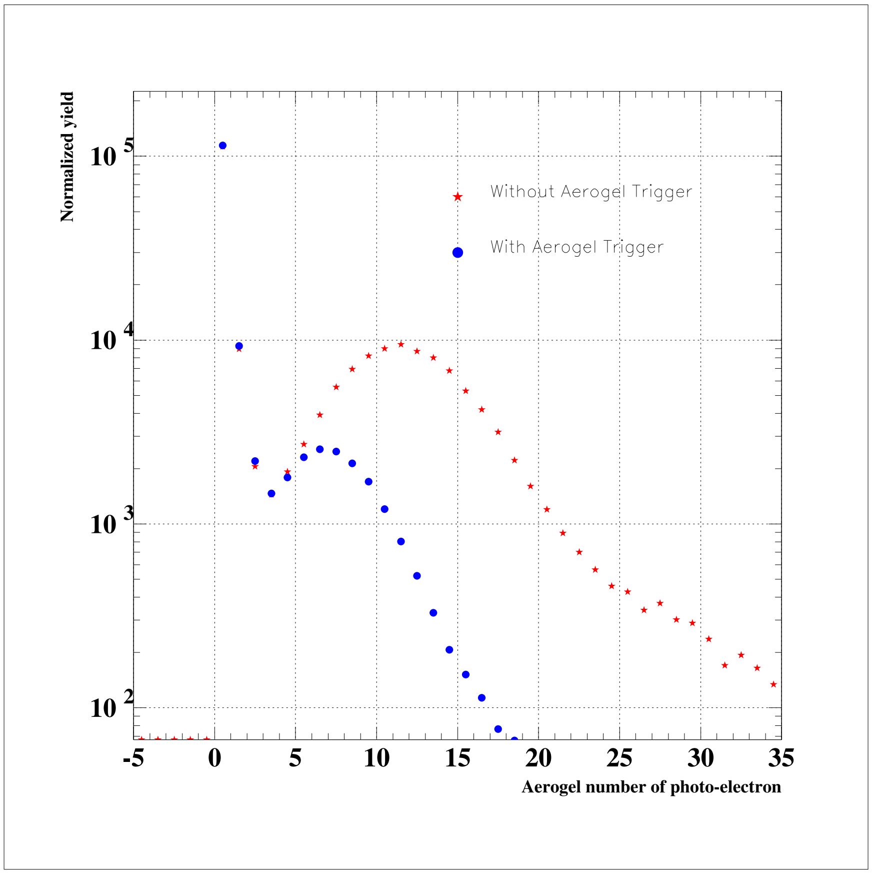

Figure 3.1: Comparison of normalized yield with and without aerogel trigger. With this hardware cut, the number of photoelectrons in aerogel Čerenkov ≤ 7, was applied online and reduced the trigger rate by ~ 35 %.

kaon analysis. During off-line analysis, to select clean kaon events, a software aerogel cut for fewer than 3 photoelectrons were applied. The inefficiencies of this off-line aerogel cut are shown in Table 3.3.

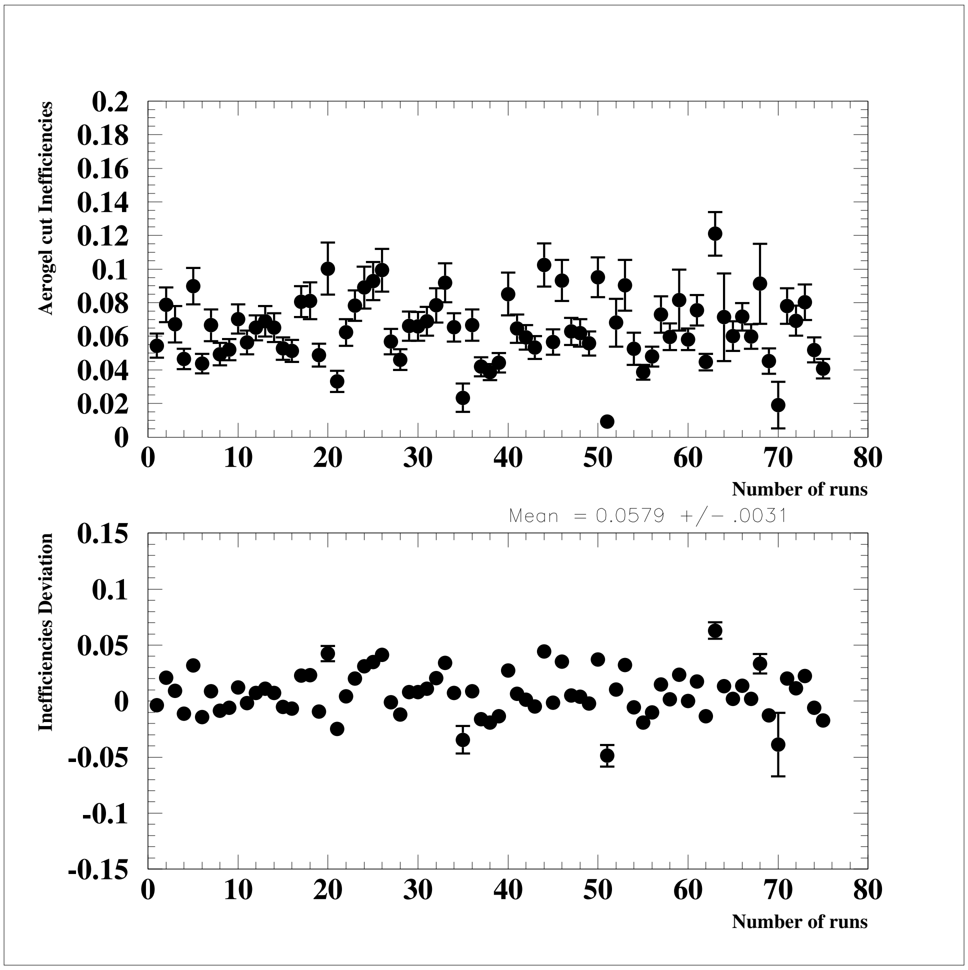

Figure 3.2: Kaon inefficiency distributions with aerogel software cut, for fewer than 3 photoelectrons. The indicated runs belong to a forward kinematic setting at $Q^2 = 0.38$ GeV^2.

3.5.3 Coincidence Time

As mentioned previously, good coincidence timing is the most important and useful information that is used to achieve clean real kaon yield and to measure the inefficiencies of most cuts. In spite of good timing resolution, the time of flight measured via the four hodoscope planes could not be extrapolated to the target in order to produce a suitable corrected coincidence time. Therefore, a value for beta derived from momentum information has been used, and all events are treated as kaons or electrons; $\beta_p = \mathrm{p}/\sqrt{p^2 + M^2}$, where p is the momentum and M the mass of electron for HMS and mass of kaon on the SOS side. Since electron beam bunches are delivered to Hall C at 2.004 ns intervals, the beam bunch structure appears in Fig. 3.3. In this figure, the vertical axis is the difference between beta extracted from the hodoscope planes and the velocity β_p from momentum in vertical axis.

To select real kaons without the disturbance from real pions, the real cut was that $|\bar{t}_{coin} - t_{coin} - 0.25| < 1.002$ where t_{coin} is a coincidence time for real kaons and $\bar{t}_{coin}$ the mean value. The random events were selected by the cut, $|\bar{t}_{coin} - t_{coin} - 0.25 + 9.0| < 4.008$, then normalized dividing by 4 before being subtracted. The inefficiency of this cut is mostly related to coincidence blocking events. During **E91-016**, coincidence blocking events are about 3 % of whole data.

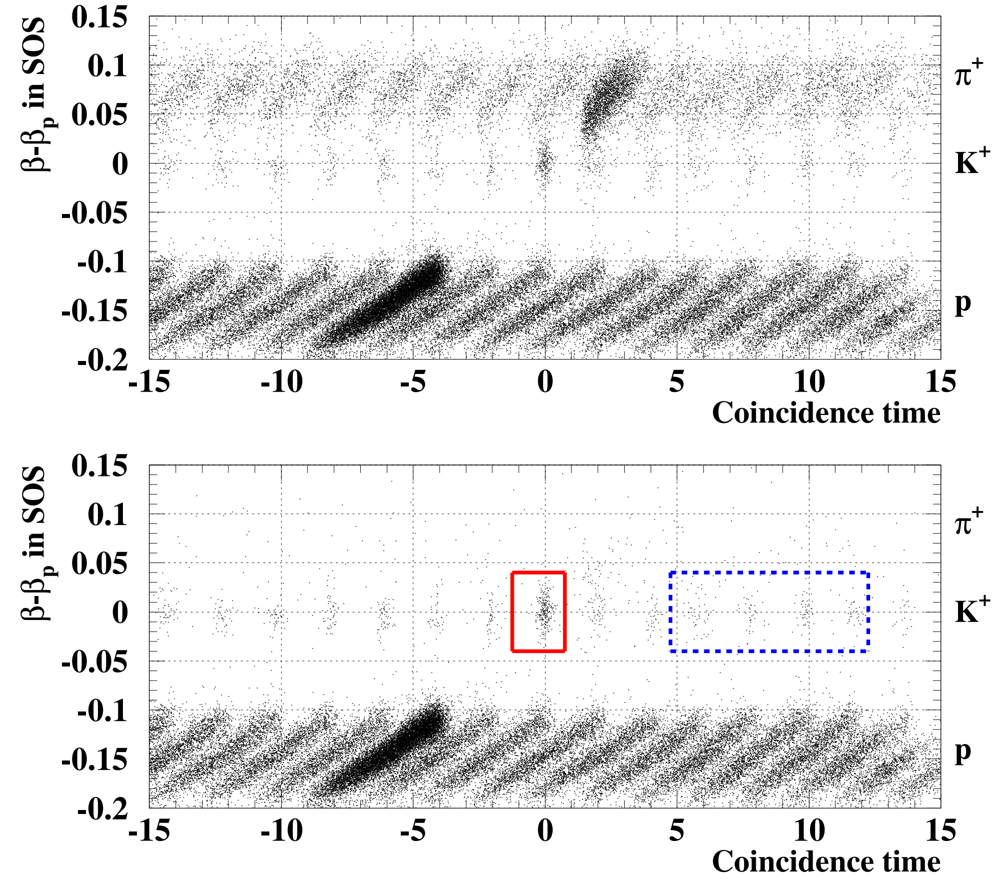

Figure 3.3: Real and random events in path-length corrected coincidence time before applying any hadron particle identification cuts (top), including aerogel veto trigger with > 7 photo electrons; bottom plot including aerogel < 3. NPE. The box with solid lines indicate cut boundary for real events and dotted lines for random.

To evaluate the inefficiency of coincidence time cuts or the coincidence blocking, the data on $H(e, e'\pi^+)n$ reaction have been used. Among the coincidence blocking events, only 1/3 of the events were good real events. Therefore, the inefficiency of coincidence or blocking applied ≈ 1 %.

3.5.4 Hadron Beta

The hadron beta cut was chosen from the difference between the β measured by TOF in the hut and the β calculated from the momentum, β_p. If the difference was less than 0.04, the events were selected to be kaons. The efficiency of the beta cut in SOS is measured by comparing the number of events that pass all cuts to the number that pass all but the beta.

If the projection of the track from the drift chamber did not meet with the corresponding paddle in the hodoscope planes, the events are defined as $\beta = 0$ in the engine replay. These $\beta = 0$ events are obviously eliminated when the $|\beta - \beta_p| < 0.04$ cut was applied. Since the efficiency of the beta cut is evaluated only with events with the $\beta > 0$ cut, the two beta cut efficiencies are measured separately. The inefficiencies of these beta cuts are shown in Table 3.3.

3.6 Kaon Decay Corrections

Since the kaon is an unstable particle, with a mean life time $\tau = (1.2371 \pm 0.0029) \times 10^{-8} s$, many kaons created at the target decay into secondary particles before detection. For the nominal kinematic settings in **E91-016**, about 70% of kaons produced decay despite the short total flight path-length, $\approx$ 9.5 m. Secondary particles from kaon decay affect the selection of good kaons. Because of the difficulties in discriminating decay events from good data, this problem has been carefully evaluated with use of Monte Carlo simulations.

Decay Modes	Branching Ratio (%)	p (MeV/c)
$\mu^+\nu_\mu$	63.51 ± 0.18	236
$\pi^+\pi_\circ$	21.16 ± 0.14	205
$\pi^+\pi^+\pi_-$	5.59 ± 0.05	125
$\pi^\circ e^+\nu_e$	4.82 ± 0.06	228
$\pi^\circ\mu^+\nu_\mu$	3.18 ± 0.08	215
$\pi^+\pi^\circ\pi_\circ$	1.73 ± 0.04	133

Table 3.6: Table of K^+ decay channels. p is the momentum of each decay product for 2-body decay and the maximum momentum of any the decay products for 3-body decays in the rest frame. Other channels with branching ratio less than 1% are not shown.

For simulation of kaon decay, SIMC, discussed in next chapter, is used. This simulation, SIMC, includes SOS spectrometer acceptance, detector aperture cuts and the decay modes shown in Table 3.6. The kaon survival probability is calculated using well-known function;

$$P(x) = e^{-Mx\Gamma/|\vec{p}|}, \tag{3.1}$$

where:

- $P(x)$ is the probability for a kaon not to decay after traveling a distance x,

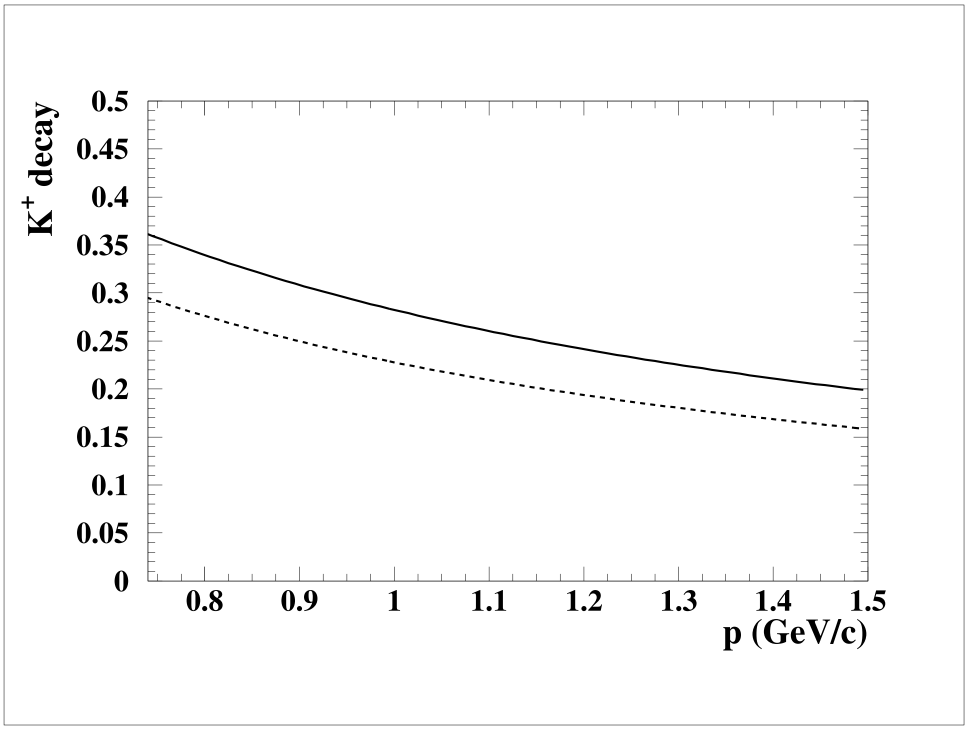

Figure 3.4: Kaon decay rate within hut. The solid and dotted lines indicate the decay rate from focal plane to S2Y hodoscope plane and between the second drift chamber and S2Y hodoscope plane, respectively.

- M is the mass of kaon,
- x is the distance traveled,
- $\Gamma = 1/\tau$ is the inverse of the mean lifetime, $\approx$ 12.4 ns for a kaon [39],
- $\vec{p}$ is the momentum of the kaon.

Since events that decay within the SOS spectrometer do not reach the hut, the primary concerns are mainly kaon decay between the field boundary of the last dipole of SOS and the aerogel. In the kaon decay Monte Carlo simulation inside the hut, most decay events are rejected with detector aperture cuts. To evaluate

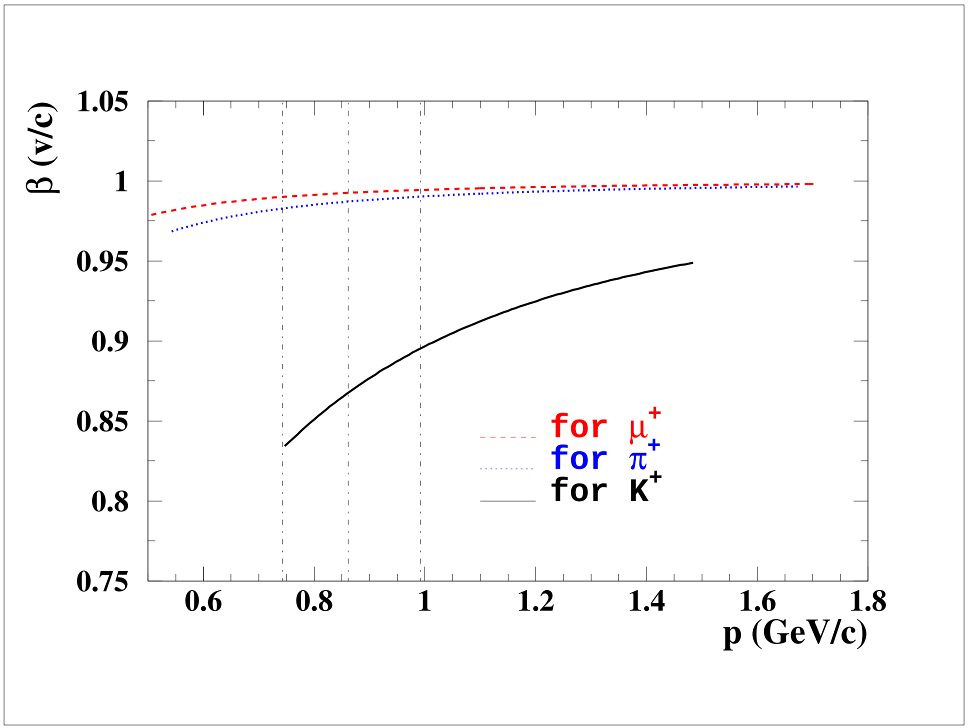

Figure 3.5: Beta vs. momentum for π, μ, and K^+. Each vertical line corresponds to the lowest momentum point(SOS $\delta = -20$ %) for each setting.

the contribution of secondary particles which pass proper kaon PID cuts, two additional cuts are defined in the simulation and applied to decay final particles. One is nominal beta range cuts being the same as the kaon beta range $|\frac{p-p_\circ}{p_\circ}| \leq 0.2$, the other is the restricted beta cut, $\beta \leq 0.986$, which is equivalent to the threshold of the aerogel Čerenkov pretrigger. Since all kaon events where the number of photo-electrons in the aerogel is greater than 3 are included in the aerogel Čerenkov inefficiency correction, it is necessary to determine the fraction of decay events to account for double decay correction.

3.7 Absorption

Absorption of electrons in the target and the HMS spectrometer was negligible. In contrast, kaons interact significantly with the materials they pass through in the target and the SOS spectrometer. A list of all materials with their thickness, densities, and radiation lengths is given in Table 3.7 and 3.8. The eikonal approximation of Weise [40] gives the following formula for the kaon interaction cross section with matter,

$$\sigma = A\sigma_{KN}(1 - \frac{3\sigma_{KN}}{8\pi {r_0}^2}(1 - B^2)A^{1/3}), \qquad (3.2)$$

where A is the number of nucleons, σ_{KN} is the kaon-nucleon cross section, r_0 is 1.2 fm, and B is the ratio of the real and imaginary parts of the forward kaon-nucleon scattering amplitude. Using kaon-proton cross sections from the Particle Data Group [41] and kaon absorption data on carbon [42], a parameterization for B as a function of momentum p is derived [43] to be

$$B = 0.82119 - 0.11274 * p. \qquad (3.3)$$

Material	t(cm)	rho(g/cm^3)	$X_0(g/cm^2)$	r.l.(%)	Notes
			Target		
Entrance cap	0.0071	2.7	24.01	0.080	2.8 mil Al
LH2	4.36	0.0723	61.28	0.514	
LD2	4.17	0.1670	122.6	0.568	
Exit cap	0.0137	2.70	24.01	0.155	5 mil Al
Chamber exit	0.0406	2.70	24.01	0.457	16 mil Al
			Spectrometer		
Air	≈ 15	0.0021	36.66	≈ 0.050	
Kevlar entrance	0.0381	0.74	55.2	0.051	15 mil Kevlar
Mylar entrance	0.0127	1.39	39.95	0.044	3 mil Mylar
Kevlar exit	0.0381	0.74	55.2	0.051	15 mil Kevlar
Mylar exit	0.0127	1.39	39.95	0.044	5 mil Mylar
			Hut		
Air	≈ 35	0.00121	36.66	≈ 0.116	
DC Mylar	0.0102	1.39	39.95	0.036	
Ar/CH_4 gas	21.6	0.00154	≈ 25.7	≈ 0.129	
Sense Wires(W)	0.00006	19.3	6.76	0.017	$12 \times 25\mu m$ wires
Field Wires(W)	0.00212	≈ 3.5	≈ 25	≈ 0.030	$12 \times 125\mu m$ wires
Air	≈ 210	0.00121	36.66	≈ 0.693	
S1X	1.067	1.03	43.8	2.510	1.067 for overlap
S1Y	1.067	1.03	43.8	2.510	1.067 for overlap
CER entr.	0.1	2.70	24.01	1.125	
CER gas(Freon)	≈ 150	0.0025	≈ 23.7	≈ 1.582	Density for .5 atm.
CER morror	-	-	-	≈ 0.5	
CER exit	0.1	2.70	24.01	1.125	
S2X	1.067	1.03	43.8	2.510	1.067 for overlap
S2Y	1.067	1.03	43.8	2.510	1.067 for overlap
Air	≈ 18	0.00121	36.66	≈ 0.060	
Calorimeter	40	-	-	≈ 1600	

Table 3.7: Table of HMS materials. These table entries are used to calculate kaon aborption and mulitple scattering. The numbers are used in the Monte Carlo simulation for multiple scattering.

Material	t(cm)	rho(g/cm^3)	$X_0(g/cm^2)$	r.l.(%)	Notes
			Target		
Entrance cap	0.0071	2.7	24.01	0.080	2.8 mil Al
LH2	4.36	0.0723	61.28	0.514	
LD2	4.17	0.1670	122.6	0.568	
Exit cap	0.0137	2.70	24.01	0.155	5 mil Al
Chamber exit	0.0203	2.70	24.01	0.288	8 mil Al
			Spectrometer		
Air	≈ 15	0.00121	36.66	≈ 0.050	
Kevlar entrance	0.0127	0.74	55.2	0.017	5 mil Kevlar
Mylar entrance	0.0076	1.39	39.95	0.027	3 mil Mylar
Kevlar exit	0.0381	0.74	55.2	0.051	15 mil Kevlar
Mylar exit	0.0127	1.39	39.95	0.044	5 mil Mylar
			Hut		
Air	≈ 15	0.0021	36.66	≈ 0.050	
DC Mylar	0.0178	1.39	39.95	0.062	14 planes
Ar/CH_4 gas	7.41	0.00154	≈ 25.7	≈ 0.044	
Sense Wires(W)	0.00008	19.3	6.76	0.022	$12 \times 30\mu m$ wires
Field Wires(W)	0.00034	19.3	6.76	0.098	$12 \times 60\mu m$ wires
Air	≈ 49.5	0.0021	36.66	≈ 0.1633	
S1Y	1.098	1.03	43.8	2.582	1.098 for overlap
S1X	1.04	1.03	43.8	2.446	1.04 for overlap
CER entr.	0.05	2.70	24.01	0.056	
CER gas(Freon)	≈ 100	0.0051	≈ 23.7	≈ 2.152	Density for 1 atm.
CER morror	-	-	-	0.5	
CER exit	0.05	2.70	24.01	0.056	
S2Y	1.098	1.03	43.8	2.582	1.098 for overlap
Aerogel entr.	0.0625	2.70	24.01	0.70	
Aerogel	9.0	-	-	≈ 6	
Aergel exit	0.0625	2.70	24.01	0.70	
S2X	1.04	1.03	43.8	2.446	1.04 for overlap
Air	≈ 20	0.00121	36.66	≈ 0.066	
Calorimeter	40	-	-	≈ 1600	

Table 3.8: Table of SOS materials. These table entries are used to calculate kaon aborption and mulitple scattering. The numbers are used in the Monte Carlo simulation for multiple scattering.

Kaon momentum p (GeV)	Absorption (%) in SOS
1.0	5.5
1.1	5.8
1.2	6.3
1.3	6.0
1.4	6.0
1.5	5.9
1.6	5.8
1.7	5.8
1.8	5.8
1.9	5.7
2.0	5.7

Table 3.9: Kaon absorption in the SOS [43].

Kaon absorption data on copper [42] is well fitted through the use of this formula, validating the general use of the formula. Application to the SOS materials leads to kaon absorption ranging from 5-7 %, with the explicit momentum dependence shown in Table 3.9.

3.8 Hodoscope Trigger Efficiencies

Three out of four hodoscope planes having fired was chosen in the trigger logic during **E91-016**. This 3-out-of-4 hodoscope trigger efficiency is almost 100 % in HMS and SOS.

3.9 Dead Time Corrections

Because of high counting rates in both HMS and SOS, some events are lost, i.e. not processed correctly. These are termed dead-time losses and correction must be applied.

3.9.1 Electronic Dead Time

When two signals from different events try to activate the logic gate module within a short time, the later event is usually lost. The first signal opens the 30 ns width gate of the logic module. If the second event signal reaches the same module before the gate is closed, this event is ignored. Such loss during triggers is called electronic dead time, and determined by comparing the number of triggers when using 30, 60, 90 and 120 ns width logic gate windows. The algorithm for electronic dead time extraction can be found in [23]. During **E91-016**, the width of most of the output signals in the trigger logic was 30 ns. The weighted mean values of HMS and SOS electronic dead times for all kinematic settings are shown in Table 3.1.

3.9.2 Computer Dead Time

The computer dead time is defined as the events lost because a hardware trigger is formed during the time that the DAQ is busy processing the previous event. The Hall C DAQ can process the events with ~ 400 μs time intervals or an event rate, ~ 2.5 kHz. During **E91-016**, the data rate was approximately 1 kHz. This high trigger rate led to significant dead time. The weighted mean values of computer dead time for all kinematic settings are shown in Table 3.1.

The computer deadtimes are calculated by dividing the difference between pretrigger and trigger by pretrigger events.

CHAPTER 4

MONTE CARLO SIMULATION

The Monte Carlo simulation (SIMC) is based on a code written by N. Makins and T.G. O'Neill for SLAC experiment NE-18 at SLAC [44]. It has been adapted to the Hall C configuration and modified by Doug Koltenuk [22] for kaon electroproduction at Hall C. The simulation modeled the optical properties of the two Hall C spectrometers (HMS and SOS), multiple scattering and energy loss for given passing material, radiative processes. Added new routines are kaon decay, and a momentum distribution of the proton in deuteron from the Bonn potential [22]. The adequacy of simulation has been tested by comparison with elastic scattering, (e,e') and $(e,e'p)$, data. It is known to reproduce $(e,e'p)$ within ± 3 %. By comparison of the simulated yield with the measured yield, the produced cross sections are extracted in an iterative procedure.

4.1 Event Generation

The simulation first selects the reaction position within the target cell and also considers beam position due to rastering. Then it generates the 4-vectors of the electron randomly and uniformly over a range greater than the limits of the HMS spectrometer. The direction of the kaon is generated with two polar angles.

Finally, the momentum of the kaon is calculated from the selected angle and the electron momentum vector with either a Λ or Σ hyperon in the final state. These five independent variables make up the parameters for the electroproduction five-fold differential cross section. A weight factor based on the five-fold different cross section is calculated from the invariant quantities, Q^2, W, t, and ϕ.

For $D(e, e'K^+)YN$, the 4-vector for the target nucleon has to be known in order to solve the kinematics for the final system. The deuteron wave function from the Bonn potential is used to determine the initial momentum distributions of the struck nucleon [22].

4.2 Transport through Spectrometer

After generating momenta and angles at the reaction position in the extended liquid target as mentioned in section 4.1, these quantities are transported through the spectrometers (HMS and SOS) and up to the huts. The trajectory through each spectrometer is determined by a set of matrix elements that transport the particle through the magnetic elements to the detector hut. The matrix elements are derived from the COSY INFINITY [27] transport program based on measured field maps or design specifications. In the both SOS and HMS, the matrix elements are sequential. Individual matrices are applied for different sections of the spectrometer. After each section, the corresponding aperture of the collimator, the magnets, or the detector elements, are included in the model, and particles that go outside of these aperture are thrown out. Also the energy loss and multiple scattering are calculated and corrections applied after any material listed in Table 3.7 and 3.8.

Multiple scattering can take place anywhere in the spectrometer: in the target, at vacuum windows, in air, on drift chamber wires, or in scintillator paddles. The simulation calculates multiple scattering at all of these places. For a realistic model of drift chamber resolutions, the position of the particle in each chamber was generated. To fit the measured wire chamber resolution, two Gaussians are used. One is for less than six hits in a drift chamber. It has a narrow Gaussian distribution. The other is for the events with more than six hits. This Gaussian is three times as broad, but with much lower probability. This effect is modeled by increasing the smearing factor by the percentage of data events with more than six hits [22]. After the final focal plane quantities are obtained, they are used to calculate the reconstructed event quantities at the target. The reconstruction matrix elements are an inversion of the forward matrix elements used to transport from the target to the focal plane.

4.3 Radiative Corrections

The radiative code in the Monte Carlo simulation is quite similar to the code found in the original version of the simulation, so that a detailed description will not be given here (for more details in [45], [46]). The minor modification

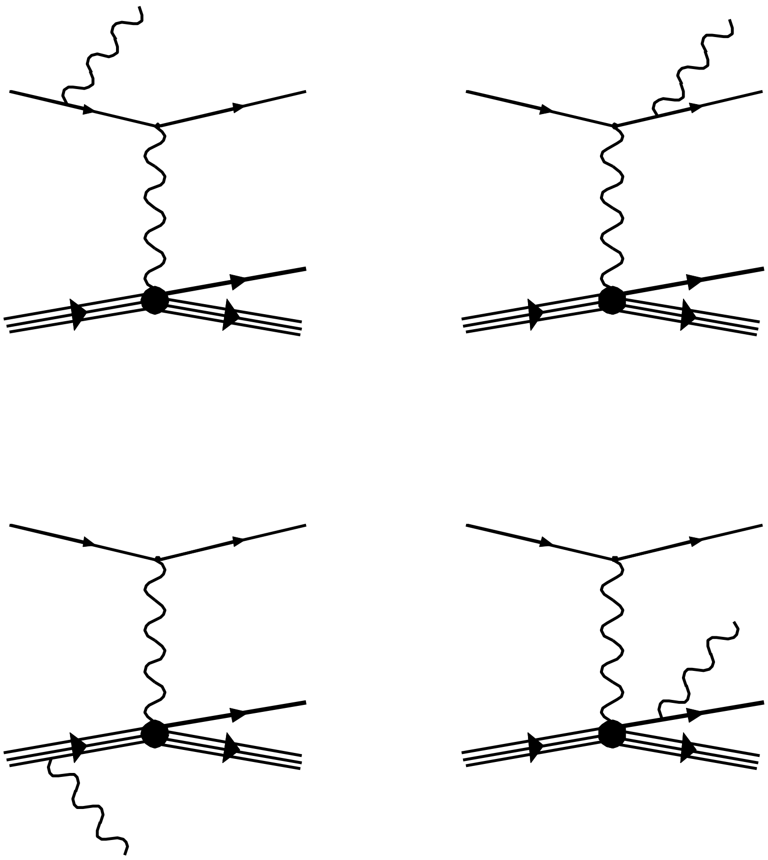

Figure 4.1: Feynman diagrams for the internal hard corrections processes contributing to the measured cross section.

for kaon electroproduction involves the same approximations used in calculating the radiative corrections for $p(e, e'p)$ with the kaon mass replacing the proton mass. Since the contribution to the radiative corrections that is directly related to the outgoing hadron should be small, this approximation should suffice. All the contributions to radiative corrections are calculated, both external Bremsstrahlung and internal (hard and soft). The relative probability for radiation in each arm (incoming electron, outgoing electron, and outgoing kaon) is computed, and the radiated photon is assigned to be in a particular arm based on this probability. If the outgoing electron will not fall into the spectrometer delta acceptance without being radiated, the radiated photon is forced to be in that arm, and the events weighted by the relative probability that the outgoing electron would have radiated. The initial range of outgoing electron momenta thrown is verified to be large enough to include all events that might radiate into the acceptance. However, a range of final electron momenta is not determined such that an individual event would fall into acceptance, a process that would add another weight to the radiative correction and would make the calculation of the overall weight much more complicated.

The external Bremsstrahlung radiation is real photon emission in the field of a nucleus different from the target, thereby reducing the energy of the radiating particle, causing modification of the beam energy at the interaction vertex and a change in kinematics. The same modification is also applied to the outgoing particles momenta because of external Bremsstrahlung.

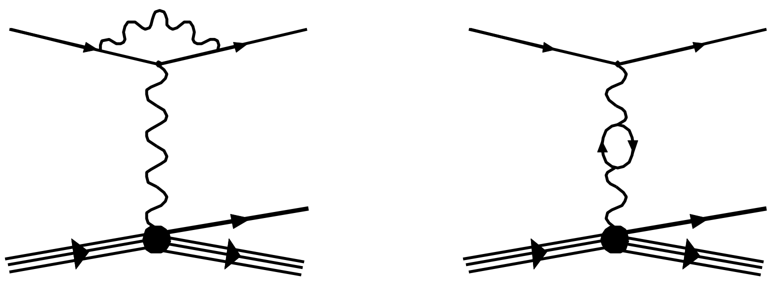

Figure 4.2: Feynman diagrams for the external hard corrections.

Internal Bremsstrahlung radiation can be further divided into soft and hard processes. The soft radiative correction, shown in Fig. 4.1, involves the emission of real photons in the coulomb field, of the target with reduction of the energy of the radiating particle. The difference between internal and external soft radiative corrections is that the internal amplitudes must be added coherently, thereby leading to interference terms. The hard radiative correction is calculated by QED, as shown in Fig. 4.2. These process do not include the emission of real photons and the modification of vertex kinematics. Since the final states for the internal hard processes are indistinguishable from that of the Born term diagram, they represent a background underneath the cross section that we are trying to measure. Each event is given a multiplicative weighting factor to compensate for the influence of these diagrams.

The radiated photon is fixed in direction to be in the same direction as the particle from which it radiated, this assignment is termed the peaking approximation. The calculated energy of this photon is based on a ω^{r-1} distribution function, where r (a positive number much less than one) is determined by the formulas used for radiative correction (see Fig. 4.3). If the initial electron radiates, the entire event is reprocessed. If one of the final particles radiates, only the 4-vector for that particle is modified. All photon radiation takes place at the vertex. In the end, radiative weights are combined with the physics cross section weight.

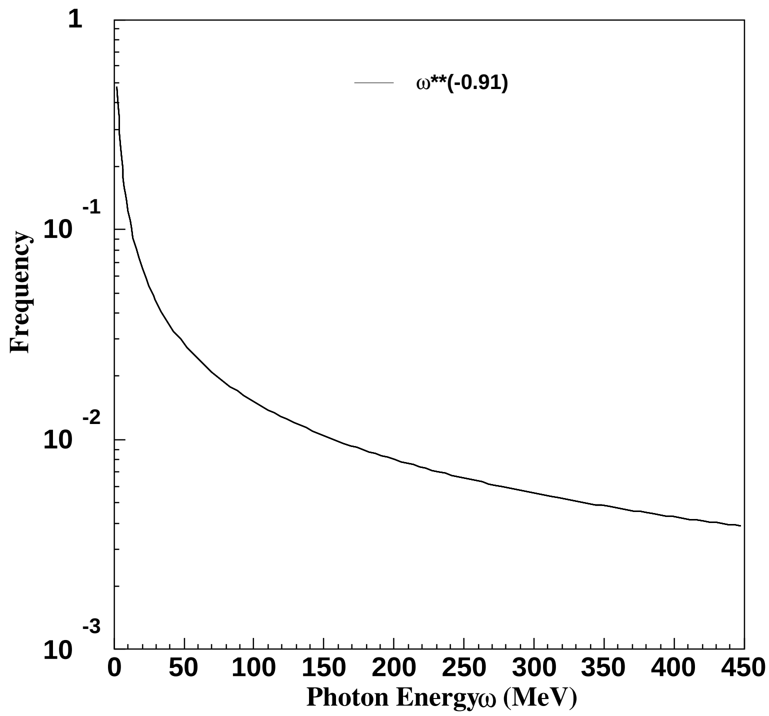

Figure 4.3: Radiated photon distribution for r=0.09, normalized such that the frequency at $\omega = 1$ is equal to one [22].

4.4 Decay Weight

In the Monte Carlo simulation, the survival probability from the target to Aerogel for each kaon is calculated on an event-by-event basis using Eq. 3.1. This calculated probability is included in the weight factor. As mentioned previously, see section 3.6, the over correction for kaon decay is simulated and taken into account.

4.5 Weighted Yields and Cross Section

Both the number of successful events and the number of tries are tabulated. Combining the ratio of the successes to tries with the initial five-dimensional generation volumes gives the e-K coincidence acceptance of the spectrometers. The modified vertex quantities due to energy loss and multiple scattering are recalculated in the center-of-mass system. Then the initial model cross section in the center-of-mass is converted to the laboratory system by multiplication of Jacobian and virtual photon flux, as in Eq. 4.1. This transformed cross section is included in the weight factor for simulated yield. The simulation yield is computed by including target normalizations as well as Monte Carlo weights (decay, radiative correction, spectrometer acceptance, and initial model cross section mentioned in previous sections). The overall yield can be compared with the data. A cross section is extracted from the data by multiplying the average cross section in the Monte Carlo simulation by the scaling factor necessary to match the simulation to the data. Further detailed description of the parameterized cross section will be discussed in Chapter 5.

$$\frac{d^5\sigma}{dE_{e'}d\Omega_{e'}d\Omega_K} = \Gamma J \frac{d\sigma}{d\Omega_K{}^*} \tag{4.1}$$

where the virtual photon flux, Γ, is

$$\Gamma = \frac{\alpha}{4\pi^2}\frac{E\prime(W^2 - M^2)}{EMQ^2(1-\epsilon)} \tag{4.2}$$

and the Jacobian between the CM and Laboratory, $J = d\cos\theta^*/d\cos\theta$.

CHAPTER 5

PHYSICS ANALYSIS AND RESULTS

5.1 Overview

This section describes the extraction of the differential cross section for kaon electroproduction. For hydrogen, the clear separation of the Λ and Σ hyperons (Fig. 5.1) provides an experimental way of understanding the (Q^2, W, t, ϕ) dependence of the cross section when assuming the parameterization of Eq. 5.1 and using an appropriate binning of the data. For the relatively small dynamic range covered in the present experiment, we assume that

$$\frac{d\sigma}{d\Omega}(Q^2, W, t, \phi) = f(Q^2)g(W)h(t)i(\phi), \tag{5.1}$$

where $f,\ g,\ h,\ and\ i$ are independent functions of the indicated variables with the other variables fixed. The Λ and Σ^0 production on the deuterium target are, basically, treated in the same way as production on the hydrogen target in a quasi-free model, but with two main differences; the inclusion of the Σ^- production from the neutron and a nucleon momentum distribution taken from the Bonn potential.

In addition, for a better description of the missing mass distribution near the Λ production threshold, the Λ-n Final State Interaction is modeled.

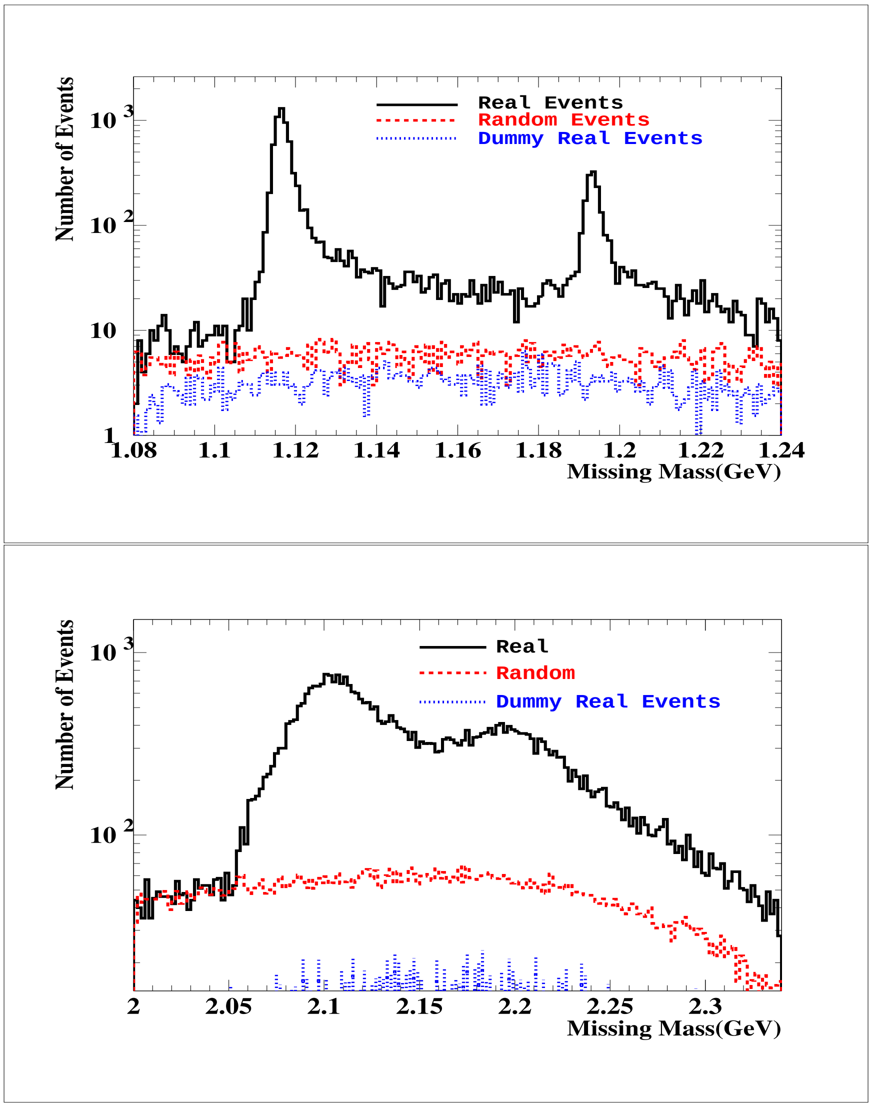

Figure 5.1: Raw missing mass spectra for real and background events for $H(e,e'K^+)Y$(top) and $D(e,e'K^+)YN$(bottom).

5.2 $H(e, e'K^+)$

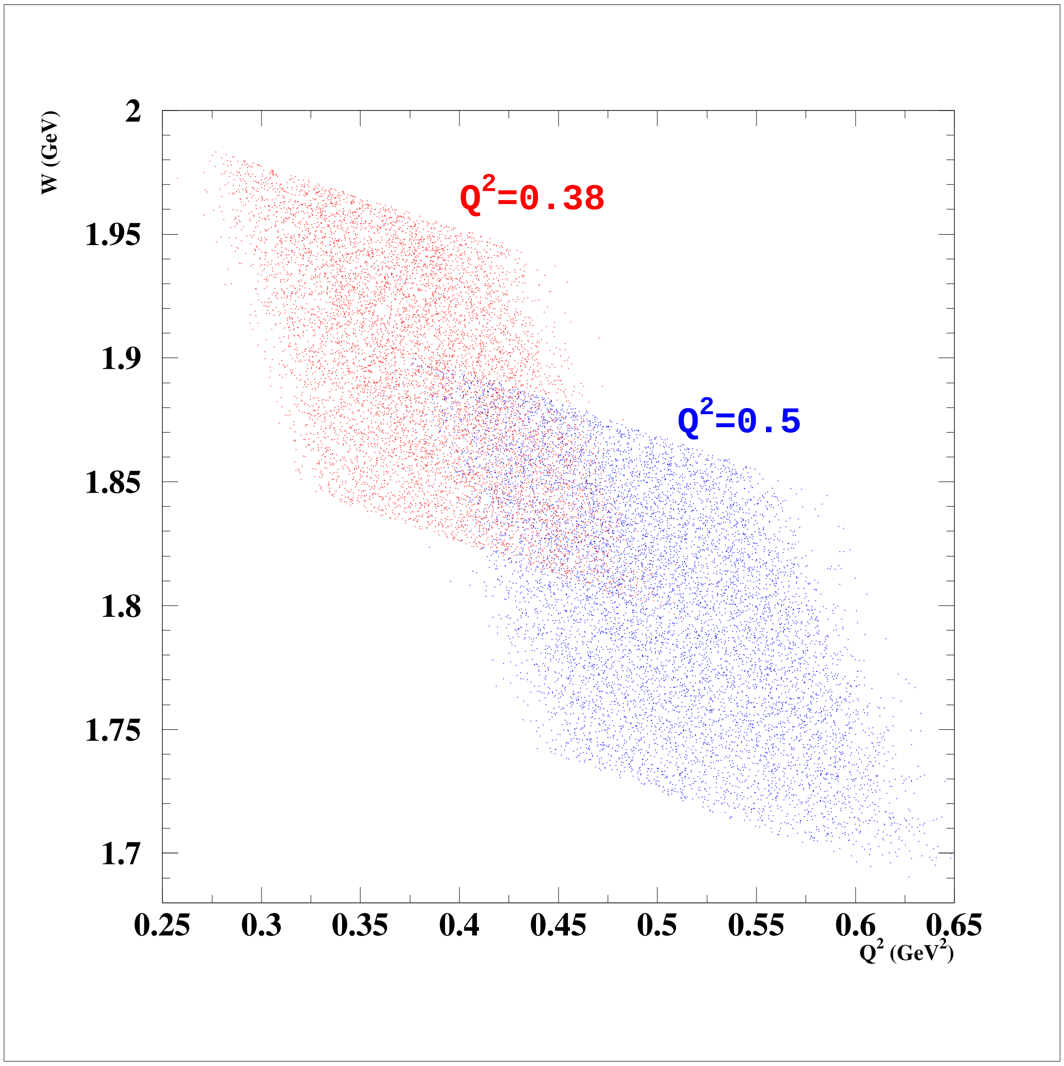

Figure 5.2: W vs. Q^2 coverage for $H(e, e'K^+)\Lambda$ data. The distributions come from the Monte Carlo simulation for $1.1 <$ Missing Mass < 1.16 GeV.

5.2.1 Phase Space Distribution

In **E91-016**, angular distributions of kaon electroproduction have been measured for two different electron kinematic settings ($Q^2 = 0.5$ and 0.38 GeV^2) at one beam energy ($E_{beam} = 3.245$ GeV). For each Q^2 setting, the kaon was detected at laboratory angles ranging from 0° to 13° w.r.t. the virtual photon for each Q^2 setting. For the $Q^2 = 0.5$ GeV^2 setting, an additional angular distribution was taken with the SOS set at a lower momentum (see Table 2.7).

The phase space coverage of experiment **E91-016** for the $H(e,e'K^+)\Lambda$ reaction is shown in Fig. 5.2, 5.3, A.1, A.2, and A.3 for the forward settings only: $W \simeq 1.70$–1.97 GeV, $Q^2 \simeq 0.3$–0.6 GeV^2, $\theta^*{}_{\gamma K}$ ($\theta_{\gamma K}$ in c.m.) $\simeq 0$–$55°$, and $\phi \simeq 0$–$360°$. Within the overlapping region, the physics being the same, our extracted cross sections were also tested for consistency.

P_{sos} setting		Q^2 (GeV^2)	W (GeV)	t (GeV^2)	θ_{cm}(deg.)
	1	0.515	1.769	-0.274	10.89
1.077	2	0.515	1.765	-0.283	14.69
(GeV/c)	3	0.516	1.769	-0.321	25.28
	4	0.516	1.771	-0.384	37.07
	5	0.515	1.767	-0.275	10.92
0.929	6	0.515	1.767	-0.284	14.64
(GeV/c)	7	0.516	1.767	-0.323	25.43
	8	0.515	1.767	-0.388	37.52

Table 5.1: The mean kinematic values for $H(e,e'K^+)\Lambda$ for $1.74 < W < 1.80$ GeV.

Sets 1–4 and 5–8 (Table 2.7) have a large common W and Q^2 coverage for all settings. After applying the same W cuts ($1.74 < W < 1.80$ GeV), shown in

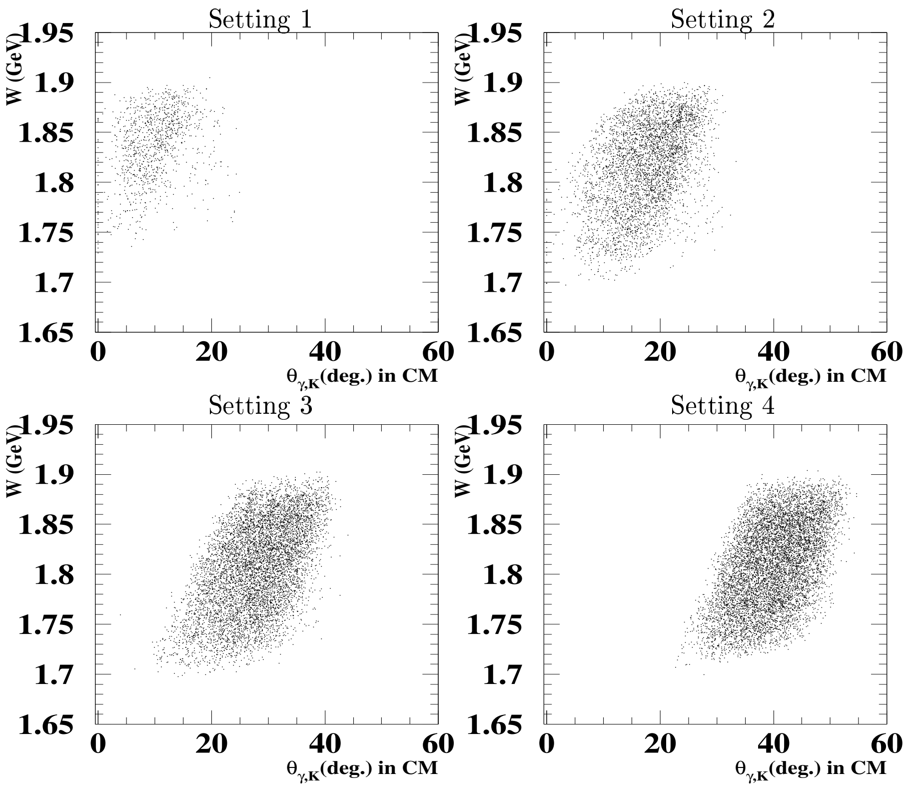

Figure 5.3: W vs. $\theta_{\gamma,K}$ phase space distributions at $Q^2 = 0.5$ GeV^2. All four settings correspond to the same ϕ acceptance: $|\phi - 180°| \leq 24°$, so that the fraction of detected events falling within the cut is smaller at the more forward angle.

Table 5.1, the mean of the Q^2 distribution for all eight angle settings varied little; at the same angle, the other kinematics components, t and θ_{cm}, are also consistent.

The ϕ distributions overlap well (Fig. 5.4), except for the 13° setting. Since the setting for the centroid of the SOS momentum has two values, the corresponding $\delta = \frac{P-P_\circ}{P_\circ}$ distribution of the kaons is shifted (Fig. 5.5). Therefore, one expects a difference in the yields due to different phase space in the SOS. The normalized yield ratio before acceptance correction for each setting is indicated in Table 5.2.1; the discrepancy in the 13° ratios is discussed below. As noted previously, the extracted cross section is obtained after scaling the simulated yield to the data. The Monte Carlo simulation is therefore model-dependent. In other words, the discrepancy between the two SOS momentum settings comes from an inappropriate low momentum weight factor which mainly originates from our understanding of the SOS optics. By comparing data and simulation for the $H(e, e'p)$ elastic reaction at various SOS δ settings, a discrepancy of about 5 % was seen, the simulated yield being lower than the data yield. Correcting for this effect, the cross sections are now of comparable magnitude within the error bars (Fig. 5.6).

kinematic		0.°	4.°	8.°	11.°
Yield Ratio	Data	$1.003 \pm .033$	$1.015 \pm .027$	$0.996 \pm .026$	$0.798 \pm .032$
(Normal/Low)	MC	1.047	1.037	1.002	0.875

Table 5.2: Comparison of the charge normalized yield for Λ production between the SOS delta normal and low settings for $1.74 < W < 1.80$ GeV. The errors in the data ratio are statistical only. The yields calculated from the Monte Carlo simulation use a initial Model cross section before further analysis.

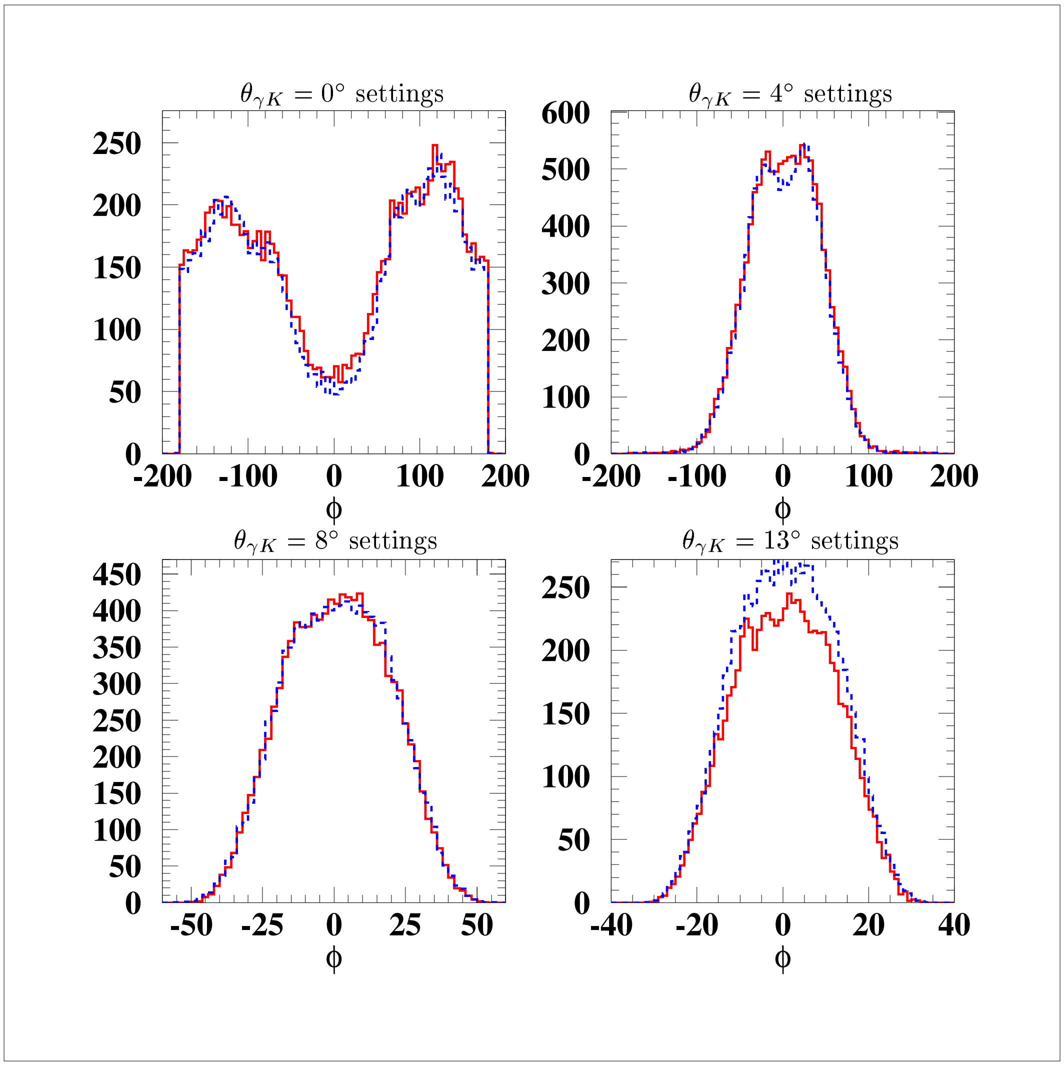

Figure 5.4: Comparison of the ϕ distributions between the SOS normal (P_{SOS} = 1.077 GeV/c) and low (P_{SOS} = 0.929 GeV/c) settings at Q^2 = 0.5 GeV^2 for $1.74 < W < 1.80$ GeV. The charge normalized yields are shown for the normal (solid line) and low (dotted line) settings.

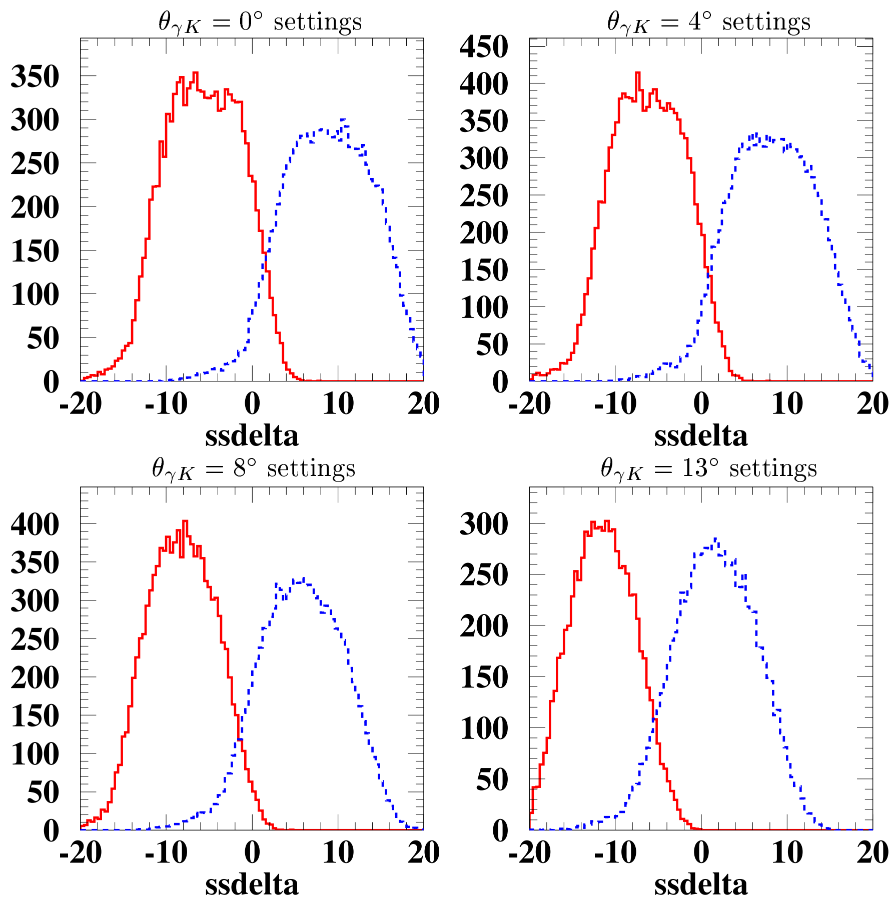

Figure 5.5: Comparison of the δ_{SOS} distribution between the SOS normal ($P_{SOS} =$ 1.077 GeV/c) and low (P_{SOS} = 0.929 GeV/c) settings at Q^2 = 0.5 GeV^2 for $1.74 < W < 1.80$ GeV from our Monte Carlo simulation. The solid and dotted lines are for the normal and low settings, respectively. The shift is a consequence of the change in the central momentum of the SOS.

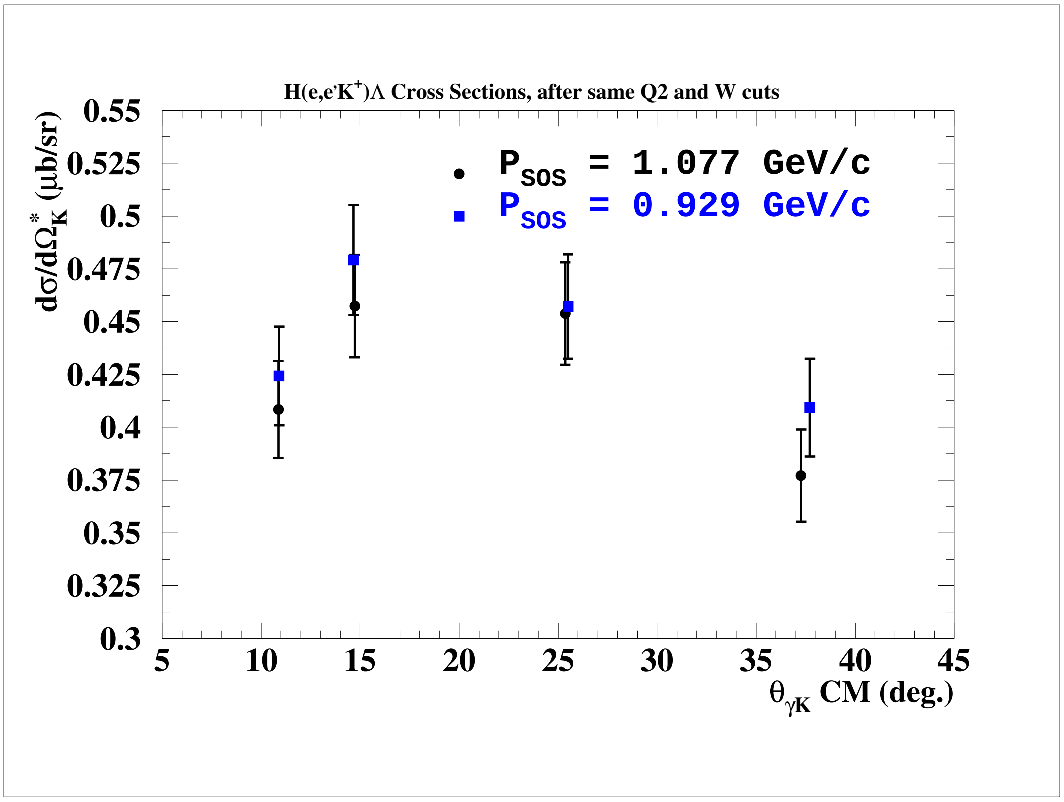

Figure 5.6: Comparison of the cross section between P_{SOS} = 1.077 and P_{SOS} = 0.929 GeV/c settings for the same W and Q^2 cuts which correspond to mean values of $\bar{W}$ =1.77 GeV and $\bar{Q^2}$ = 0.513 GeV^2 for all points. The error bars shown are mainly dominated by a 4.5 % systematic error.

5.2.2 Q^2, W, and t Dependence

Setting numbers	Q^2 (GeV^2)	W (GeV)	t (GeV^2)	θ_{cm} degree	$d\sigma^*/\Omega$ (μb/sr)
1	0.462	1.848	-0.205	8.171	0.517 ± 0.036
1	0.466	1.831	-0.221	11.479	0.435 ± 0.026
2	0.493	1.814	-0.238	10.806	0.590 ± 0.039
2	0.483	1.823	-0.235	13.110	0.435 ± 0.025
2	0.484	1.817	-0.246	15.447	0.428 ± 0.021
2	0.487	1.814	-0.257	17.770	0.410 ± 0.019
2	0.487	1.813	-0.266	20.221	0.420 ± 0.019
2	0.487	1.805	-0.279	22.309	0.435 ± 0.019
3	0.508	1.796	-0.283	20.342	0.462 ± 0.024
3	0.495	1.806	-0.286	23.438	0.423 ± 0.019
3	0.494	1.806	-0.299	25.998	0.412 ± 0.018
3	0.495	1.804	-0.314	28.535	0.388 ± 0.017
3	0.495	1.804	-0.330	31.293	0.406 ± 0.017
3	0.500	1.797	-0.350	33.902	0.396 ± 0.017
4	0.497	1.807	-0.340	33.039	0.356 ± 0.022
4	0.495	1.806	-0.358	35.732	0.352 ± 0.019
4	0.496	1.803	-0.377	38.270	0.350 ± 0.018
4	0.497	1.802	-0.398	41.034	0.336 ± 0.017
4	0.497	1.803	-0.420	43.892	0.349 ± 0.019
4	0.507	1.796	-0.444	46.289	0.315 ± 0.020

Table 5.3: Binned Λ cross sections for all angles at $Q^2 = 0.5$ GeV^2 for the $P_{SOS} =$ 1.077 GeV/c settings for hydrogen. All kinematic values are the mean value of each binned segment. The azimuthal angle, ϕ, ranges are $|\phi - 180°| \leq 24°$

This section describes procedures used to extract the dependence of the $H(e, e'K^+)\Lambda$ cross section with respect to the kinematic variables (Q^2, W, t). The assumption made is that Eq. 5.1 is valid within the spectrometer acceptance.

The comparisons between the experimental data and the initial Monte Carlo simulation for the $H(e, e'K^+)\Lambda$ reaction show a discrepancy in the δ_{SOS} distribution (Appendix B); the data are systematically higher than the simulation in the low

Setting numbers	Q^2 (GeV^2)	W (GeV)	t (GeV^2)	θ_{cm} degree	$d\sigma^*/\Omega$ (μb/sr)
5	0.481	1.786	-0.244	7.468	0.504 ± 0.046
6	0.509	1.775	-0.266	10.015	0.618 ± 0.041
6	0.509	1.774	-0.273	12.921	0.459 ± 0.034
6	0.508	1.774	-0.279	15.496	0.487 ± 0.031
6	0.503	1.774	-0.285	17.763	0.488 ± 0.030
6	0.507	1.763	-0.296	18.709	0.484 ± 0.029
7	0.525	1.763	-0.303	18.849	0.575 ± 0.030
7	0.512	1.774	-0.305	22.530	0.446 ± 0.024
7	0.512	1.776	-0.316	25.330	0.424 ± 0.021
7	0.510	1.778	-0.328	28.143	0.420 ± 0.020
7	0.510	1.775	-0.343	30.697	0.461 ± 0.022
7	0.522	1.754	-0.363	31.772	0.471 ± 0.024
8	0.515	1.777	-0.357	32.965	0.397 ± 0.020
8	0.508	1.786	-0.377	37.081	0.379 ± 0.019
8	0.506	1.789	-0.397	40.154	0.369 ± 0.018
8	0.508	1.784	-0.417	42.713	0.414 ± 0.020
8	0.524	1.760	-0.440	44.495	0.400 ± 0.020

Table 5.4: Binned Λ cross sections for all angles at $Q^2 = 0.5$ GeV^2 for the $P_{SOS} =$ 0.929 GeV/c settings for hydrogen. All kinematic values are the mean value of each binned segment. The azimuthal angle, ϕ, ranges are $|\phi - 180°| \leq 24°$

W, i.e. low δ region for $Q^2 = 0.5$ GeV^2. As a result modifications of the kinematic dependence of the cross section were needed.

The parameterization of the cross section was performed in two different ways. In one case, the data were initially binned by varying only one kinematic variable but fixing the others. The other method consists of binning the data arbitrarily and then iterating the cross section so obtained with the use of a χ^2 fit for a given parameterization.

In the previous section, it is seen that the comparisons between two different

Setting	Q^2 (GeV^2)	W (GeV)	t (GeV^2)	θ_{cm} degree	$d\sigma^*/\Omega$ (μb/sr)
9	0.347	1.938	-0.137	6.254	0.585 ± 0.036
9	0.356	1.923	-0.148	8.742	0.450 ± 0.027
9	0.360	1.915	-0.158	10.995	0.458 ± 0.024
9	0.356	1.906	-0.165	13.044	0.432 ± 0.022
10	0.380	1.903	-0.167	11.247	0.530 ± 0.032
10	0.370	1.908	-0.172	13.936	0.392 ± 0.020
10	0.369	1.905	-0.182	16.377	0.398 ± 0.019
10	0.372	1.901	-0.195	18.897	0.357 ± 0.017
10	0.372	1.899	-0.208	21.589	0.361 ± 0.017
10	0.370	1.893	-0.222	23.952	0.368 ± 0.018
11	0.386	1.895	-0.229	24.376	0.355 ± 0.017
11	0.379	1.896	-0.247	27.571	0.364 ± 0.017
11	0.380	1.893	-0.266	30.236	0.382 ± 0.017
11	0.380	1.892	-0.288	33.132	0.332 ± 0.015
11	0.381	1.888	-0.312	36.119	0.321 ± 0.015

Table 5.5: Binned Λ cross sections for all angles at $Q^2 = 0.38$ GeV^2 settings for hydrogen. All kinematic values are the mean value of each binned segment. The azimuthal angle, ϕ, ranges are $|\phi - 180°| \leq 24°$

phase space regions not only suggest modification of the cross sections used in the simulation, but also show independence of the cross section derived from data analysis upon the model cross section used in the MC simulation.

In addition, only the far forward angle kinematic settings cover the full ϕ acceptance of 0–360°. Therefore, because of partial ϕ distributions, the average cross section for all other settings where $\theta_{\gamma K}^{CM} \neq 0$ includes contributions from the interference terms, σ_{TT} and σ_{LT}. In other words, one has to restrict all settings to the same ϕ coverage in order to extract reliable information on the kinematic dependence of the cross sections for each variable.

To make the appropriate W binning, one kinematic variable was varied

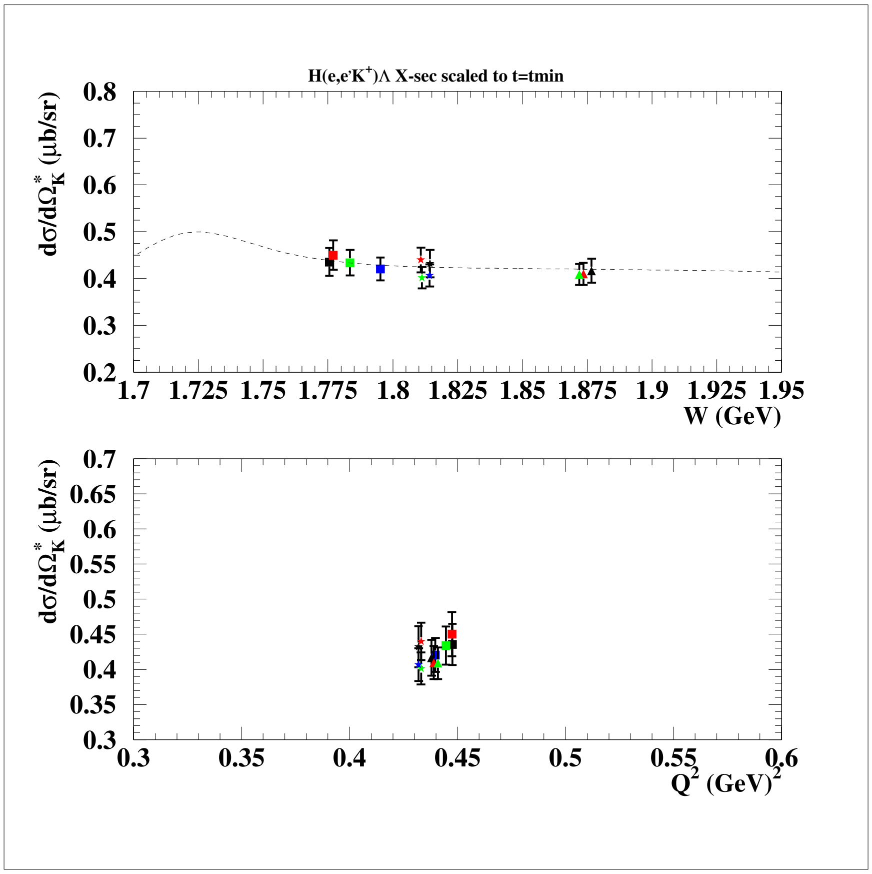

Figure 5.7: $H(e, e'K^+)\Lambda$ cross section W dependence for a narrow Q^2 cut after scaling to $t = t_{min}$ using the function displayed in Fig. 5.11 (top). The bottom figure shows that the Q^2 for all points are roughly equal. The dotted curve is the function used for fitting the W dependence shown in Fig. 5.10.

while the others were fixed. In order to extract valid information from the data, one has to slice the data using an appropriate line shape cut. The results show that for all W and Q^2, the cross section varies only slightly despite the large variation of $\theta_{\gamma K}^{CM}$ (Tables 5.3, 5.4, and 5.5). As expected, there are kinematic dependences in the cross sections and in the mean values, but there is agreement between the cross sections in the overlapping regions. Also, in Fig. 5.8, one can notice the difference induced by the two different kinematic coverages for $Q^2 = 0.38$ and $0.5\ \mathrm{GeV}^2$, see Fig. 5.2. The extracted W dependence of the cross section is shown in Fig. 5.7. The t and W dependences obtained become the starting functions for the parameter iteration procedure which is discussed in the next section.

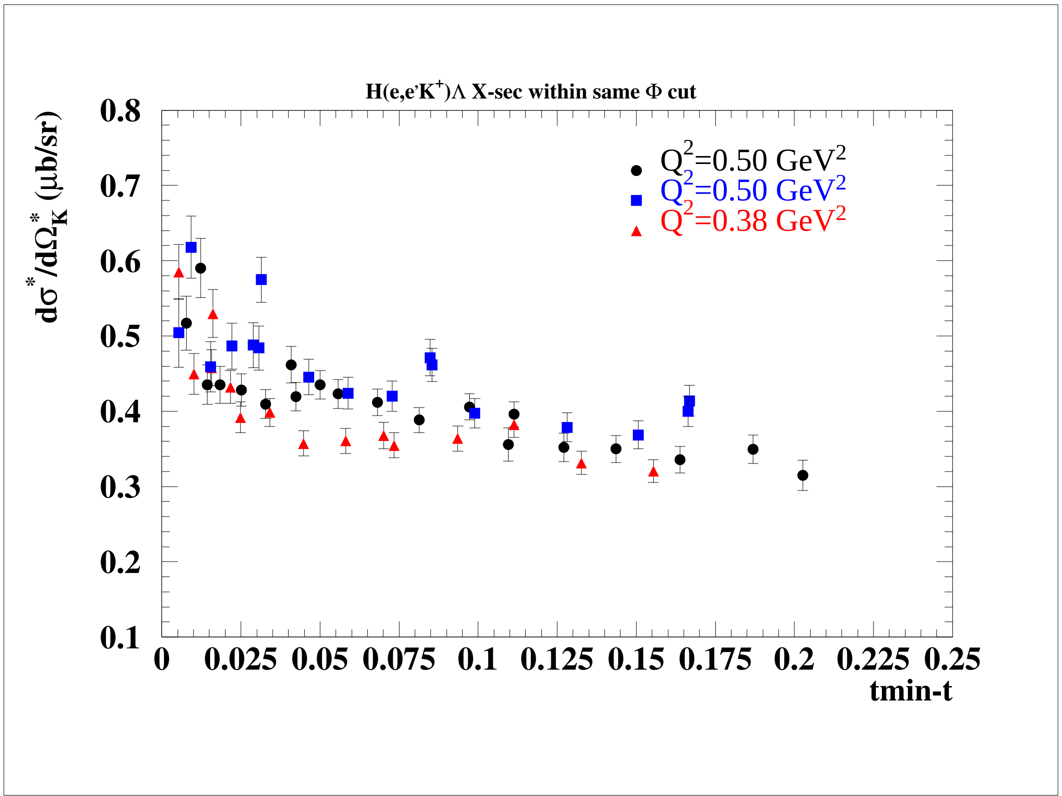

Figure 5.8: $H(e,e'K^+)\Lambda$ cross section angular dependence without scaling. All points have a common ϕ range, $|\phi - 180°| \leq 24°$. The circle and square symbols indicate the $P_{SOS} = 1.077$ and 0.929 GeV/c at $Q^2 = 0.5\ \mathrm{GeV}^2$ settings, respectively, and the triangle the $Q^2 = 0.38\ \mathrm{GeV}^2$ setting. Kinematic values for all points are indicated in Table 5.3, 5.4, and 5.5.

5.2.3 The $H(e, e'K^+)\Lambda$ Differential Cross Section

In the previous sections, the t and W dependences of the cross section, shown in Fig. 5.8 and 5.7, were obtained from the experimental data. In this section, we will describe the extraction of the parameters for each individual function in Eq. 5.1. Since the cross section varies across the different bins within our spectrometer acceptance, scaling of the cross section is needed on a point-to-point basis.

Setting	ϵ	Q^2 (GeV^2)	W (GeV)	t (GeV^2)	θ_{cm} degrees	$d\sigma/d\Omega^*$ ($\mu b/sr$)
1	0.796	0.500	1.799	-0.252	10.70	0.428 ± 0.022
2	0.797	0.502	1.796	-0.271	16.03	0.443 ± 0.023
3	0.796	0.502	1.797	-0.316	26.96	0.424 ± 0.022
4	0.794	0.498	1.803	-0.387	39.00	0.347 ± 0.018
5	0.811	0.524	1.759	-0.289	12.31	0.424 ± 0.022
6	0.811	0.523	1.759	-0.296	15.13	0.487 ± 0.020
7	0.808	0.520	1.765	-0.331	26.09	0.469 ± 0.018
8	0.804	0.513	1.778	-0.396	38.77	0.399 ± 0.022
9	0.768	0.376	1.896	-0.165	9.70	0.433 ± 0.022
10	0.768	0.379	1.892	-0.195	17.45	0.394 ± 0.020
11	0.769	0.382	1.891	-0.267	29.89	0.355 ± 0.018

Table 5.6: Cross sections at central kinematics for Λ production on hydrogen. All kinematic values are the mean values of distributions. The azimuthal angle, ϕ, distribution for each setting is shown in Appendix A.

For the iterative procedure to determine function of the kinematic variables (Eq. 5.1), we used functions displayed below in Eqs. 5.2, 5.3, 5.4, and 5.5. The results obtained are shown in Figs. 5.10, 5.11 and Table 5.7.

$$f(Q^2) = Constant \tag{5.2}$$

$$g(W) = \frac{P_1 P_k^{CM}}{(W^2 - M_p^2)W} + \frac{P_2 W^2}{(P_3 W)^2 + (W^2 - P_4^2)^2} \tag{5.3}$$

$$h(t_{min} - t) = P_1 e^{P_2(t_{min}-t)} \tag{5.4}$$

$$i(\phi) = P_1 + P_2 \cos(\phi) + P_3 \cos(2\phi) \tag{5.5}$$

where the P_i are constants whose values are determined by fitting the data.

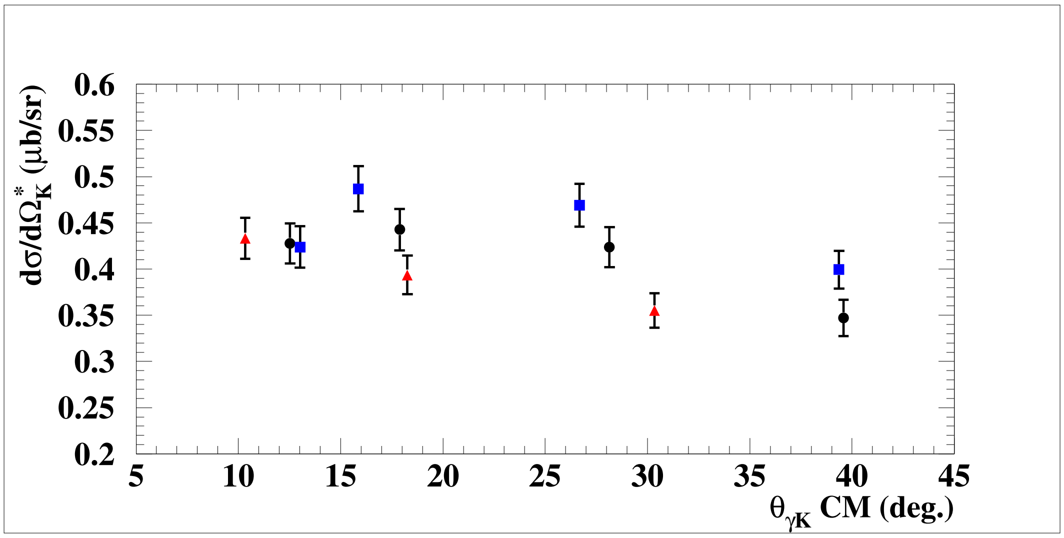

Figure 5.9: Angular dependence of $H(e, e'K^+)\Lambda$ cross section. The circle and square symbols indicate the $Q^2 = 0.5$ GeV^2 settings with $P_{SOS} = 1.077$ and 0.929 GeV/c, respectively, and the triangles the $Q^2 = 0.38$ GeV^2 setting.

The t and ϕ dependences extracted have the same form as those used previously [13] [47]. For the W dependence, the first and second terms correspond to a phase-space factor and a Breit-Wigner resonance shape, respectively. Previous

Functions	P_1	P_2	P_3	P_4
$f(Q^2)$	0.430 ± 0.005			
$g(W)$	4.470 ± 0.005	0.00089 ± 0.00086	$0.0787 \pm .02458$	1.72 (fixed)
$h(t_{min} - t)$	0.4262 ± 0.0056	-2.144 ± 0.211		
$i(\phi)$	0.438 ± 0.006	$-0.048 \pm .009$	0.008 ± 0.009	

Table 5.7: The parameter values after fit.

measurements [12] taken at a higher W, ~ 2.0 GeV, require only the phase-space factor in Eq. 5.3 which result in a decrease of the cross section seen in Fig. 5.10 near $W \sim 1.7$ GeV. This effect is responsible for the disagreement between data and simulations which include only this term. Introducing the two lowest lying nucleon resonances [39] with reported Λ-K^+ decay branching ratios, N(1710) and N(1720), leads to better agreement between the two distributions. Even though the data are not enough to distinguish differences between the two resonance contributions, the fit (the dotted curve in Fig. 5.10) describes the data well.

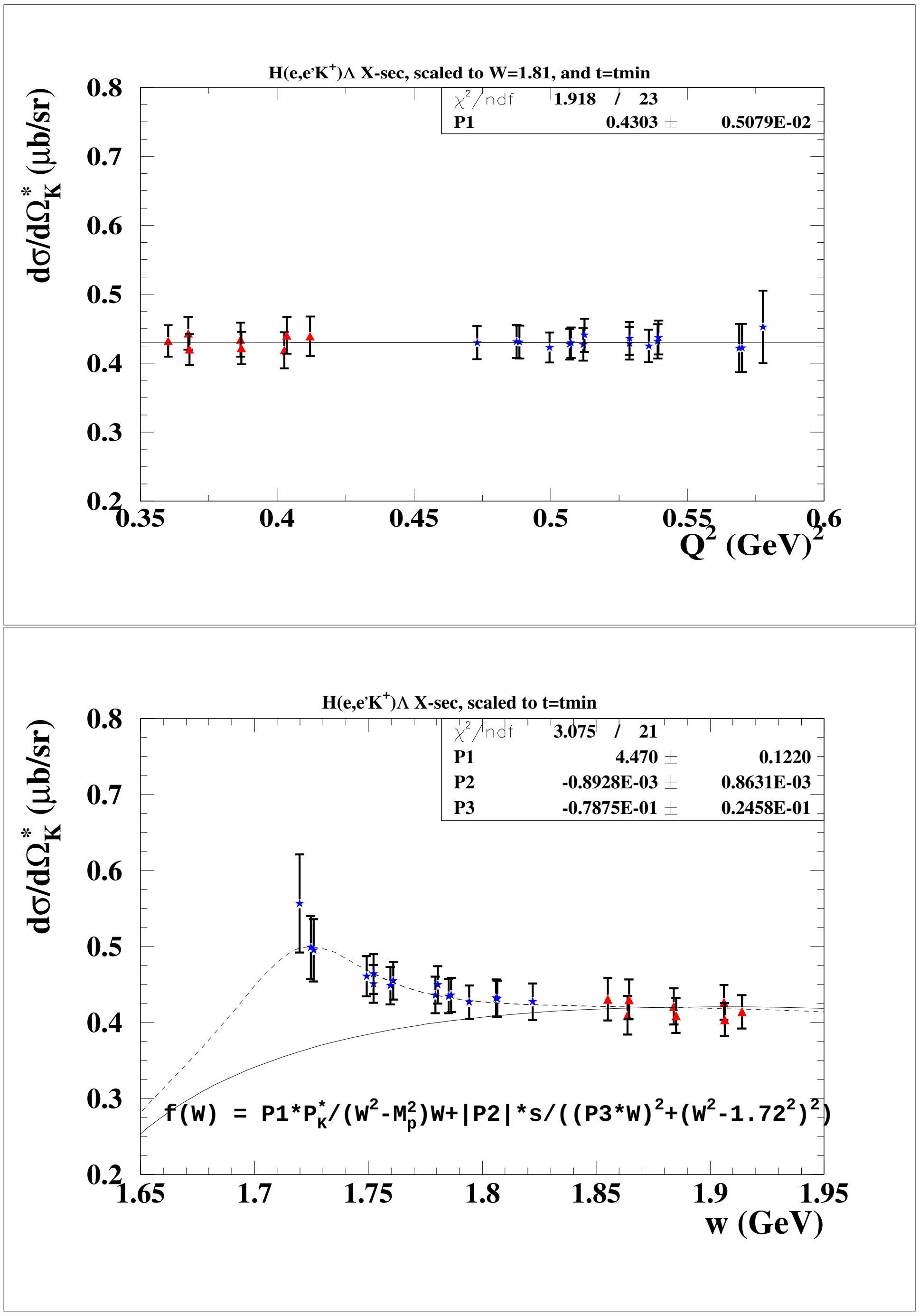

Figure 5.10: Q^2 (top) and W (bottom) dependences of the $H(e, e'K^+)\Lambda$ cross section. In the top, data have been scaled to $t = tmin$, $\phi = 90°$, and $W = 1.81$ GeV. In the bottom, data have been scaled to t=tmin and $\phi = 90°$. The dotted line is from the fitted function shown in the figure. The solid line is the phase space function fit to the data above $W = 1.81$ GeV.

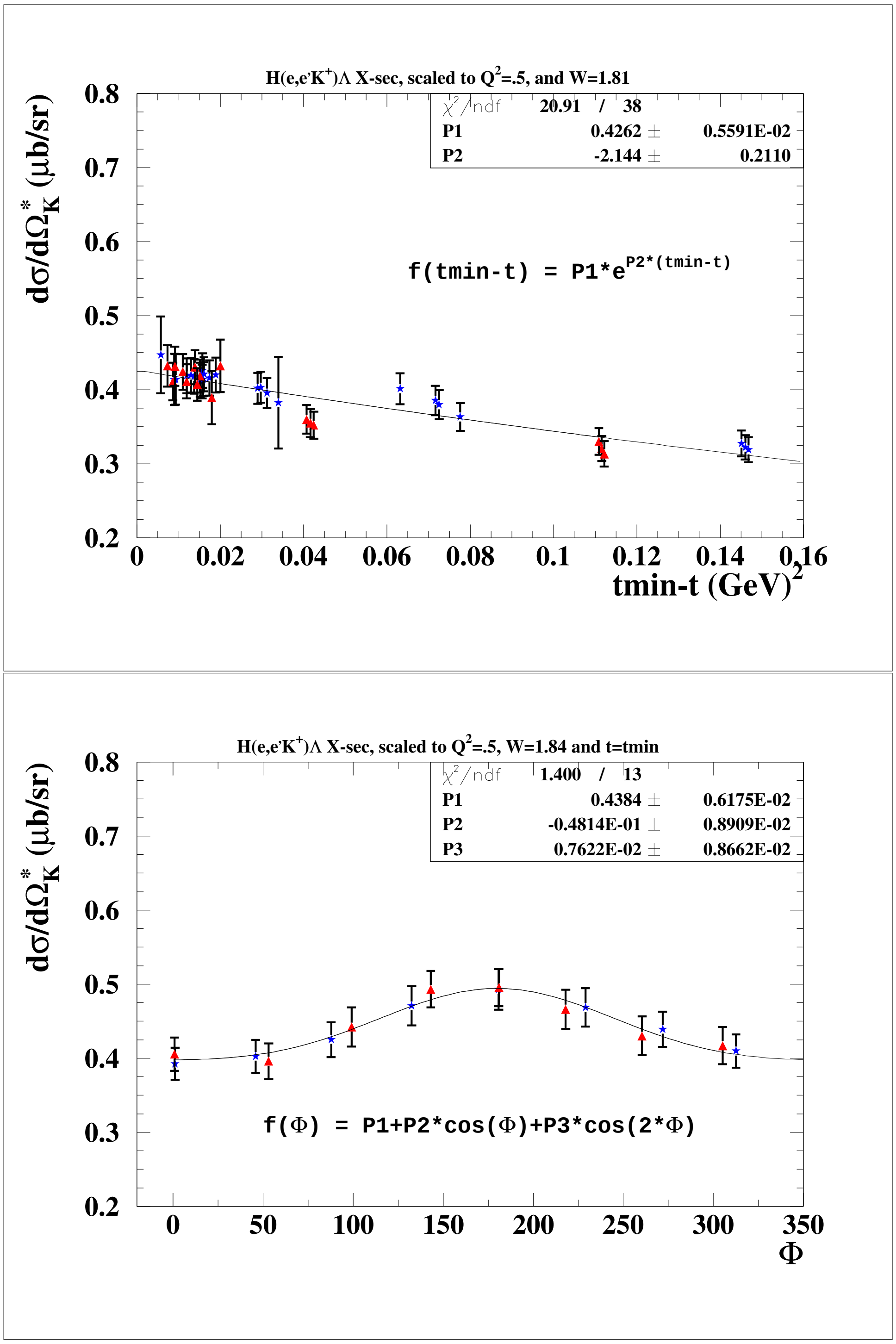

Figure 5.11: t (top) and ϕ (bottom) dependences of the $H(e,e'K^+)\Lambda$ cross section. In the top, data have been scaled to $W = 1.81$ GeV and $\phi = 90°$. In the bottom, data have been scaled to t=tmin and $W = 1.81$ GeV.

5.2.4 Σ^0 Cross Section

The Σ^0 data yields are approximately 1/4 of the Λ yields not only because of the smaller cross sections but also because of a smaller phase space. The Σ^0 production could not be studied with detailed binning data because of low statistics. The Monte Carlo simulation for Σ^0 production with initial cross sections derived from a flat matrix amplitude multiplied by phase space factor, p_K/p_γ where p_K and p_γ are the three momenta of a kaon and virtual photon, respectively, described the data reasonably well as is seen in Fig. 5.12. Table 5.8 lists the mean cross sections and kinematic variables at all settings; the angular dependences are shown in Fig. 5.12.

Setting	ϵ	Q^2 (GeV^2)	W (GeV)	t (GeV^2)	θ_{cm} degree	$d\sigma/d\Omega^*$ (μb/sr)
1	0.781	0.473	1.844	-0.302	12.554	0.107 ± 0.007
2	0.781	0.473	1.844	-0.327	20.787	0.101 ± 0.006
3	0.779	0.470	1.849	-0.380	32.487	0.106 ± 0.006
4	0.776	0.465	1.859	-0.461	44.849	0.127 ± 0.009
5	0.789	0.487	1.816	-0.335	13.976	0.080 ± 0.005
6	0.789	0.486	1.819	-0.352	21.213	0.082 ± 0.005
7	0.787	0.481	1.827	-0.396	32.688	0.101 ± 0.006
8	0.784	0.478	1.835	-0.471	45.105	0.094 ± 0.006
9	0.762	0.365	1.914	-0.219	11.568	0.133 ± 0.007
10	0.761	0.364	1.917	-0.251	20.691	0.132 ± 0.007
11	0.758	0.365	1.921	-0.324	33.226	0.130 ± 0.008

Table 5.8: Σ° cross sections at central kinematics for hydrogen. All kinematic values are the mean values of distributions.

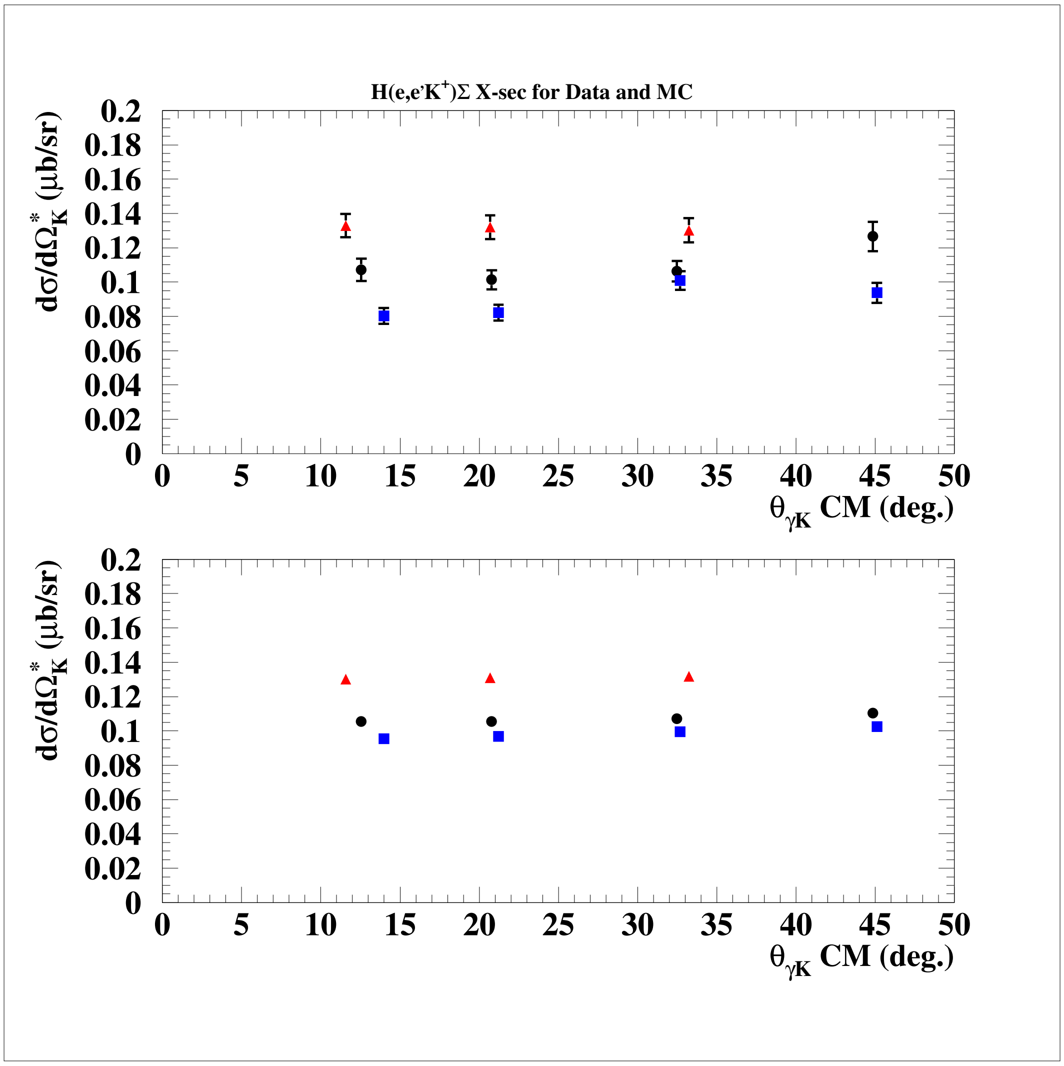

Figure 5.12: $H(e, e'K^+)\Sigma^0$ cross section; data (top) and MC simulation (bottom). The circle and square symbols indicate $P_{SOS} = 1.077$ and 0.929 GeV/c at $Q^2 = 0.5$ GeV^2, respectively, and the triangles, $Q^2 = 0.38$ GeV^2

5.3 $D(e, e'K^+)$

For the deuterium data, the Monte Carlo simulations for the possible reactions mentioned previously were generated and compared with data. The Λ cross section with the empirical kinematic dependences was inserted into the Monte Carlo simulation for the $D(e, e'K^+)\Lambda n$ reaction. In the MC simulations with two Sigma production cross sections for deuterium, Σ^0 and Σ^-, the model cross section for Σ^0 is scaled to $H(e, e'K^+)\Lambda, \Sigma^0$ data. To understand Σ^- production from neutron contributions to the deuterium data, we assumed that the ratio of Λ to Σ^0 production on the deuteron is the same as on the free proton.

5.3.1 Missing Mass Spectra

To extract the cross section for the three hyperons (Λ, Σ^0, and Σ^-) from D data, the missing mass spectra of data were fitted with the missing mass histograms produced by the three simulations for Λ, Σ^0 and Σ^-. During this fitting, a maximum likelihood fit [48] was used with the constraint which kept the Λ and Σ^0 cross section ratio for deuterium, $\sigma_\Lambda/\sigma_{\Sigma^0}$, the same as in hydrogen. With the quasi-free model, the fit determined the scaling factors for the Λ and Σ^- distributions over the missing mass range 2.080-2.130 and 2.165-2.320 GeV, respectively. In the missing mass spectra, offsets $\lesssim$ 1 MeV were applied for each kinematic setting. These offsets are determined by minimizing χ^2 during variation of offsets between -3 to 1 MeV in 0.5 MeV steps.

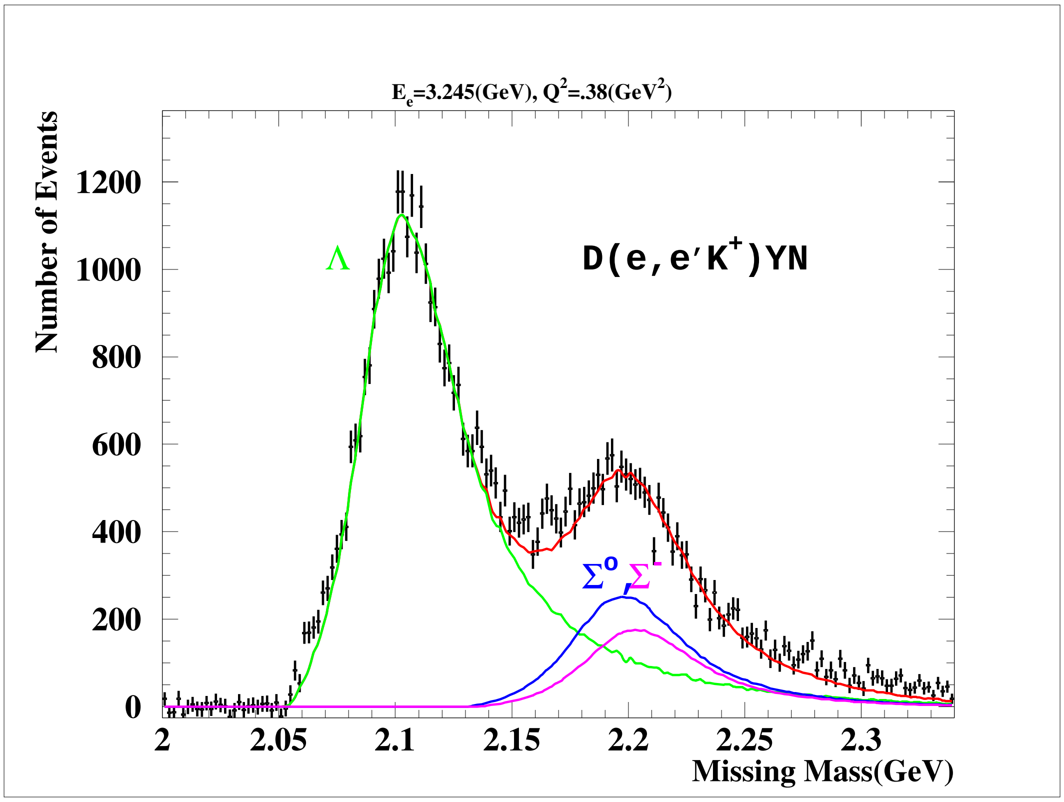

Figure 5.13: The missing mass spectra from data (points with error bars) and MC simulations (solid lines) for $D(e, e'K^+)YN$ reactions. The sum of the three simulations is the line through the data.

The results of fitting are shown in Fig. 5.13 where, in general, there is good agreement between the sum curve and the data. It is evident, however, that near the Λ threshold, there is a clear excess in the cross section that is presumed to result from final state interactions (FSI) between the Λ and neutron to be discussed in the next section.

5.3.2 Final State Interaction

Near threshold for the $D(e,e'K^+)\Lambda n$ reaction, the emergent Λ-n relative energy is very low and the interaction between them is strong. In the following, a simple model for the FSI is presented. We treat the problem in a manner analogous to nucleon-nucleon scattering, but adjust the parameters to be suitable for Λ-n interaction [8].

Formalism

The matrix element for the reaction $\gamma^* + d \to K^+ + \Lambda + n$,

$$M_{fi} = < K\Lambda n|\mathbf{T}|\gamma^* d >, \tag{5.6}$$

with $\mathbf{T}$ being an appropriate operator [8]. Without any interaction between the outgoing particles, the final state, $< K\Lambda n|$, is simply described by a product of three plane waves. Due to the Λ-n interaction, Eq. 5.6 becomes

$$\tilde{M}_{fi} = < \Lambda n| \int |\Lambda' n' >< \Lambda' n'| < K|\mathbf{T}|\gamma^* d >, \tag{5.7}$$

where $\tilde{M}_{fi}$ is the modified scattering amplitude. To simplify substituting the FSI into Eq. 5.6, it was assumed that the amplitude $< \Lambda n|\Lambda' n' >$ is calculated as an elastic Λ-n scattering wave function. The scattering amplitude with FSI is

$$\tilde{M}_{fi} = \frac{\psi(kr+\delta)}{\psi(kr)} M_{fi}, \tag{5.8}$$

where $\psi(kr+\delta)$ and δ are the wave function and phase-shift after Λ-n interaction, and ψ is without the interaction. Therefore, the cross section with FSI is

$$(\frac{d\sigma}{d\Omega})_{FSI} = f_{P.S.}|\tilde{M}_{fi}|^2 = f_{P.S.}|\frac{\psi(kr+\delta)}{\psi(kr)}|^2|M_{fi}|^2, \tag{5.9}$$

where $f_{P.S.}$ is a phase space factor. The influence, I, of the interaction between Λ and n on the reaction D(e,e′ K$^+$)Λn is

$$I = |\frac{\psi^*(kr+\delta)}{\psi(kr)}|^2, \tag{5.10}$$

where I is the ratio of cross sections with and without FSI.

The Λ-n final-state-interaction is predicted by theoretical calculations [8], and [49]. The three different models for the Λ-n interaction were parameterized with two Gaussian potentials, one attractive (V_A) and one repulsive (V_R), so that

$$V(r) = V_A e^{r^2/\beta_A{}^2} + V_R e^{r^2/\beta_R{}^2}. \tag{5.11}$$

The values of the parameters for the three models are listed in Table 5.9. The scattering length and effective range are obtained by applying Bethe's formula [8]

Model	state	V_A (MeV)	β_A (fm)	a (fm)	r (fm)
Verma	Singlet ($^1S_0$)	-167.34	1.100	-2.29	3.15
	Triplet ($^3S_1$)	-132.42	1.100	-1.77	3.25
Jülich A	Singlet ($^1S_0$)	-373.94	0.790	-1.60	1.33
	Triplet ($^3S_1$)	-144.14	1.059	-1.60	3.15
Jülich B	Singlet ($^1S_0$)	-131.49	1.095	-0.57	7.65
	Triplet ($^3S_1$)	-189.60	0.964	-1.94	2.42

Table 5.9: The parameters for the various potentials used in Eq. 5.11. The strength and range of the repulsive part are fixed for all three potentials at $V_R = 246.80$ MeV, $\beta_R = 0.82$ fm for the singlet state, and $V_R = 181.68$ MeV, $\beta_R = 0.82$ fm for the triplet state. From [8].

for low-energy scattering,

$$k \cot \delta = 1/a + rk^2/2, \tag{5.12}$$

where k is the relative momentum between Λ and neutron, δ is the s-wave phase shift, a is the scattering length and r is the effective range. To describe the data near threshold for production of each hyperon, the phase shift is calculated up to p-wave. The calculated phase shifts were applied to modify the cross section for quasi-free Λ production on the proton by using Eq. 5.9. For the Σ^0-n and Σ^--p FSI, the same model used in Λ-n FSI was applied, but scaled to fit the data at the threshold of Σ by adjusting a parameter, r, which will be discussed in the following section. Since the interactions of K^+-N are weak relative to N-N scattering, FSI of K^+-N are ignored.

FSI models and phase-shift calculations

The Y-N FSI is treated as the elastic scattering of Y-N. The Lippmann-Schwinger equation including the potentials, Eq. 5.11, with the parameters in Table 5.9 has been solved numerically to extract the phase-shift. The detailed description of the calculation and the numerical method of the phase-shift are presented in Appendix C. The numerical calculation code was written in FORTRAN. The FORTRAN code initially was used for p-p scattering calculations [50] using the Yukawa potential. It was modified for Y-N using two Gaussian potentials. The results from this work were compared with the calculated phase shift using Eq. 5.12 for each model mentioned in Table 5.9.

In two body elastic scattering, the differential cross section is

$$\frac{d\sigma}{d\Omega} = |f(\theta)|^2, \tag{5.13}$$

where $f(\theta)$ is a scattering amplitude. The scattering amplitude can be written as

$$f(\theta) = \frac{1}{k}\sum_{l=0}^{\infty}(2l+1)e^{i\delta_l}\sin\delta_l P_l(\cos\theta). \tag{5.14}$$

To solve this scattering problem, the Lippmann-Schwinger equation, Eq. C.6, was solved numerically. The relation between scattering amplitude and transition matrix, $\mathbf{T}$, is

$$f(\theta) = -(2\pi)^2 k \frac{\rho(E_k)}{k} T(k, \hat{k'} \cdot \hat{k}),$$

where $\rho(E_k) = dk/dE$. After expanding in partial waves, the $\mathbf{T}$ matrix becomes

$$\mathbf{T}(k, \hat{k}' \cdot \hat{k}) = -\frac{1}{\pi\rho(E_k)} \sum_{l=0}^{\infty} \frac{(2l+1)}{4\pi} e^{i\delta_l} \sin\delta_l P_l(\cos\theta). \tag{5.15}$$

The matrix element of $\mathbf{T}$ is

$$\mathbf{T}_l(k) = -\frac{e^{i\delta_l}\sin\delta_l}{\pi\rho(E_k)}. \tag{5.16}$$

Using Eq. C.12 and substituting Eq. 5.16, the matrix element of R can rewritten as

$$\begin{aligned} \mathbf{R}_l(k) &= \frac{\mathbf{T}_l}{1 - i\pi\rho(E_k)\mathbf{T}_l} \\ &= -\frac{1}{1 - i\pi\rho(E_k)e^{i\delta_l}\sin\delta_l/\pi\rho(E_k)} \frac{e^{i\delta_l}\sin\delta_l}{\pi\rho(E_k)} \\ &= \frac{-\sin\delta_l}{\pi\rho(E_k)(e^{-i\delta_l} + i\sin\delta_l)} \end{aligned}$$

Therefore, the numerical solution of Eq. C.16, $\mathbf{R}_l(k)$, can be written as

$$\mathbf{R}_l(k) = -\frac{\tan\delta_l}{\pi\rho(E_k)}. \tag{5.17}$$

To get the solution for Eq. 5.17 numerically, the function was transformed by Gaussian quadrature. For a given $f(y)$,

$$\int_{-1}^{+1} f(y)dy \simeq \sum_{i=1}^{N} f(y_i)w_i \tag{5.18}$$

where y_i are the zeros of $P_N(y)$ distributed between -1 and +1, and w_i are the weights. Also to take care of the $\mathbb{P}$ singularity in Eq. C.16, the integral was split into two parts;

$$\int_0^\infty \to \int_0^{2k} + \int_{2k}^\infty . \tag{5.19}$$

The singularity is the middle of the range between zero and ∞, i.e. $2k$. The phase-shift results from the present calculation for S-waves were compared with results of Li and Wright [8] and, as shown in Table 5.10, are consistent with each other.

The calculated FSI influence factors for all three models are shown in Fig. 5.14. For the ${}^3S_1$ of each model, the influence factor was determined by weighting the four possible states equally.

Model	$P_{\Lambda,n}$ (MeV/c)	Phase Shift (rad.) Li & Wright	Calculation (N.R)	Relativistic
Verma	10.0	.11448	.11656	.11667
	20.0	.22018	.22035	.22262
	30.0	.31094	.31112	.31429
	40.0	.38420	.38399	.38789
	50.0	.44030	.43910	.44357
	60.0	.48123	.47819	.48315
	70.0	.50953	.50366	.50902
	80.0	.52773	.51790	.52361
	100.0	.54223	.52093	.52725
	120.0	.53799	.50058	.50741
	140.0	.52338	.46577	.47302
Jülich A.	10.0	.08069	.08084	.08411
	20.0	.15906	.15907	.16546
	30.0	.23310	.23309	.24233
	40.0	.30129	.30124	.31301
	50.0	.36270	.36257	.37654
	60.0	.41696	.41669	.43253
	70.0	.46410	.46362	.48104
	80.0	.50446	.50368	.52246
	100.0	.56705	.56531	.58631
	120.0	.60955	.60631	.62912
	140.0	.63658	.63124	.65564
Jülich B.	10.0	.02872	.02951	.03050
	20.0	.05645	.05728	.05948
	30.0	.08231	.08598	.08664
	40.0	.10565	.10854	.11088
	50.0	.12602	.12950	.13160
	60.0	.14325	.14601	.14841
	70.0	.15736	.16004	.16115
	80.0	.16851	.16874	.16980
	100.0	.18310	.17445	.17555
	120.0	.18960	.16700	.16777
	140.0	.19060	.14875	.14920

Table 5.10: The phase shift calculation results for different models.

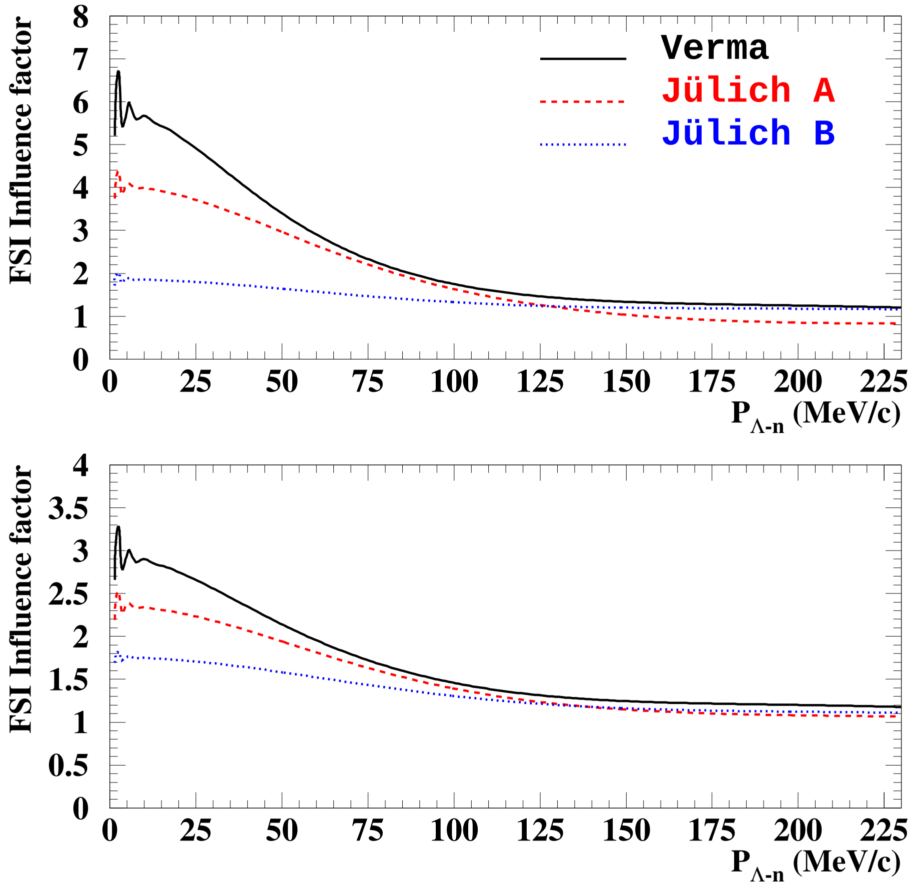

Figure 5.14: Λ-n FSI influence factors for three different models. The top figure is for singlet ($^1S_0$) potentials only. The bottom figure includes triplet contributions where the influence factor, $I = (I_s + 3I_t)/4$ and indices s and t indicate singlet and triplet, respectively.

5.3.3 Spectra with FSI

After the influence factor, Eq. 5.10, was calculated, it was applied to modify the cross section for p(e,e$'K^+$)Y in the MC simulation. The results of Monte Carlo simulations with and without FSI are shown in Figs. 5.15 and 5.16. Inclusion of FSI effects results in differences in Λ production cross sections $\lesssim 4.$ %.

The three different models for Λ-n FSI are compared with data in Fig. 5.17. The influence (or contribution) factor extracted from the data by taking the ratio of yield for data to MC simulation (quasi-free model only) for each bin is shown in Fig. 5.18. The magnitude of the influence factor at $\sim$ 50 MeV/c relative Λ-n momentum is in better agreement with the pure ${}^1S_0$ term than with $\frac{{}^1S_0+3\cdot{}^3S_1}{4}$ contributions; the shapes are similar. Near the Λ threshold, the $^1\mathrm{S}_0$ of Verma and Jülich A models represent the data well but Jülich B does not.

Since the quasi-free Λ-n cross section just above threshold is very small, it is not possible to observe statistically significant FSI effects for relative momenta $\ll$ 50 MeV/c or energy $\lesssim$ 10 MeVabove threshold. Moreover, in the data shown in Fig. 5.18, the observable difference resulting from FSI at an excitation of $\sim$ 10 MeV, i.e. $\sim$ 50 MeV/c relative momentum, corresponds to the maximum of the influence factor. Since the primary difference between the Verma and Jülich A models occurs for $P_{\Lambda-n} \leq$ 50 MeV/c in the center-of-mass system as seen in Fig 5.14, the data were not able to distinguish significant differences between the Verma and Jülich A models. They do, however, show obvious differences with the Jülich model B, which, because of it relative weakness, is hard to distinguish from the purely quasi-free calculation.

In Verma and Jülich model A, the singlet interaction fitted data better than inclusion of the triplet contribution. The proton and neutron are spin 1/2 baryons. The deuteron is characterized by a $J^P = 1^+$ ground-state which is loosely bound ($E_B \approx 2.2$ MeV), where the proton and neutron move mainly in a relative $^3S_1$ state. The K^+ and Λ spins are 0 and 1/2, respectively. In the cartoon of Fig. 5.19, we assume the two u quarks in the initial proton are located far from each other because of Coulomb repulsion. After the reaction, since the orbital momentum tends to be conserved, the same charge quarks, d and s, surround the u quark. As result, the magnetic moment changes to the opposite direction. Therefore, it may flip the total spin of the Λ or reduce the triplet contribution. This qualitative argument is clearly inadequate, but may serve to justify our assumptions.

For the Σ^0-n and Σ^--p FSI, Jülich model A was used and scaled arbitrarily to fit the data. The influence factors for the two Σ-N FSI have been equally weighted. As shown in Fig. 5.20, the Σ-N FSI contributions are much stronger than Λ-n. Therefore, as mentioned earlier in the section 1.2.2, Σ's can interact strongly by exchanging a pion in the intermediate state. In this work, the influence factor for each Σ-N FSI is about 7 times stronger than Λ-n.

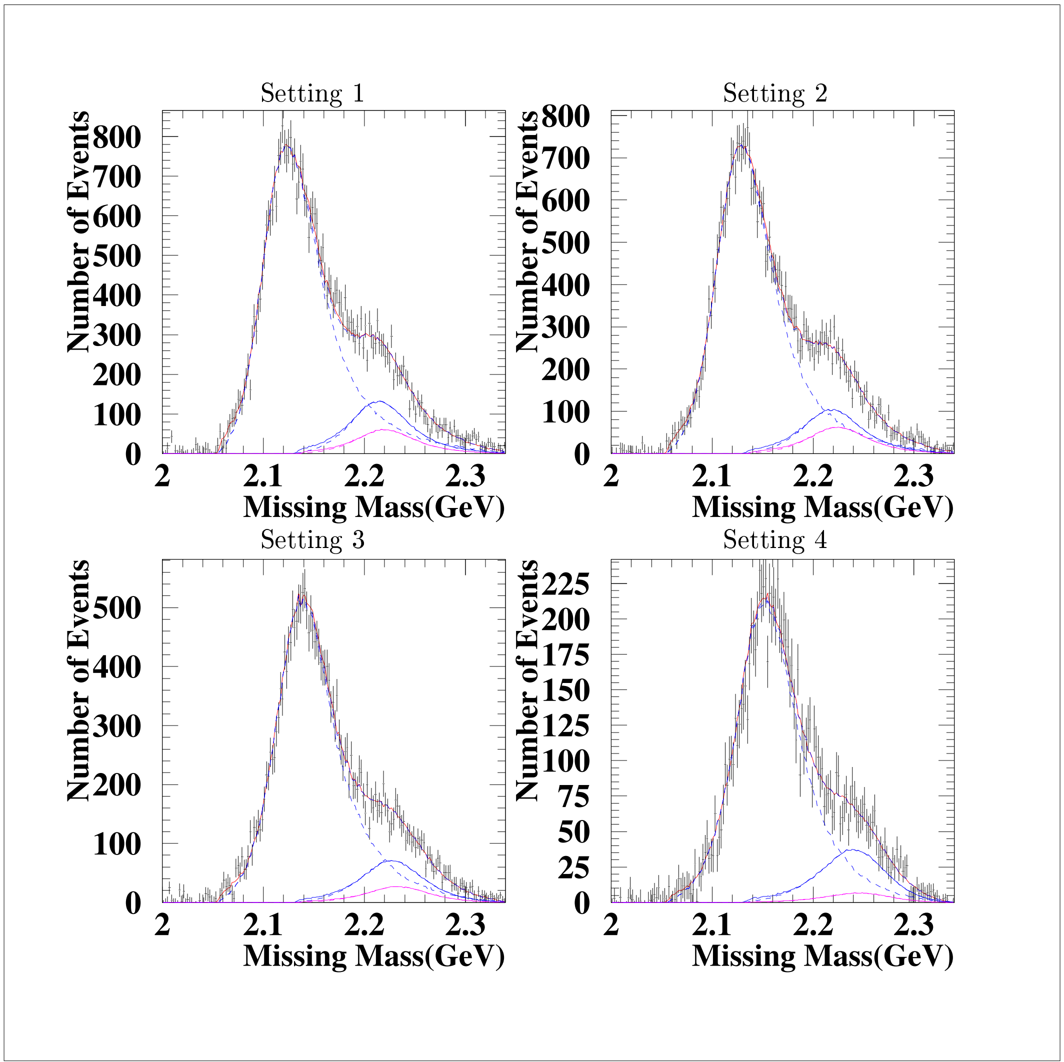

Figure 5.15: $D(e, e'K^+)YN$ missing mass spectra of data and simulations with and without FSI for set numbers 1–4 as defined in Table 2.7 at $Q^2 \approx 0.5$ GeV^2. The solid lines are Y-N distributions with FSI from the $^1S_0$ of Jülich model A [8]. The dotted lines are for pure quasi-free production.

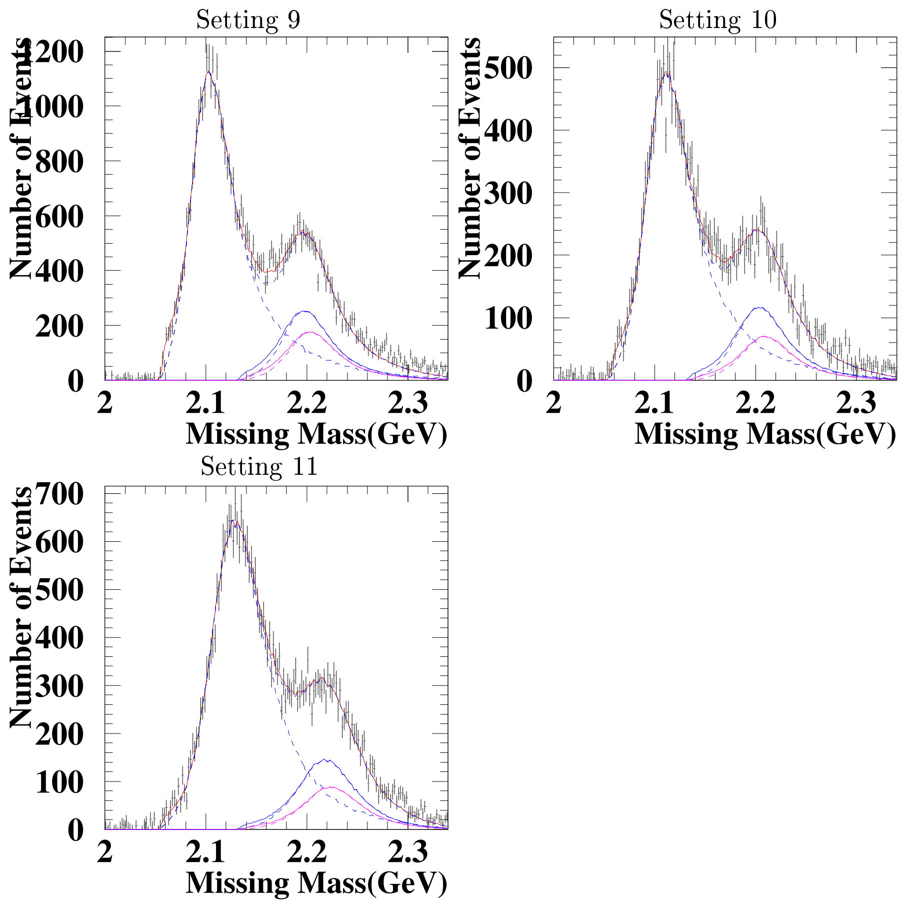

Figure 5.16: $D(e, e'K^+)YN$ missing mass spectra of data and simulation with and without FSI for set numbers 9–11 as defined in Table 2.7 at $Q^2 \approx 0.38$ GeV^2. The solid lines are the three cross sections with FSI from the $^1S_0$ of Jülich model A [8]. The dotted lines are for pure quasi-free production.

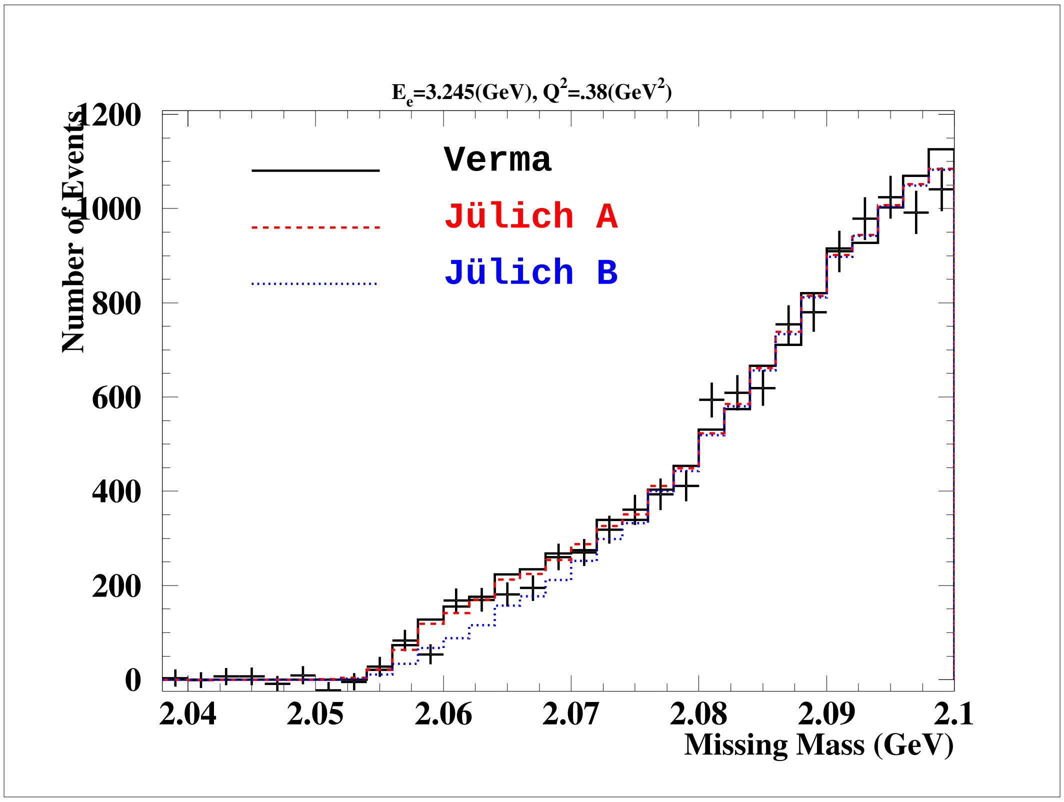

Figure 5.17: Comparison of the three different Λ-n FSI models, mentioned in Table 5.9, with data near the threshold of Λ production on deuterium. The data shown come the far forward setting at $Q^2 = 0.38$ GeV^2.

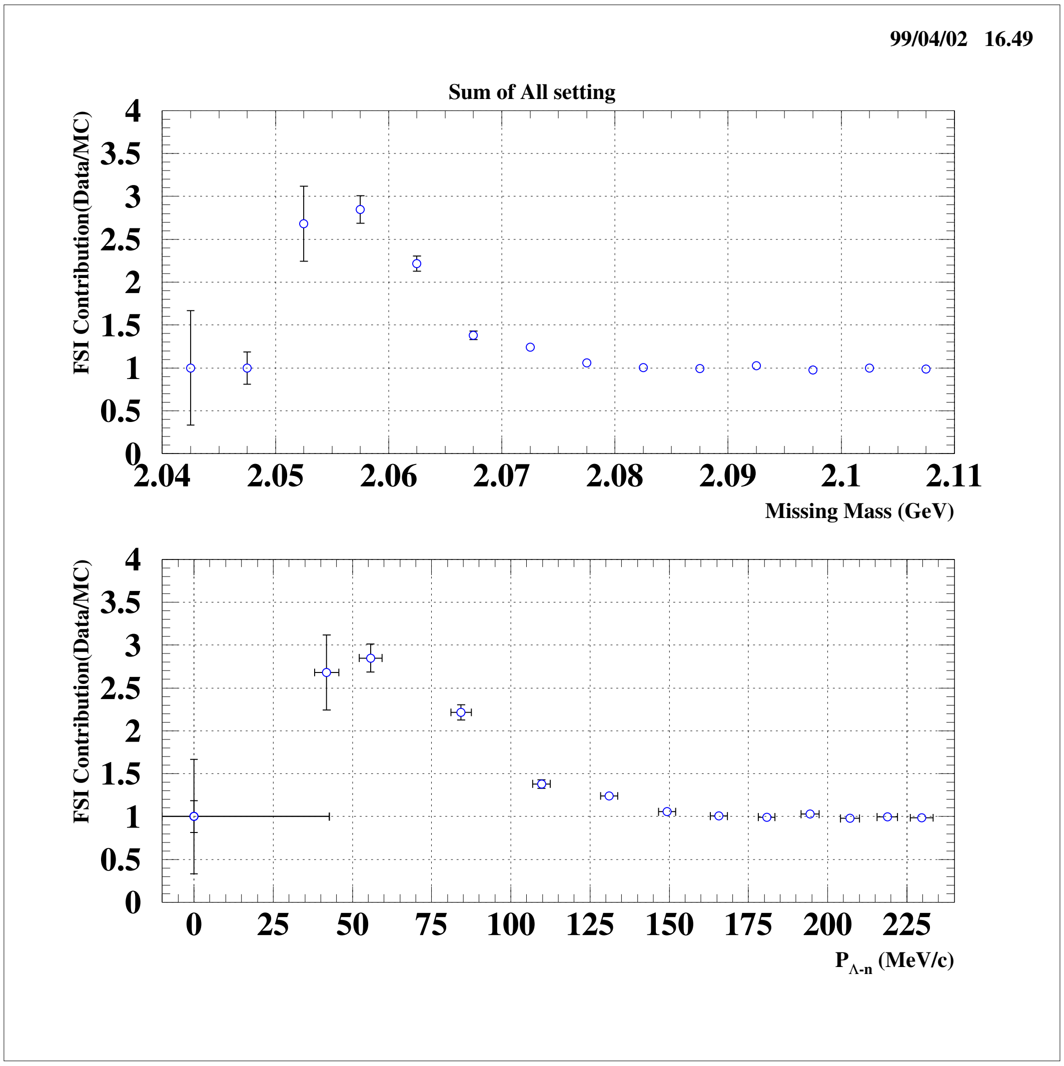

Figure 5.18: The measured Λ-n FSI influence factor from data as a function of missing mass (top) and relative Λ-n momentum (bottom)

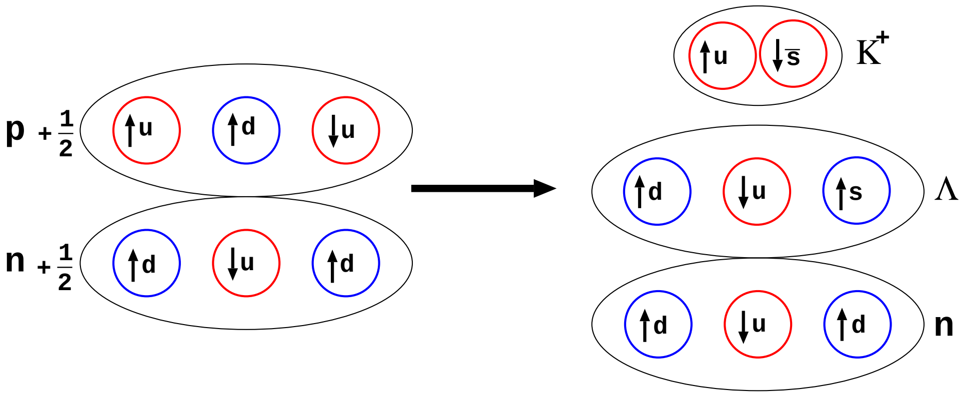

Figure 5.19: Simple spin diagram for $D(e, e'K^+)\Lambda n$ reaction.

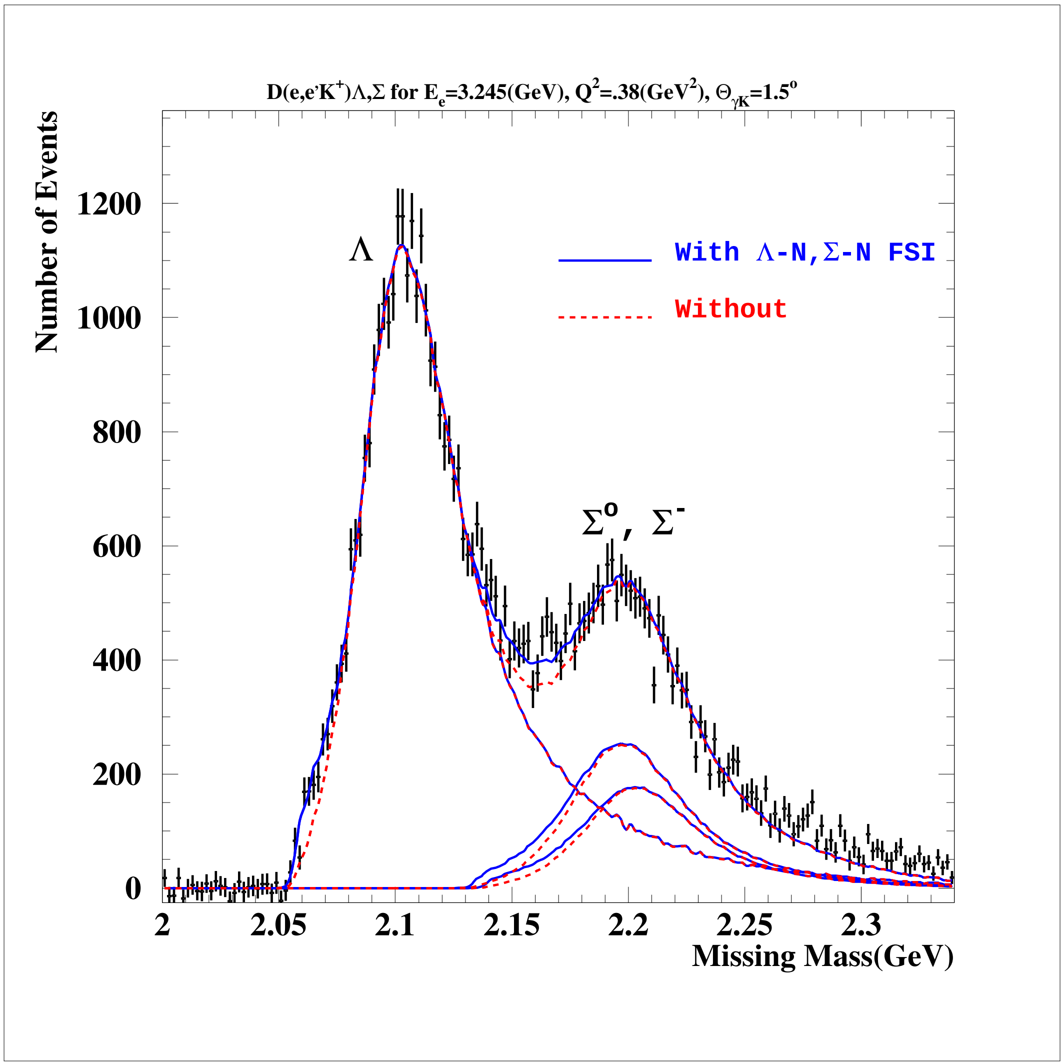

Figure 5.20: $D(e, e'K^+)YN$ missing mass plot with FSI MC simulation for $Q^2 = 0.38$ GeV^2 forward settings. The points are data and the solid (dashed) line from simulations with (without) Λ-n, Σ^0-n, and Σ^--p FSI.

5.3.4 D/H and Σ^-/Σ^0 Ratio

Kinematics		Cross sections (μb/sr) on deuterium			Σ Ratio
Q^2 (GeV^2)	$\theta_{\gamma K}$(deg.)	Λ	Σ^0	Σ^-	Σ^-/Σ^0
	0.	$.413 \pm 0.023$	$.111 \pm 0.011$	$.059 \pm 0.017$	0.53 ± 0.17
0.5	4.	$.426 \pm 0.026$	$.104 \pm 0.012$	$.073 \pm 0.021$	0.70 ± 0.22
	8.	$.406 \pm 0.030$	$.110 \pm 0.012$	$.060 \pm 0.027$	0.54 ± 0.31
	13.	$.332 \pm 0.037$	$.135 \pm 0.019$	$.067 \pm 0.111$	0.49 ± 0.70
	1.5	$.410 \pm 0.022$	$.131 \pm 0.010$	$.089 \pm 0.014$	0.68 ± 0.13
0.38	6.	$.386 \pm 0.027$	$.134 \pm 0.011$	$.076 \pm 0.022$	0.57 ± 0.17
	11.	$.341 \pm 0.022$	$.129 \pm 0.010$	$.077 \pm 0.020$	0.60 ± 0.17

Table 5.11: Cross sections for Kaon electroproduction on deuterium. The errors are mainly dominated by fitting errors, $\sim$ 4–10 % for the Λ and Σ^0, and $\sim$ 16–150 % for Σ^-. The $\theta_{\gamma K}$ is in the Lab system.

The extracted cross sections are shown in Table 5.11. The Λ cross section ratio for deuterium to hydrogen is $\sim$ 0.956, shown in Fig. 5.21. Since there are some differences in kinematic effects ($\sim$ 3.2 %) between hydrogen and deuterium that are obtained from the MC simulations, due to the 3 body final state, the corrected Λ cross section ratio for D/H becomes

$$f_D/f_H = (\sigma_D/\sigma_H)/(\sigma_{D,MC}/\sigma_{H,MC}) = (0.956 \pm 0.026)/0.968 = 0.987 \pm 0.027,$$

where f_D and f_H are scaling factors modifying the yields from MC simulations to the data, σ_D and σ_H are the Λ cross sections from data, $\sigma_{D,MC}$ and $\sigma_{H,MC}$ are from simulations, and the indices D and H indicate target.

The ratios of the cross sections, Σ^-/Σ^0 for all kinematics are listed in Ta-

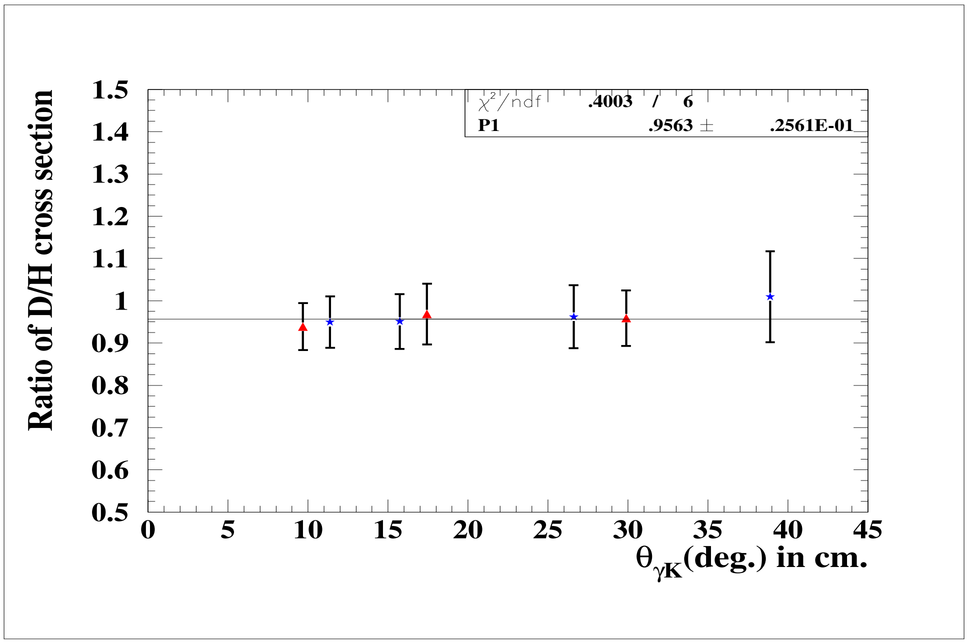

Figure 5.21: The cross section ratios between $H(e,e'K^+)\Lambda$ and $D(e,e'K^+)\Lambda$n for the settings in Table 5.11. The triangle symbols are from $Q^2 = 0.38$ data and star for $Q^2 = 0.5$ GeV^2.

ble 5.11 The average of the ratios $\sigma_{\Sigma^-}/\sigma_{\Sigma^0}$ is 0.61 ± 0.07 as shown in Fig. 5.22. Previous measurements [16] and [12] report different results. In reference [16], the Σ^-/Σ^0 ratio is $2.37 \pm 0.11 \pm 0.12$, but Bebek's value is 1.60 ± 1.40, with error ≈ 100 %. Assuming a purely isospin dependence, the ratio of the cross sections of Σ^- to Σ^0 can be calculated as

$$\frac{\sigma(\Sigma^-)}{\sigma(\Sigma^0)} = |\frac{< J_p m_p J_i m_i | J_{\Sigma^-} m_{\Sigma^-} >}{< J_n m_n J_i m_i | J_{\Sigma^0} m_{\Sigma^0} >}|^2, \tag{5.20}$$

where the brackets are Clebsch-Gordan coefficients with J_x and m_x being the isospin- and z-projections of isospin for proton, exchanged particle, and Σ. For pure

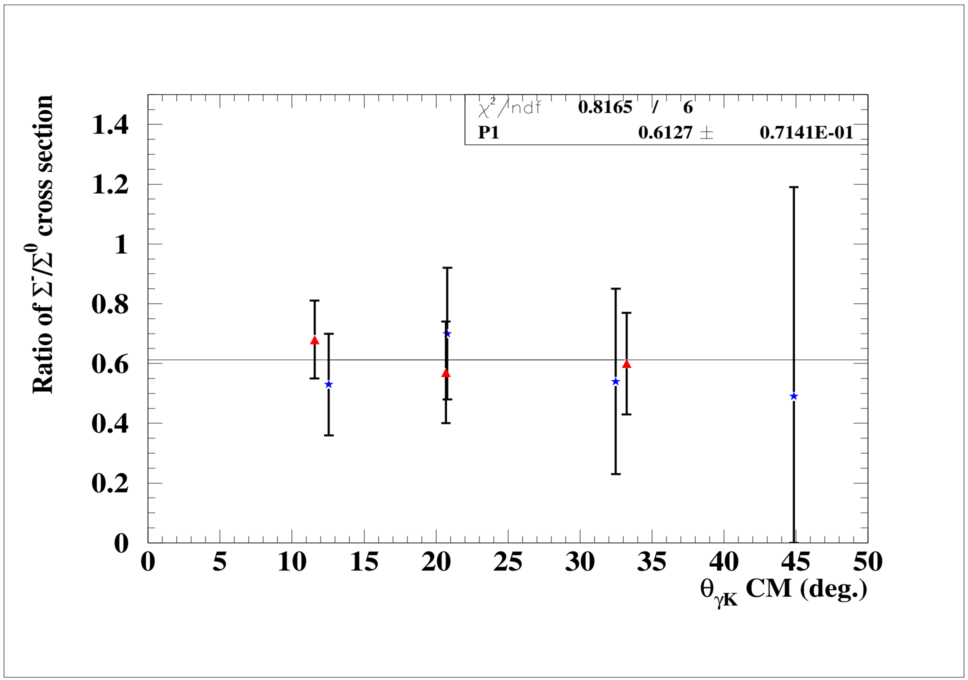

Figure 5.22: Σ^-/Σ^0 cross sections for deuterium, where the Σ^0 cross sections are obtained from the free proton. The triangle symbols are $Q^2 = 0.38$ GeV^2 data and the stars for $Q^2 = 0.5$ GeV^2.

isospin-$\frac{1}{2}$ exchange, the calculated ratio $\frac{\sigma(\Sigma^-)}{\sigma(\Sigma^0)} = 2.0$. For the isospin-$\frac{3}{2}$ exchange, however, the ratio is 0.5, consistent with the result of this work.

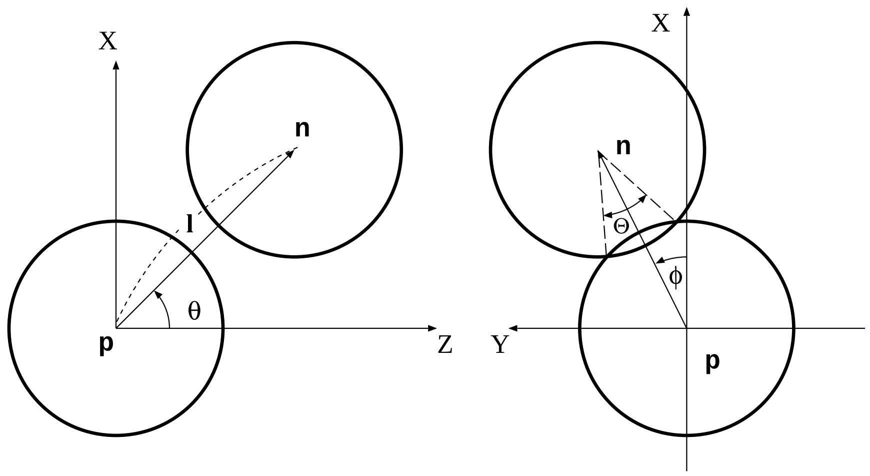

Figure 5.23: Schematic model of the deuteron. Left side is the cross section projected in the X-Z plane, right side is in the X-Y plane. The overlap region of the two circles in the right side picture is the area of shadow from neutron blocking. The electron or virtual photon flux is assumed to be coming in the $-$Z direction.

5.3.5 Shadowing Effect

Because of random motions of the two nucleons, proton and neutron, in the deuteron, the incoming electron can be effectively blocked from hitting the proton by the neutron. The probability of this shadowing effect may simulated with random rotational motion of a simple dumbbell model. In this model, crudely illustrated in Fig. 5.23, the distance between a proton and a neutron in the deuteron is taken to be the average value, l=2.5 fm [51]. The radii, r_n, of the two nucleons is set to 0.8 fm [52].

In a simple Monte Carlo simulation for extreme neutron shadowing, events were generated uniformly over the cross section area of proton, $x^2+y^2 \leq r_n^2$ where x, y are positions in X-Y plane and $r_n = 0.8$ fm. The center of the neutron was selected by generating $\cos\theta$ and ϕ randomly. If $\cos\theta > 0.$ and $(x_n - x)^2 + (y_n - y)^2 \leq r_n^2$, where $x_n = l\sin\theta\cos\phi$ and $y_n = l\sin\theta\sin\phi$ are projections of the neutron center in X-Y plane, then the events were defined as blocked by the neutron. The result of this simulation is that the shadowing by the neutron is ~ 2.7 %, which is roughly consistent with the value measured from data, indicated in Section 5.3.4.

Another scenario involves consideration of K^+-N in the final state [16] and [53]. The K^+-N total cross section is ~ 20 mb compared to an area ~ 600 mb for the deuteron. This simplistic assumption leads to ~ 97 % transmission of the K^+, also consistent with our data.

5.4 Discussion of Results

5.4.1 Proton

To compare our data with previous results, the measured Λ cross sections for the far-forward settings at two different Q^2, 0.38 and 0.50 GeV^2, have been scaled to the kinematics of $W = 2.1$ GeV. The results are shown in Fig. 5.24. Our two Q^2 points do not follow the dipole curve which fit previous data, but extrapolates to the photo-production point [55], $Q^2 = 0$. The results from electro-production must agree with photo-production or converge to photo-production as $Q^2 \to 0$, if the cross section form (Eq. 1.9) of electroproduction is valid.

In the center-of-momentum frame, the cross section formula for kaon [3] electroproduction,

$$\frac{d\sigma}{d\Omega_{c.m.}} = \frac{\vec{P_K}}{\vec{P_\gamma}} \frac{M_p M_Y}{16\pi^2 s} < |T_{fi}|^2 > \tag{5.21}$$

where $\vec{P_K}$ and $\vec{P_\gamma}$ are the three momenta of the kaon and virtual photon in the c.m., M_p and M_Y are the mass of kaon and Λ and $< |T_{fi}| >$ is defined to be the virtual photon-production square averaged amplitude, as mentioned in Eq. 1.8,

$$\begin{aligned} < |T_{fi}|^2 > \;=\; & \sum_{\lambda,\lambda'} [\frac{1}{2}(|H_x|^2 + |H_y|^2) + \varepsilon_L |H_z|^2 + \frac{\varepsilon}{2}(|H_x|^2 - |H_y|^2) \\ & - \sqrt{2\varepsilon_L(\varepsilon+1)}(H_x{}^* H_z + H_x H_z{}^*)], \end{aligned}$$

where the H's are the hadronic currents for the given directions. H_x and H_y are transverse, H_z is longitudinal, the third term is proportional to σ_{TT} and the last term is $\propto \sigma_{LT}$. For electroproduction with unpolarized beam and target, since $H_x \approx H_y$, the σ_{TT} term in Eq. 1.9 can be zero. This is consistent with the present result showing a negligible value for the σ_{TT} contribution. Therefore, Eq. 1.8 can be abbreviated as

$$< |T_{fi}|^2 > \simeq \sum_{\lambda,\lambda'} [|H_x|^2 + \varepsilon_L |H_z|^2 - 2\sqrt{2\varepsilon_L(\varepsilon+1)} Re(H_x{}^* H_z)] \tag{5.22}$$

and Eq. 5.5 reduces to

$$i(\phi) = P_1 + P_2 \cos\phi. \tag{5.23}$$

Comparing Eq. 1.9 and 5.5, the contribution of the σ_{LT} term

$$\frac{P_2}{P_1} = \frac{\sqrt{2\varepsilon_L(\varepsilon+1)} \sin\theta \sigma_{LT}}{\sigma_T + \varepsilon_L \sigma_L} \tag{5.24}$$

$$= \frac{2\sqrt{2\varepsilon_L(\varepsilon+1)} \sin\theta Re(H_x{}^* H_z)}{|H_x|^2 + \varepsilon_L |H_z|^2} \tag{5.25}$$

$$= \frac{2\sqrt{2\varepsilon_L(\varepsilon+1)} \sin\theta Re(\frac{H_z}{H_x})}{(1+\varepsilon_L R)}, \tag{5.26}$$

where $Re(H_x{}^* H_z) = Re(\frac{|H_z|^2}{R} \frac{H_z}{H_x}) = |H_x|^2 Re(\frac{H_z}{H_x})$, and $R \equiv |H_z|^2/|H_x|^2 = \sigma_L/\sigma_T$. If we assume $Re(\frac{H_z}{H_x}) = \sqrt{R}$, then Eq. 5.26 becomes

$$\frac{P_2}{P_1} \simeq \frac{2\sqrt{2\varepsilon_L(\varepsilon+1)} \sin\theta \sqrt{R}}{(1+\varepsilon_L R)}. \tag{5.27}$$

By the substituting $R \simeq 0.8$ from [11] at $Q^2 \simeq 0.5$ GeV^2,

$$\frac{P_2}{P_1} \simeq \frac{2 \cdot \sqrt{2 \cdot 0.08(1+0.75) \cdot 0.8}}{(1+0.08 \cdot 0.8)} \sin 11.0^\circ = 0.15.$$

From another independent analysis [23], $R \simeq 0.2$, $\frac{P_2}{P_1} = 0.08$, which is closer to the result in shown Fig. 5.11.

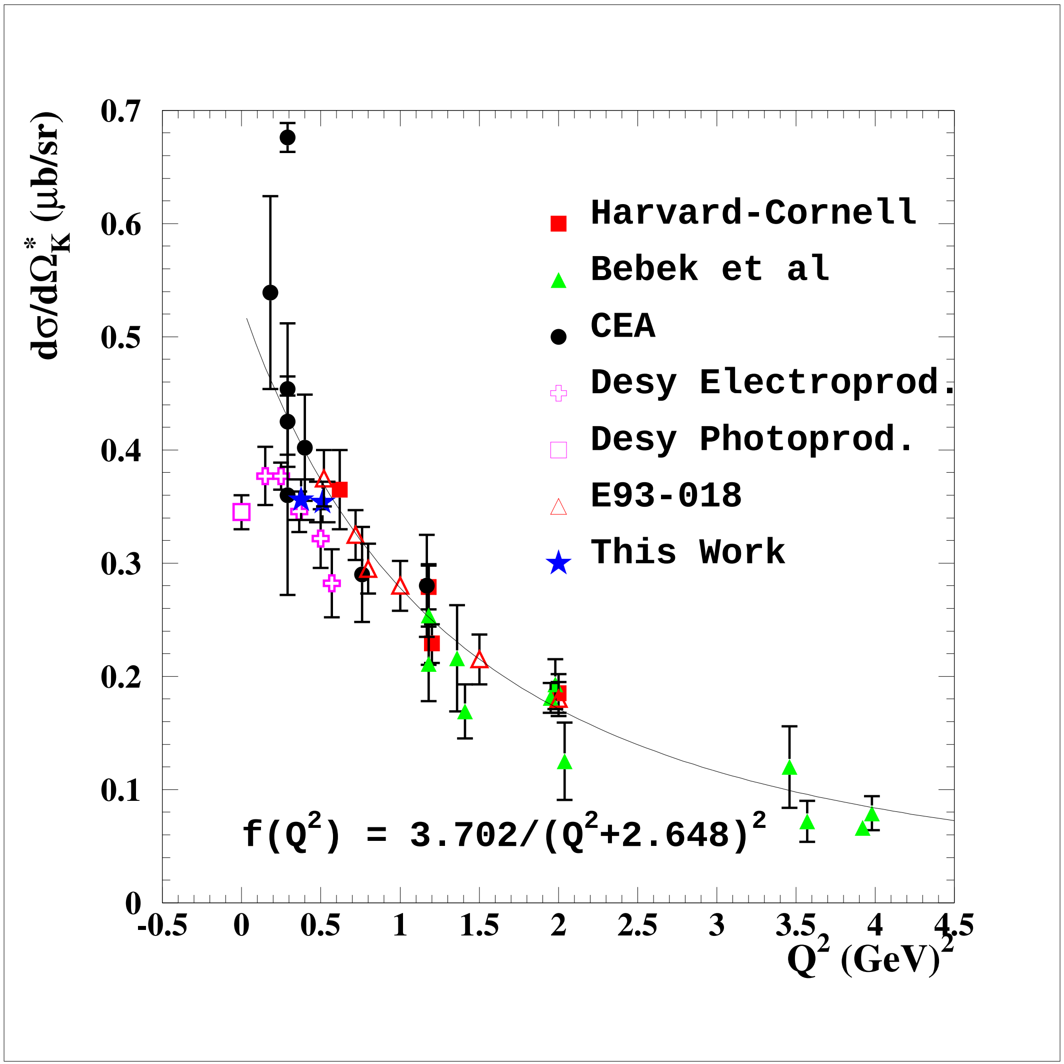

Figure 5.24: The Q^2 dependence of the unpolarized differential cross section for the reaction $\gamma^{(*)}+p \rightarrow K^{+}+\Lambda$. All cross sections are scaled to $W = 2.1$ GeV. The curve shown is a dipole fit through the previous data points for Λ electroproduction [11].

5.4.2 Deuteron

The cross sections for the angular dependence of kaon electroproduction of Λ, Σ^0, and Σ^- on deuterium have been extracted with an assumption, namely the proton in the deuteron is the same as the free proton. For Λ and Σ^0 production, the ratio of deuteron to hydrogen cross sections $\approx 0.987 \pm 0.027$. This consistent with the simple simulation for neutron shadowing or K^+ absorption on the deuteron, described in Section 5.3.5. The ratio of Σ^- to Σ^0 $\approx$ 0.61 ± 0.07 for data at all angles for two different Q^2, 0.38 and 0.50 GeV^2. The FSI between hyperon and nucleon in Monte Carlo simulations is compared to data and shown in Fig. 5.20. The three different models for Λ-n FSI were used to fit the missing mass spectra of data near the Λ threshold. The data are not able to distinguish the difference between Verma and Jülich model A, but exclude Jülich model B.

After data subtracted by the simulation with the quasi-free model including FSI, the rest of the missing mass spectra are shown in Fig. 5.25. A sharp spike at threshold of the Σ^- production, $\sim$ 2.134 GeV, remains. This may be the Σ^--p Coulomb bound state, predicted in [54], but the data is inconclusive.

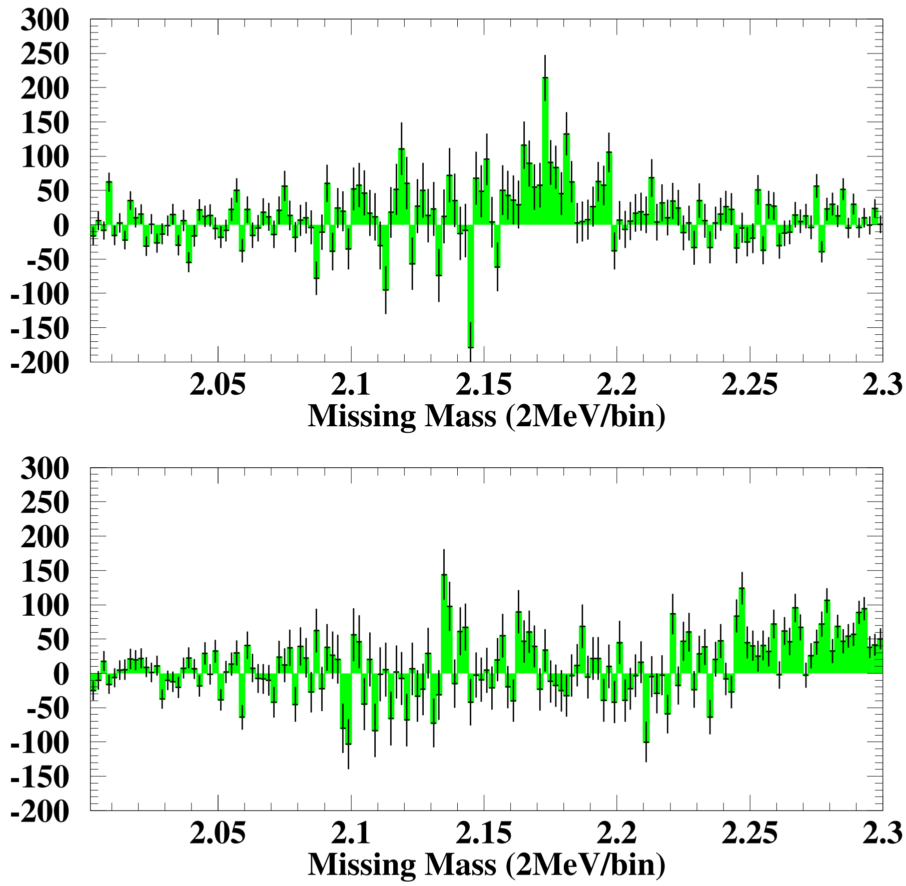

Figure 5.25: The remainder of the missing mass spectrum for two different Q^2 settings after the Monte Carlo simulations including FSI of $D(e, e'K^+)YN$ were subtracted from data. Top is the sum of four angle sets for $Q^2 = 0.5$ GeV^2 and bottom is the sum of three angle sets for $Q^2 = 0.38$.

CHAPTER 6

SUMMARY AND CONCLUSION

The angular distributions of kaon electroproduction on the hydrogen and deuterium have been measured. Missing mass distributions obtained from the hydrogen target show two well separated peaks which can be associated with Λ and Σ^0 production. Cross sections for the two reaction channels are extracted by comparison with MC simulations. The angular dependence for Λ production is well described by a previous parameterization which shows an exponential fall-off as a function of the related Lorentz invariant variable, t. In the dynamic range covered by this experiment, the cross section does not depend on Q^2 in contrast to a previous parameterization, predicted by most theoretical models, which assumed a kaonic monopole form factor. Our data, however, lead to the previous photo-production point ($Q^2 = 0$). In the low W regions, the extracted cross section increases with decreasing W, a trend that is not expected from simple phase space arguments. This energy region has not been explored by previous experiments which missed the resonance region. The cross section dependence on W was parameterized with the phase space factor and a Breit-Wigner resonance form with a fixed resonance, N(1720), one of two dominant nucleon resonances decaying into Λ and K^+. Since data below $W \sim 1.72$ GeV is missed, a region where the cross section is rising, it is not possible to determine a precise value for the resonance mass. The fit, however, passes through all the points, including the N(1720) resonance. At the far forward settings, for the first time, the ϕ dependence shows an σ_{LT} contribution which is $\sim$ 11 % of the average cross section and a negligible effect for σ_{TT}. The Σ^0 production depends mainly upon a phase space factor. The cross section for Σ^0 is less dependent on $\theta_{\gamma K}$, the kaon scattering angle respect to the virtual photon, than the Λ.

E91-016 is the first measurement on deuterium with sufficient resolution and statistics to separate the contribution from Λ and Σ production. The data show the Λ–Σ separation in the missing mass spectrum on deuteron. The missing mass spectra of the deuteron are well described by quasi-free production including Y-N FSI. The cross sections of Λ, Σ^0, and Σ^- on deuterium have been measured with an assumption in which the nucleons in the deuteron are assumed to be free, i.e. quasi-free. The Λ ratios of deuterium/hydrogen are about 99 %, for the all kinematic settings, a result that can be explained by simple neutron shadowing or a K^+-n absorption model. This result implies that the proton in the deuteron can be treated as a free proton. Hence, we are allowed to separate the two Σ productions on the deuteron by treating the cross section of Σ^0 on the deuteron as being nearly equal to that for hydrogen. With this assumption, we find the ratio Σ^-/Σ^0 is $\simeq 0.6$, consistent for all kinematics, and measured the angular dependence of Σ^-. The constant ratios of Λ on deuterium to hydrogen and Σ on neutron to proton support the statement that nucleons in the deuteron can be regarded as free nucleons. With the simple comparison of the Clebsch-Gordan coefficients, isospin-$\frac{3}{2}$ exchange agrees better with data for Σ production than isospin-$\frac{1}{2}$ exchange. This may provide a basis for the production of Σ-hypernuclei. In order to understand the strong enhancements in the missing mass spectra near the thresholds for hyperon production, however, we applied final-state Y-N interactions. Even though the FSI is a small contribution compared to the entire distribution, it is a large contribution near the threshold of each production, particularly for Σ-N. The Λ-n FSI has been measured for the first time. For the Λ-n FSI, we tested the various models with two different spin states. The data not only differentiate between different models to some extent, but also between two different spin states of the Λ-n system, qualitatively. The singlet model is more consistent with data, and implies spin-flip of the struck nucleon. The Λ-n scattering length is consistent with a value, ≈ -1.6 fm. For the Σ-N interaction, the best fit to the data near threshold yields an influence factor roughly 7 times larger than in the Λ-n interaction. This strong interaction of Σ-N can be explained by pion exchange in the intermediate state. After subtracting the quasi-free production including FSI from the data for the low Q^2 setting, a sharp structure remains at the Σ^- threshold rather than at the Σ^0. The width is approximately the experimental resolution. It may be due to either Σ^--p FSI or a quasi-bound nucleus resulting from the Coulomb interaction. There is no evidence for this peak at $Q^2 = 0.5$ GeV^2. The initially proposed cusp effect was not observed at a missing mass of 2.13 GeV, the Σ^0-n threshold.

A significant set of kaon electroproduction data has been collected on hydrogen and deuterium. Some of results, however, may be different from previous interpretations due to the limitation of data; for example, the resonance in the W dependence and the Q^2 dependence leading to the photoproduction point. In Λ production, to evaluate the exact resonance channel in the low W dependence and to understand the cross section behavior near $Q^2 \sim 0$, there is a need for new data in which the dependences are measured continuously with high precision down to the lowest values. The former will provide the specific s-channel contribution which may require modification of theoretical models. The latter may also lead to change in the theorists' assumption of a monopole kaonic form factor. Although Λ-n FSI in kaon electroproduction has rarely been discussed by theorists, the data are able to distinguish one model from the others. An additional precise measurement of $D(e, e'K^+)$ at $Q^2 \approx 0$ can distinguish between the remaining two models. As mentioned in ref. [15], the Σ^--p FSI in the exclusive measurement on deuterium, $D(e, e'K^+p)\Sigma^-$ or $D(e, e'K^+\Sigma^-)p$ will be much stronger than in the inclusive reaction,$D(e, e'K^+)\Sigma^- p$. Therefore, the exclusive measurement of the Σ^- production on deuterium can provide precise information on Σ^--p FSI.

BIBLIOGRAPHY

[1] SAPHIR Collaboration. *Phys. Lett.*, B445:20–26, 1998.

[2] R.A. Adelseck and B. Sagahai. *Phys. Rev.*, C42:108, 1990.

[3] R. Williams, C.-R. Ji, and S. R. Cotanch. *Phys. Rev.*, C46:1617, 1992.

[4] J. C. David, C. Fayard, G. H. Lamot., and B. Saghai. *Phys. Rev.*, C53:2613, 1996.

[5] T. Mart, C. Bennhold, and C. E. Hyde-Wright. *Phys. Rev.*, C51:1074, 1995.

[6] R.A. Adelseck and B. Sagahai. *Phys. Rev.*, C45:2030, 1992.

[7] J. de Swart. *Rev. Mod. Phys.*, 35:916, 1963.

[8] X. Li and L. E. Wright. *J. Phys.*, G17:1127–1137, 1991.

[9] J. D. Walecka. *Lecture Notes.* Argonne National Laboratory (unpublished), 1983.

[10] G. Knöchlein, D. Drechsel, and L. Tiator. *Z. Phys.*, A352:327–343, 1995.

[11] G. Niculescu et al. *Phys. Rev. Lett.*, 81:4576–4579, 1998.

[12] C.J. Bebek et al. *Phys. Rev.*, D15:594, 1977.

[13] P. Brauel et al. *Z. Phys.*, C 3:101, 1979.

[14] R.A. Adelseck. PhD thesis, Ohio University (unpublished), 1988.

[15] X. Li, L. E. Wright, and C. Bennhold. *Phys. Rev.*, C45:2011, 1992.

[16] A. M. Boyarski et al. *Phys. Lett.*, B34:547, 1971.

[17] D.J. Quinn et al. *Phys. Rev.*, D20:1553, 1979.

[18] V. Cook et al. *Phys. Rev. Lett.*, 7:182, 1961.

[19] F. M. Renard and Y. Renard. *Phys. Lett.*, 24B:159, 1967.

[20] C. B. Dover and G. E. Walker. *Phys. Rep.*, 89:1, 1982.

[21] G. Niculescu. PhD thesis, Hampton University (unpublished), 1998.

[22] D. M. Koltenuk. PhD thesis, University of Pennsylvania (unpublished), 1999.

[23] R. M. Mohring. PhD thesis, University of Maryland (unpublished), 1999.

[24] C. Armstrong. *Beam Current Mesaurement in Hall C.* Hall C internal report (unpublished), 1996.

[25] Wendy Hinton. PhD thesis, Hampton University (unpublished), 2001.

[26] J. Dunne. *Cryo and Dummy Target Information*, 1998.

[27] M. Berz. *Technical report USUCL-977.* Michigan State University (unpublished), 1995.

[28] G. Heyes et.al. In *Proc. of the TOOLS 8 Conference*, pages 171–183, July 1992.

[29] G. Heyes et.al. In S. Loken, editor, *Proc. of the CHEP Conference*, pages 122–126, Apr. 1994.

[30] D. Abbott et. al. In R. Fox, editor, *Proc. of the IEEE Conference on Real-Time Computer Applications in Nuclear, Particle, and Plasma Physics*, page 147, Michigan State University - NSCL, 1995.

[31] *Introduction to Q.* LAMPF Technical report (unpublished), 1972.

[32] C. Armstrong. *Hall C analysis engine routine flow,* Hall C internal report (unpublished), 1995.

[33] D. Van Westrum. PhD thesis, University of Colorado (unpublished), 1998.

[34] K. Assamagan, D. Dutta, and P. Welch, *Hall C Matrix Element Optimization Package (CMOP)*, CEBAF Hall C Internal Report (unpublished), 1997.

[35] K. Assamagan, Private communication, 1997.

[36] R. Ent, Private communication, October 1997.

[37] Y. Chen, Private communication, 1997.

[38] I. Niculescu, *Shower Counter and Čerenkov Efficiencies.* CEBAF Hall C Internal Report (unpublished), 1997.

[39] E. J. Weinberg and D. L. Nordstrom, *Phys. Rev.*, D54(part I), 1996.

[40] W. Weise. *Il Nuovo Cimento*, 102A:265, 1989.

[41] C. Caso et al. *The European Physical Journal*, C3:1, 1998.

[42] R.J. Abrams et al. *Phys. Rev.*, D4:3235, 1971.

[43] J. Reinhold, Private communication, 1998.

[44] N. C. R. Makins at al. *Phys. Rev. Lett.*, 72:1986, 1994.

[45] N. Makins. PhD thesis, Massachusetts Institute of Technology (unpublished), 1994.

[46] T.G. O'Neill. PhD thesis, California Institue of Technology (unpublished), 1994.

[47] P. Brauel. PhD thesis, Internal Report DESY F22-78/04 (unpublished), 1978.

[48] *HBOOK Reference Manual*, CERN Program Library Long Writeups Y250, 1995.

[49] R.A. Adelseck and L. E. Wright, *The American Physical Society*, 39:580, 1988.

[50] K. M. Maung, Private communication, 1998.

[51] K. Heyde, *Basic Ideas and Concepts in Nuclear Physics.* Institute of Physics Publishing, 1994.

[52] C. W. DeJager, H. DeVries, and C. DeVries, *At. Data Nucl. Data Tables*, 14:479, 1977.

[53] J. Reinhold, Private communication, 2000.

[54] B. Zeidman, Electroproduction of kaons and light hypernuclei. PR-89-013, CEBAF Internal Report (unpublished), 1991.

[55] P. Feller et al., *Nuclear Physics*, B39:413, 1972.

APPENDIX A

AZIMUTHAL ANGLE (ϕ) DISTRIBUTION

Since **E91-016** central kinematics was set near the threshold of Σ production on deuterium, the Λ production on the hydrogen target is not precisely parallel kinematics. Therefore unseparated cross sections at the forward settings have contributions from interference terms. The following pictures show the azimuthal angle distributions of Lambda production on hydrogen. As shown in Fig A.4, the sum of $P_{SOS} = 1.077$ and 0.929 GeV/c settings at $Q^2 = 0.5$ GeV^2 minimize those contribution.

All figures are defined so that the x-axis $= |t| \cos\phi$ and the y-axis $= |t| \sin\phi$.

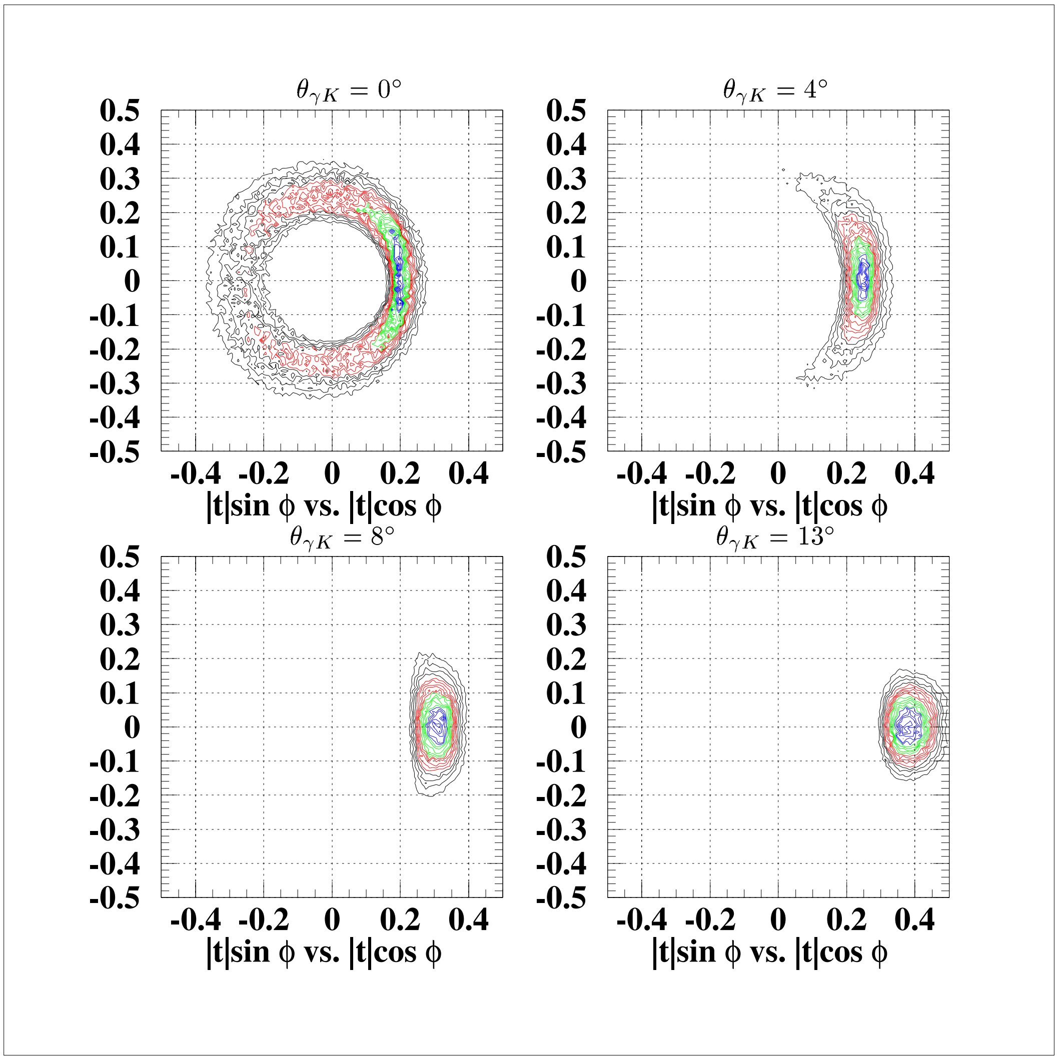

Figure A.1: ϕ distributions of Λ production for the four different angle settings at $P_{SOS} = 1.077$ GeV/c and $Q^2 = 0.50$ GeV^2.

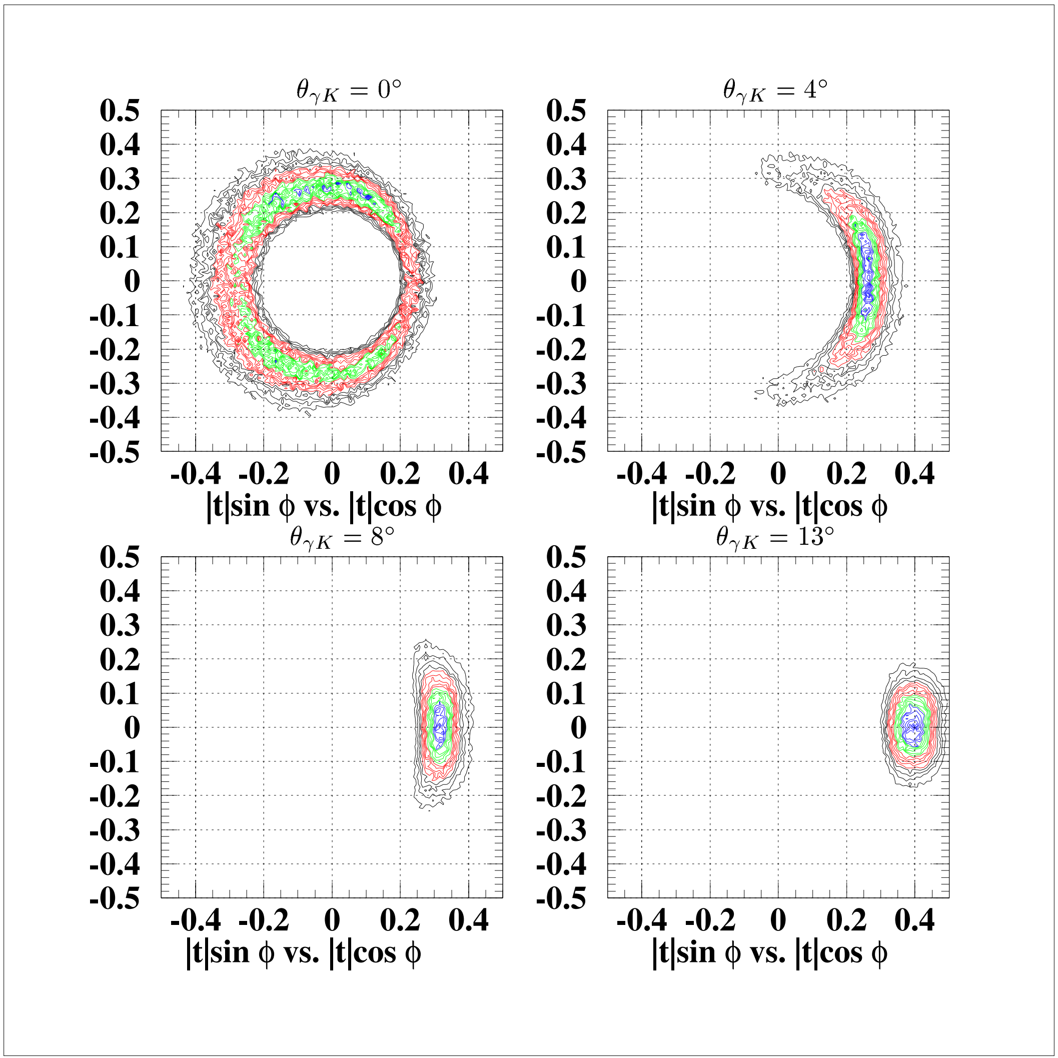

Figure A.2: ϕ distributions of Λ production for the four different angle settings at $P_{SOS} = 0.929$ GeV/c and $Q^2 = 0.50$ GeV^2.

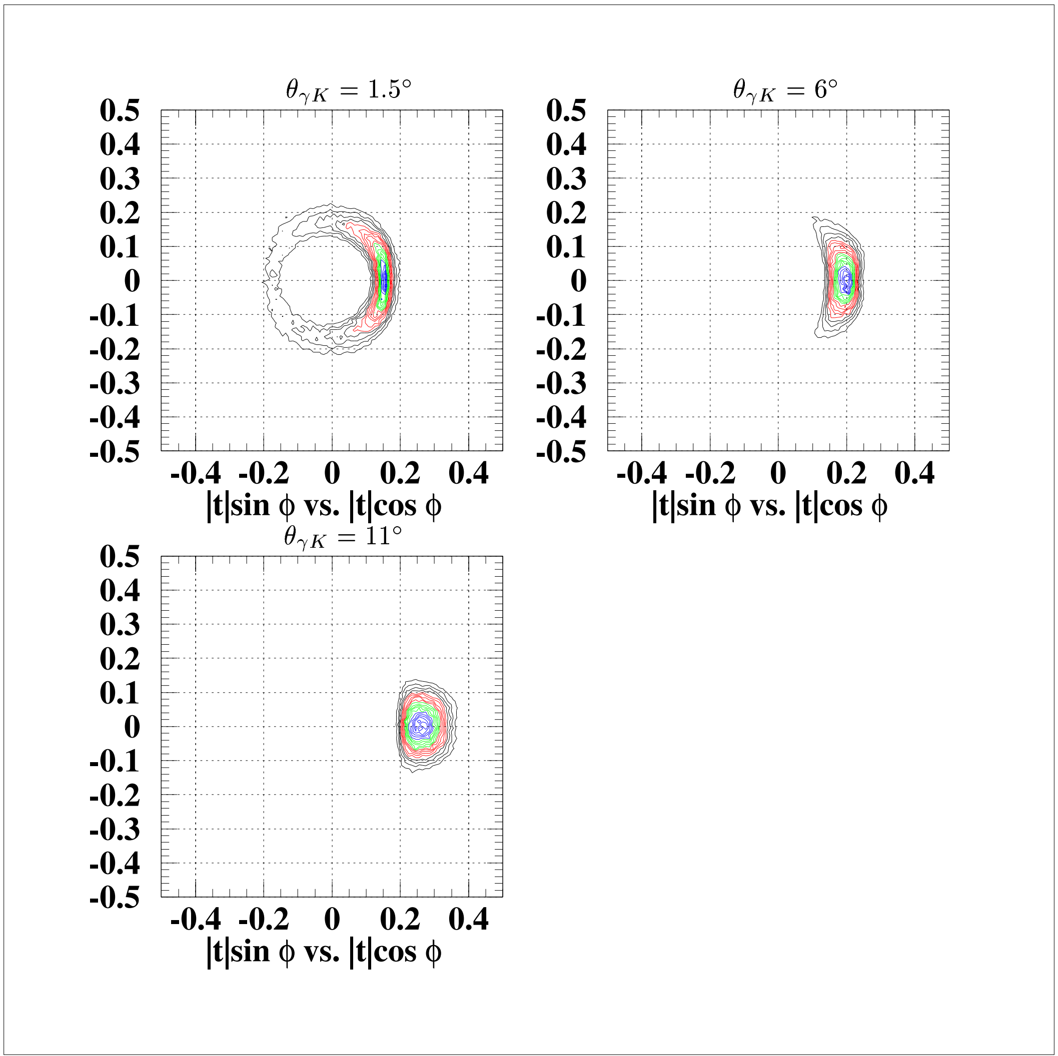

Figure A.3: ϕ distributions of Λ production for the three different angle settings at $Q^2 = 0.38$ GeV^2.

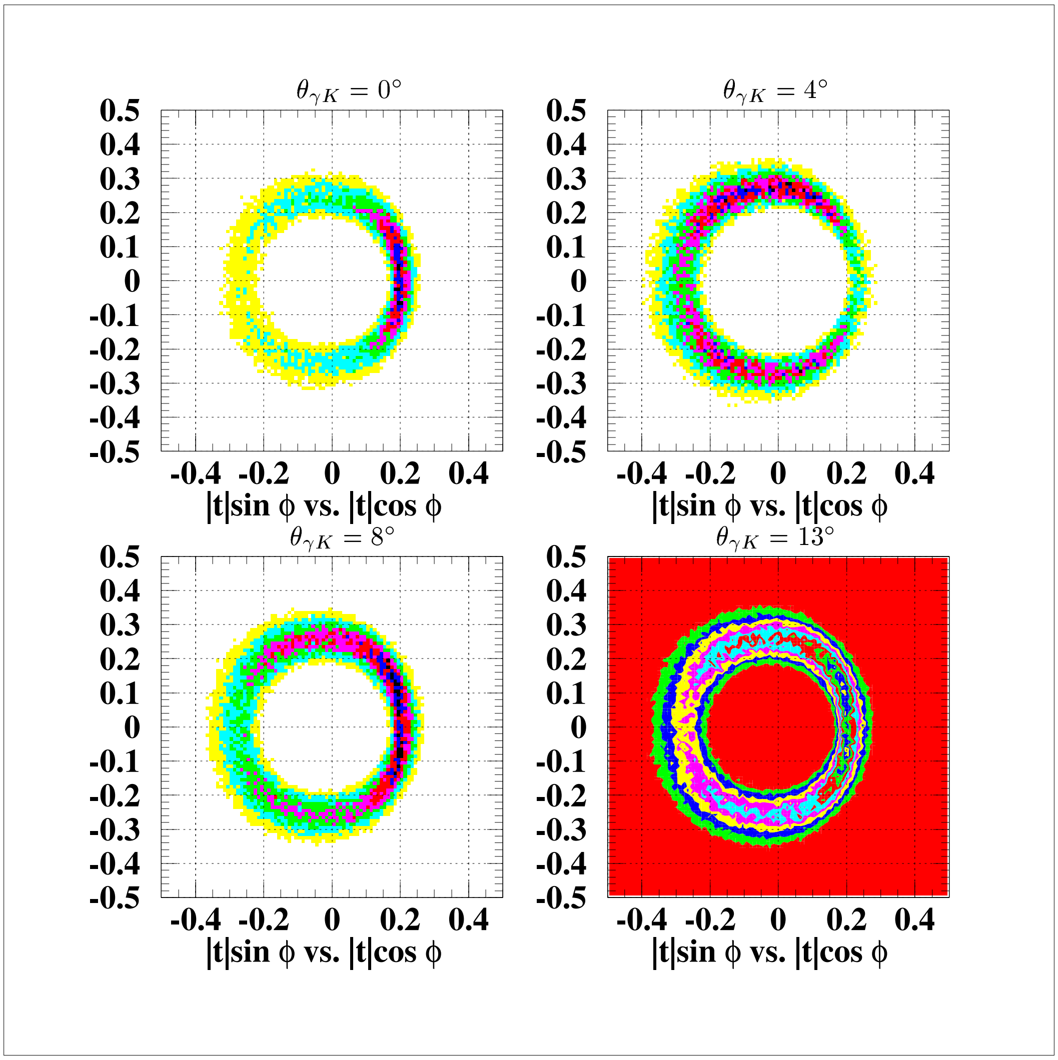

Figure A.4: ϕ sum distributions of P_{SOS} = 1.077 and 0.929 GeV/c settings at $Q^2 = 0.50$ GeV^2.

APPENDIX B

THE COMPARISON OF SOS DELTA SPECTRA

The following pictures of SOS delta spectra are comparisons of data and MC simulations for the $H(e,e'K^+)\Lambda$ reaction. Both data and simulations are cut in missing mass between 1.1 and 1.16 GeV. In each figure, top is the data and MC simulation with initial model cross section while the bottom indicates application of the fitted cross section. The setting numbers are defined in Table 2.7.

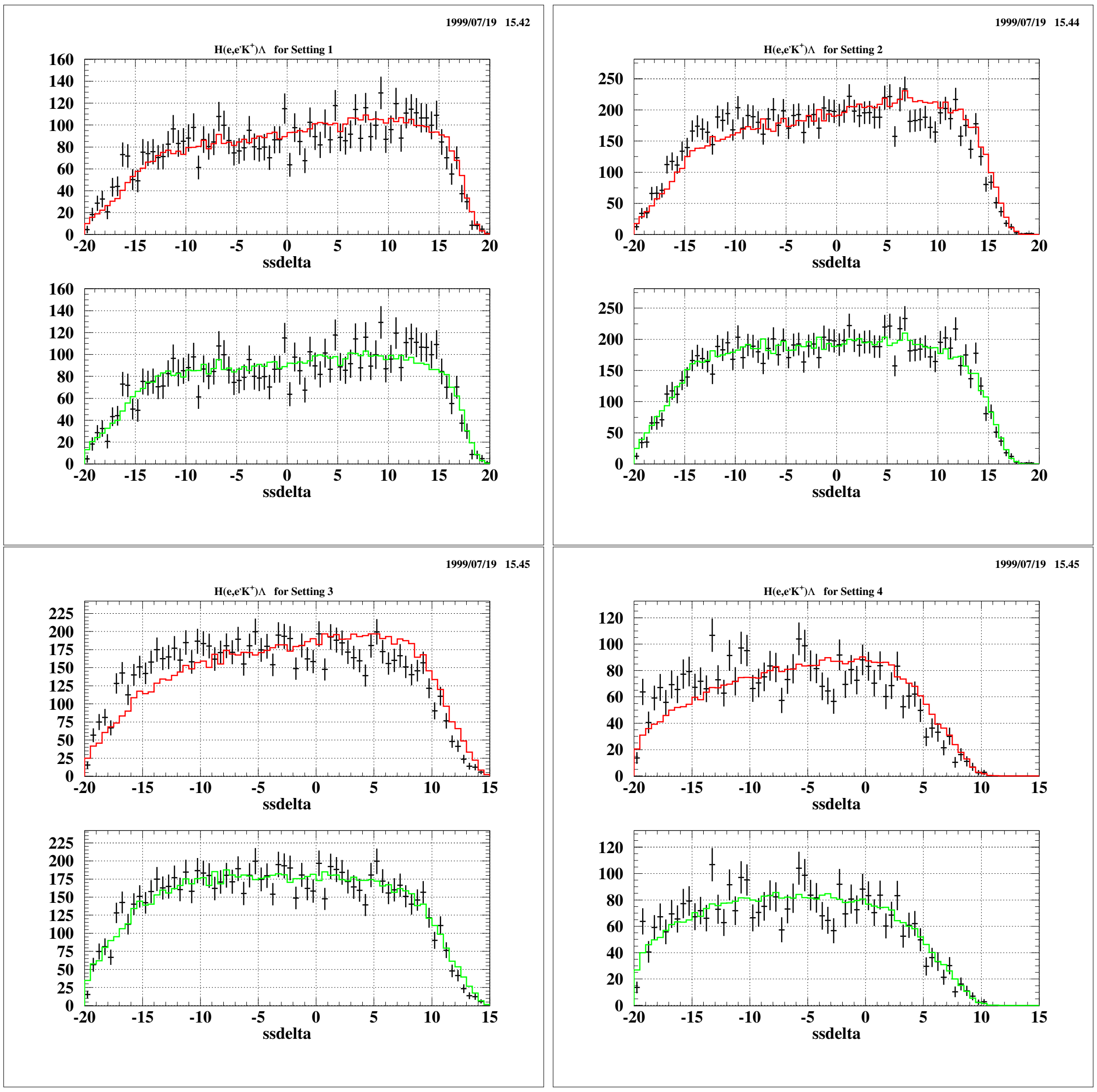

Figure B.1: SOS delta, $\frac{P-P_0}{P_0}$, comparisons of data and MC for set numbers 1–4 as defined in Table 2.7 for $Q^2 = 0.50$ GeV^2 settings.

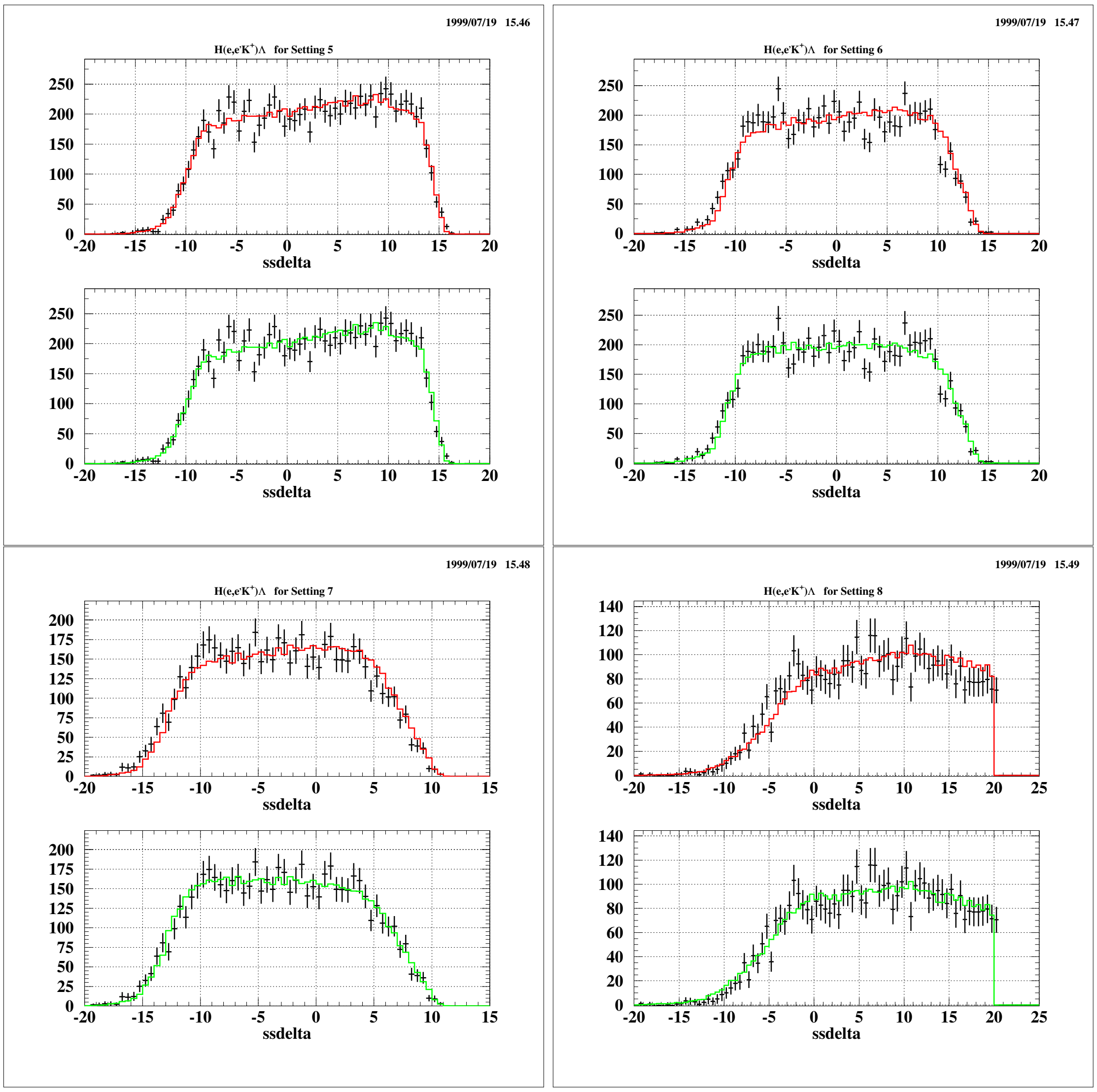

Figure B.2: Figures similar to Fig. B.1, for set numbers 5–8, $Q^2 = 0.50$ GeV^2 settings.

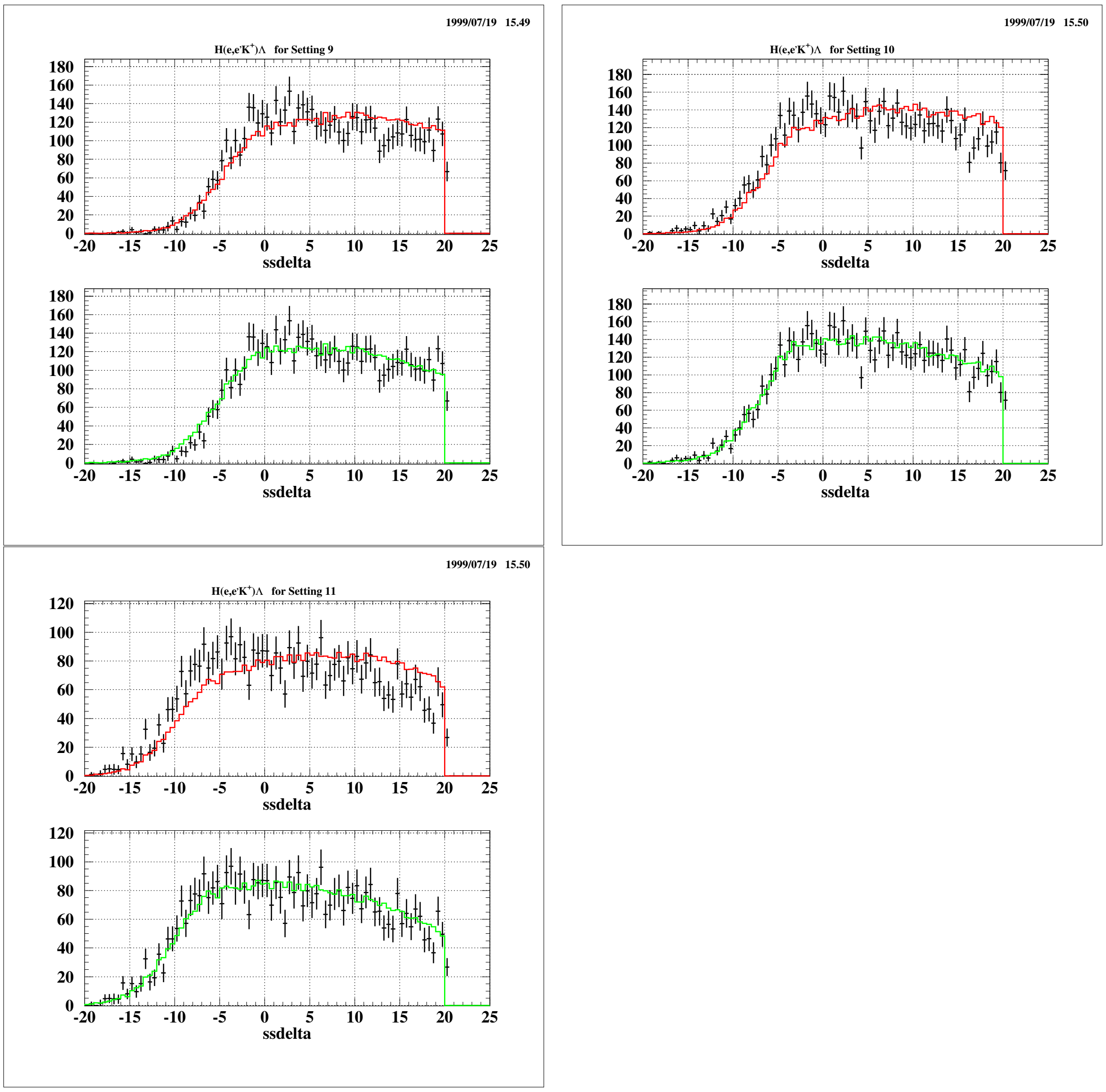

Figure B.3: Figures similar to Fig. B.1, for set numbers 9–11, $Q^2 = 0.38$ GeV^2 settings.

APPENDIX C

SCATTERING PROBLEM IN P-SPACE

In two body N-N scattering with potential V, the general form of the total Hamiltonian can be written as

$$\mathbf{H} = \mathbf{H}_\circ + \mathbf{V}, \tag{C.1}$$

where V is obtained from equation 5.11, $H_\circ = \hbar^2 k^2/2\mu$; $\mu = M_Y M_N/(M_Y + M_N)$, and M_Y and M_N are the masses of the hyperon and nucleon, respectively. The Lippmann-Schwinger equation for the scattering state is

$$|\psi >= |\bar{k} > + \mathbf{G}_\circ \mathbf{V} |\psi >, \tag{C.2}$$

where $\mathbf{G}_\circ$ is the Green's function operator,

$$\mathbf{G}_\circ = \frac{1}{E_k - H_\circ + i\eta} = \int \frac{|\bar{k}'' >< \bar{k}''|}{E_k - E''_k + i\eta} d\bar{k}'', \tag{C.3}$$

and $E_k = \hbar^2 k^2/2\mu$. The transition operator, $\mathbf{T}$, is defined by

$$\mathbf{V}|\psi >= \mathbf{T}|\bar{k} > \tag{C.4}$$

$$\mathbf{T}|\bar{k} >= \mathbf{V}|\bar{k} > + \mathbf{V}\mathbf{G}_\circ \mathbf{V}|\psi > \tag{C.5}$$

$$\mathbf{T}|\bar{k} >= \mathbf{V}|\bar{k} > + \mathbf{V}\mathbf{G}_\circ \mathbf{T}|\bar{k} > \tag{C.6}$$

$$< \bar{k}'|\mathbf{T}|\bar{k} >=< \bar{k}'|\mathbf{V}|\bar{k} > + \int \frac{< \bar{k}'|\mathbf{V}|\bar{k}'' >< \bar{k}''|\mathbf{T}|\bar{k} >}{E_k - E_{k''} + i\eta} d\bar{k}'' \tag{C.7}$$

The **T**-operator can therefore be written as

$$\mathbf{T} = \mathbf{V} + \mathbf{V}\mathbf{G}_{\circ}\mathbf{T} = \mathbf{V} + \mathbf{T}\mathbf{G}_{\circ}\mathbf{V} \tag{C.8}$$

For elastic scattering, $< \bar{k}'|\mathbf{T}|\bar{k} >$ with $|\bar{k}| = |\bar{k}'|$ has been solved using the **R**-operator,

$$\mathbf{R} \equiv \mathbf{V} + \mathbf{V}\tilde{\mathbf{G}}_{\circ}\mathbf{R} = \mathbf{V} + \mathbf{R}\tilde{\mathbf{G}}_{\circ}\mathbf{V}, \tag{C.9}$$

where

$$\tilde{\mathbf{G}}_{\circ} = \mathbb{P}\mathbf{G}_{\circ} \tag{C.10}$$

and $\mathbb{P}$ stands for principal value. From equation C.9,

$$\mathbf{V} = (1 + \mathbf{R}\tilde{\mathbf{G}}_{\circ})^{-1}\mathbf{R}. \tag{C.11}$$

Substituting equation C.11 in C.8 gives $\mathbf{T} = (1+\mathbf{R}\tilde{\mathbf{G}}_{\circ})^{-1}\mathbf{R} + (1+\mathbf{R}\tilde{\mathbf{G}}_{\circ})^{-1}\mathbf{R}\mathbf{G}_{\circ}\mathbf{T}$, then $\mathbf{T} = \mathbf{R} + \mathbf{R}(\mathbf{G}_{\circ} - \tilde{\mathbf{G}}_{\circ})\mathbf{T}$. Using the relation that

$$\frac{1}{x \pm i\eta} = \frac{x \mp i\eta}{x^2 + i\eta^2} = \mathbb{P} \mp i\pi\delta(x),$$

where $\delta(x) = \lim_{\eta \to 0} \frac{1}{\pi}\frac{\eta}{x^2+\eta^2}$,

$$\mathbf{G}_{\circ} - \tilde{\mathbf{G}}_{\circ} = \frac{1}{E_k - H_{\circ} + i\eta} - \mathbb{P}\frac{1}{E_k - H_{\circ}} = -i\pi\delta(E_k - H_{\circ}).$$

Therefore the operator T can be rewritten as

$$\mathbf{T} = \mathbf{R} - i\pi \mathbf{R}\delta(E - H_\circ)\mathbf{T}. \tag{C.12}$$

Substituting equation C.3 and C.10 into C.9, yields

$$< \bar{k}'|\mathbf{R}|\bar{k} > = < \bar{k}'|\mathbf{V}|\bar{k} > + \mathbb{P}\int \frac{< \bar{k}'|\mathbf{V}|\bar{k}'' >< \bar{k}''|\mathbf{R}|\bar{k} >}{E_k - E_{k''}} d\bar{k}'' \tag{C.13}$$

For any operator $\mathbf{O}$ ($\mathbf{V},\ \mathbf{R},\ \mathbf{T}$ etc),

$$\begin{aligned} < \bar{k}'|\mathbf{O}|\bar{k} > &= \sum_{l=0}^{\infty}\sum_{m=-l}^{l} \mathbf{O}_l(k',k){Y^*}_{lm}(\hat{k}')Y_{lm}(\hat{k}) \\ &= \sum_{l=0}^{\infty} \frac{2l+1}{4\pi}\mathbf{O}_l(k',k)P_l(\hat{k}',\hat{k}.) \end{aligned}$$

From the second relation, the equation can be changed to

$$\mathbf{O}_l(k',k) = 2\pi \int_{-1}^{+1} < \bar{k}'|\mathbf{O}|\bar{k} > P_l(x)dx \tag{C.14}$$

by using $\int_{-1}^{+1} P_{l'}(x)P_l(x)dx = 2\delta_{ll'}/(2l+1)$ where $x \equiv \hat{k}' \cdot \hat{k} = \cos\theta_{\hat{k}'\hat{k}}$. Now by expanding in partial waves and using

$$\int {Y^*}_{l'm'}(\hat{k''})Y_{lm}(\hat{k''})d\hat{k''} = \delta_{ll'}\delta_{mm'}, \tag{C.15}$$

the result is

$$\mathbf{R}_l(k',k) = \mathbf{V}_l(k',k) + \mathbb{P}\int_0^\infty \frac{\mathbf{V}_l(k',k'')\mathbf{R}_l(k'',k)}{E_k - E_{k''}} k''^2 dk''. \tag{C.16}$$

This equation was solved numerically.

C.1 The Fortran Code for N-N scattering

```
c
c     This program solve Lippmann-Schwinger equation for the
c     transition operator in momentum space. First, for each L
c     the on-shell reaction matrix RL(k,K) is solved and TL(k,K)
c     is found from Heitler equation. The scattering amplitude is calculated
c     from the sum over (2L+1)TL(K,K)PL(x)/4pi. The infinite number of
c     partial waves are essentially included by using the Born approximation
c     at L=Lmax+1  where Lmax+1 is the value of L at which VL(k,K)
c     is the same as TL(K,K) within a given tolerance.
c
c     Variables and parameters
c
c     XI= pure imaginary sqrt(-1)
c     TOL= tolerance for TL(k,K)-VL(k,k)
c     hbarc= plank const/(2 pi) * velocity of light = 197.3285 MeV Fm
c     AMPJ= mass of projectile in MeV
c     AMTAG= mass of target in MeV
c     FMU=nonrelativistic reduced mass
c     HB2BYM= hbar**2/(mass of proton) =41.47 MeV Fm**2
c     NR=1 nonrelativistic kinematics
c     NR=0 relativistic kinematics
c     N1= integration point for 0 to 2k  integration (k=cm wave vector)
c     N2= integration points for 2k to infinity integration
c     NRP1=N1+N2+1 on shell point. wavevector with this index is
c          the in coming wave vector.
```

```
c     LPJMAX= initial set up value for maximum L=0,1,2,3,4 etc
c     Gauss(x,y,N) = subroutine to calcualte the standard Gauss
c                    points and weights. x(i) are the points, Y(i) are
c                    the weights. x(i) are in -1 to +1
c     TLAB= incoming Lab energy of the projectile
c     TCM= for nonrelativistic case it is the c.m energy
c     SKZ= c.m wavevector corresponding to the incoming energy
c     RHO= k dk/de density of states per unit energy
c     EON= on shell energy
c     EOFF= off shell energy
c     SKK(I)= intermediate wavevector vcariable. ie. integration variable.
c     VLKKP(sk,skp ,LL,v2) = routine to calculate V2=VL(k,k') for given
c                           pair of wavevector k and k' for the LLth
c                           partial wave. NOTE LL =0,1,2, the physical L
c     UL(k,kp)= VL(k,k')=v2
c
      implicit double precision(a-h,o-z)
      DIMENSION X(200),W(200),SKK(201),WT(200),pols(201),pol(201)
      dimension delta1(60)
      COMPLEX*16 GREN(201,201),UL(201,201),V(201),fthed,delta1
      COMPLEX*16 XI,DELTA,RON,TON(60),TBORN(60),V2,UOFQ,FTHECM,vv,vv1
      COMPLEX*16 EXPONC,FCOUL,FNUPC,fqcm,b3d,fthe(200),fthe1(200)
      complex*16 third,bsecnd,fvary,fborn
      common/const/pi,hbarc,hbarc3,amu,alpha,nr,skz,skznn
      common/poten/xvq(200),wvq(200),npot
c
c     Constants
c
      amu  =931.49431                               ! MeV/amu
      fnucl=938.272                                 ! Mass of Proton
      fnucl2=fnucl**2
      hbarc=197.32705                               ! MeV*fm
      hbarc2=hbarc**2
      pi=2.*dasin(1.d0)
      xi=(0.0,1.0)
      tol=0.01
c
```

```
      ampj = 1115.684
      ampj2=ampj**2
      amtag= 939.5656
      amtag2=amtag**2
      fmu=ampj*amtag/(ampj+amtag)
      fmunn=ampj*fnucl/(ampj+fnucl)
*
      do ntst=1,15
         skz = ntst*10.
      n1=40
      n2=40
      nrp1=n1+n2+1
*
*     Kinematics
*
      nr = 1
*
      L_value = 3
c
      if(nr.eq.1) then                ! Non-Relativ. (NR)
        skz = skz/hbarc                             ! (1/fm)
        skz2=skz**2
        eon=hbarc2*skz2/2./fmu        ! Kinetic Energy (MeV)
        rho=fmu*skz/hbarc2            ! Density of states/energy (1/(MeV*fm^3)
      else                            ! Relativistic Treaty
        print *,'skz =',skz/hbarc,'(fm-1),  ',skz,'(MeV)'
        skz2=skz**2
        ekpj=dsqrt(ampj2+skz2)
        ektag=dsqrt(amtag2+skz2)
        eon=ekpj+ektag
        rho=skz*ekpj*ektag/eon        ! Density of states/energy (MeV^2)
      endif
c
c     Get Gauss pts and wts for intgral v(q)Pl(x)dx
c
      npot=80
      call dgauss(xvq,wvq,npot)
c
```

```
c     Get gauss pts and wts. set the two integrals
c     first integral 0 to 2*skz ; use Y=MX+C
c     transformation and get M=C=skz for limits -1 to +1
c
      call dgauss(x,w,n1)
      do 20 i=1,n1
      skk(i)=skz*(x(i)+1.)
      wt(i)=w(i)*skz
  20  continue
c
c     do the second integration 2*skz to infinity.
c     use y=s+b*tan(pi*(x+1)/4)
c     get s=2*skz , b=skz , wt=w*pi*skz*sec*sec/4.
c
      call dgauss(x,w,n2)
      do 21 i=1,n2
      ii=i+n1
      coss=dcos(pi*(x(i)+1.)/4.)
      skk(ii)=2.*skz+2.*skz*dtan(pi*(x(i)+1.)/4.)
      wt(ii)=2.*pi*.25*skz/coss/coss*w(i)
  21  continue
c
c     set the last point as the on-shell momentum
c
      skk(nrp1)=skz
c
c     start the l-loop
c     LL = the physical L .(0,1,2,.....)
c
      write(2,401)
 401  format(2x,'L      tborn             ton            perre')
      lpjmax=L_value
      DO 30 LL=0,LPJMAX
      l=ll+1
c
c     start K',K'' loop
c
      do 40 kp=1,nrp1
```

```
      skp=skk(kp)
      gren(kp,nrp1)=(0.0,0.0)
      do 50 kpp=1,nrp1
      skpp=skk(kpp)
      call vlkkp(skp,skpp,ll,v2)
      ul(kp,kpp)=v2
      skpp2=skpp*skpp
      eoff=hbarc2*skpp2/2./fmu
      if(nr.ne.1)eoff=dsqrt(ampj2+skpp2)+dsqrt(amtag2+skpp2)
c
      delta=(0.0,0.0)
      if(kpp.eq.nrp1)goto 51
      gren(kp,kpp)=wt(kpp)*skpp2*ul(kp,kpp)/(eon-eoff)
  51  if(kp.eq.kpp)delta=(1.0,0.0)
      gren(kp,kpp)=delta-gren(kp,kpp)
  50  continue
  40  continue
c
c     Set the constant vector. i.e The B column matrix
c     in the matrix equation AX=B.
c
      do 60 i=1,nrp1
      v(i)=ul(i,nrp1)
  60  continue
      call leq1(gren,v,nrp1,201,det)
      ron=v(nrp1)
      ronr=dreal(ron)
      delrad=-datan(pi*rho*ronr)
      delta1(l)=delrad+xi*0.0
      ton(l)=ron/(1.+xi*pi*rho*ron)
c      print *,'ton(l)=',ton(l)
c      call vtest1(skz,skz,ll,vv)
      call vlkkp(skz,skz,ll,vv)
      tborn(l)=vv
      tonre=dreal(ton(l))
      tonim=dimag(ton(l))
```

```
      tbornre=dreal(tborn(l))
      tbornim=dimag(tborn(l))
      perre=abs(tbornre-tonre)/abs(tonre)
      perim=abs(tbornim-tonim)/abs(tonim)
      deldeg=delrad*180./pi
      deldega=abs(deldeg)
c
c     Test if tborn and ton are the same within given tolerance
c     defined at the top of program as tol
c
      if(perre.le.tol.and.perim.le.tol)goto 998
c
      write(*,61)LL,delrad
 61   format('Phase shift(L=',I2,')=',F10.7,'(rad)')
  30  CONTINUE
 998  continue
      lmax=ll
      lmax1=lmax-1
c
c     Now do the sum for the scattering amplitude
c     by using Born approximation, it essentially includes all
c     partial waves.
c
      write(2,402)
 402  format(1x,'the   LL    fthe               fthe1')
      totalc=0.0
      do 80 ithe=1,181
      the=float(ithe-1)
      ther=pi*the/180.
      q=2.*skz*dsin(ther/2.)                  ! (1/fm)
      q2=q*q                                 !
      xxx=dble(cos(ther))
      call vofq(q2,vq)
      call pl(xxx,lmax1,pol)
      fthe(ithe)=(0.0,0.0)
      fthe1(ithe)=(0.0,0.0)
      fthed=(0.,0.)
```

```
      do 90 ll=0,lmax1
      l=ll+1
      fthe(ithe)=fthe(ithe)+(2.*ll+1.)*ton(l)*pol(l)/4./pi
      fthe1(ithe)=fthe1(ithe)+(2.*ll+1.)*
     $(ton(l)-tborn(l))*pol(l)/4./pi
  90  continue
      fthe(ithe)=-fthe(ithe)*4.*pi*pi*rho/skz
      totalc=totalc+cdabs(fthe(ithe))**2*dsin(ther)*pi/180.*2.*pi
      fthe1(ithe)=-(fthe1(ithe)+vq)*4.*pi*pi*rho/skz
       fborn=-vq*4.*pi*pi*rho/skz
 330  format(2x,e12.5,2x,e12.5,2x,e12.5,2x,e12.5)
  80  continue
      tcross=4.*pi/skz*dimag(fthe(1))
      tcross1=4.*pi/skz*dimag(fthe1(1))
      print *,'tcross here next=',tcross
      print *,'tot X=',tcross*10. ,tcross1*10.,totalc*10.
c
 999  continue
      enddo
      STOP
      END
c***************************************
c*******************************************
      SUBROUTINE LEQ1(A,B,N,LA,DET)
c     implicit complex(a-h,o-z)
c     Leq1 solves the matrix equation AX=B
c     A = Coefficient matrix, solution stored in B
c     B = constant matrix
c     N = number of equations and unknowns
c     LA= dimension of the first subscript of A
c     **NOTE**  the matrix A(i,j) must be symmetric
c     This routine was originally used in WIZARD.
c
      COMPLEX*16  A(2), B(2)
      COMPLEX*16  R,T,DET
      REAL*8 CABS,T1,T2
c
      LNA=LA*N-LA
```

```
      DO 50 I=2,N
      II=I-1
      LJ=-LA
      DO 50 J=1,II
      LJ=LJ+LA
      LIJ=I+LJ
      LJJ=J+LJ
      T1=A(LIJ)*DCONJG(A(LIJ))
      IF(T1.EQ.0.0)GOTO 50
      T2=A(LJJ)*DCONJG(A(LJJ))
      IF(T2.LT.T1)GOTO 10
      GOTO 30
10    LNAO=LNA+1
      DO 20 LKO=1,LNAO,LA
      LK=LKO-1
      LJK=J+LK
      LIK=I+LK
      T=A(LJK)
      A(LJK)=A(LIK)
20    A(LIK)=-T
      T=B(J)
      B(J)=B(I)
      B(I)=-T
30    R=A(LIJ)/A(LJJ)
      LLJ=LJ+LA
      DO 40 LK=LLJ,LNA,LA
      LIK=I+LK
      LJK=J+LK
40    A(LIK)=A(LIK)-R*A(LJK)
      B(I)=B(I)-R*B(J)
50    CONTINUE
      LNN=N+LNA
      B(N)=B(N)/A(LNN)
      LI=LNA
      DO 70 II=2,N
      LI=LI-LA
      I=N-II+1
      KK=I+1
      T=0.0
```

```
      LK=LA*I-LA
      DO 60 K=KK,N
      LK=LK+LA
      LIK=I+LK
   60 T=T+A(LIK)*B(K)
      LII=I+LI
   70 B(I)=(B(I)-T)/A(LII)
      DET=(1.0,0.0)
      DO 80 J=1,N
      LJJ=J+(J-1)*LA
   80 DET=DET*A(LJJ)
      RETURN
      END
c**********************************************
      SUBROUTINE COUFAZ(MAXLL,ETAC,SCOU)
c     Obtain from D. J. Ernst
c     This routine calculates the Coulomb phases.
c     real*4 scou,etac
c     implicit double precision (a-h,o-z)
c     **NOTE**  All the double precision functions
c     of the original routine have been changed to single.
c
      DIMENSION SCOU(1),FT(5)
      MAXL=MAXLL
      ETA=ETAC
      ABETA=ABS(ETA)
      IF(MAXL-50)20,20,15
   15 MAXL=50
   20 IF(ABETA-1.E-06)30,30,50
   30 DO 40 I=1,MAXL
   40 SCOU(I)=0.E0
      GOTO 120
   50 C=1.E0/(ETA*ETA+2601.E0)
      CH=SQRT(C)
      THETA=ATAN(ETA/51.E0)
      DO 60 M=1,5
      FT(M)=SIN(THETA*(2.*M-1.))
   60 CONTINUE
```

```
      SIG2=50.5E0*THETA-ETA*(ALOG(CH)+1.E0)
      SIG2=SIG2-CH*(FT(1)/12.E0-C*(FT(2)/360.E0-C*(FT(3)/
     >1260.E0-C*(FT(4)/1680.E0-C*FT(5)/1188.E0))))
      LMAX1=50-MAXL
      IF(LMAX1)90,90,70
   70 DO 80 I=1,LMAX
      L=51-I
      SIG2=SIG2-ATAN(ETA/L)
   80 CONTINUE
   90 LMAX1=LMAX1+2
      SCOU(MAXL)=SIG2-ATAN(ETA/MAXL)
      IF(LMAX1-50)100,100,120
  100 DO 110 I=LMAX1,50
      L=51-I
      SCOU(L)=SCOU(L+1)-ATAN(ETA/L)
  110 CONTINUE
  120 CONTINUE
      RETURN
      END
C***********************************************
      SUBROUTINE INTER(XIN,YIN,Y,NINT,NMAX,DX,IZERO,IEND)
      COMPLEX*16 YIN(500),Y(500)
      real*8 XIN(500)
C
c     this routine does the linear interpolation on a
c     complex array Y. the array Y has NMAX no: of pts and the
c     corresponding X values are given by I*DX , where DX
c     is the spacing. (I=1 to NMAX). the array XIN is
c     the array of X values for which we want the
c     corresponding Y values. they are given in YIN.
c     NINT= the no: of X values to be interpolated.
c     IZERO=0 ==>YIN(I)=Y(1) for XIN< Xmin.
c     IZERO=1 ==>YIN(I)=0. for XIN< Xmin.
c     IEND=0  ==>YIN(I)=Y(NMAX)
c     IEND=1  ==>YIN(I)=0.
c
      DO 10 II=1,NINT
      YIN(II)=(0.0,0.0)
```

```
      F=XIN(II)/DX
      I=F
      IF(I.EQ.0)GOTO 20
      I1=I
      IF(I1.GT.NMAX)GOTO 30
      P=F-I
      I2=I1+1
      YIN(II)=(1.-P)*Y(I1)+P*Y(I2)
      GOTO 10
   20 IF(IZERO.EQ.1)YIN(II)=Y(1)
      IF(IZERO.NE.1)YIN(II)=(0.0,0.0)
      GOTO 10
   30 IF(IEND.EQ.1)YIN(II)=Y(NMAX)
      IF(IEND.NE.1)YIN(II)=(0.0,0.0)
   10 CONTINUE
      RETURN
      END
c***********************************************
      subroutine vtest(skp,skpp,ll,vv)
      implicit double precision (a-h,o-z)
      complex*16 xi,vv
      common/const/pi,hbarc,hbarc3,amu,alpha,nr,skz,skznn
      xi=(0.0,1.0)
      v1=-10.463
      v2=-1650.6
      v3=6484.2
      rfmu=.7
      fmu1=rfmu
      fmu2=4.*rfmu
      fmu3=7.*rfmu
      z1=(fmu1*fmu1+skp*skp+skpp*skpp)/skp/skpp/2.
      z2=(fmu2*fmu2+skp*skp+skpp*skpp)/skp/skpp/2.
      z3=(fmu3*fmu3+skp*skp+skpp*skpp)/skp/skpp/2.
      arg1=(z1+1.)/(z1-1.)
      arg2=(z2+1.)/(z2-1.)
      arg3=(z3+1.)/(z3-1.)
      const=1./pi/skp/skpp
      vv=const*(v1/rfmu*.5*dlog(arg1)+v2/rfmu*.5*dlog(arg2)+
```

```
     >v3/rfmu*.5*dlog(arg3))+xi*0.
      return
      end
*
c***********************************************
      subroutine vtest1(skp,skpp,ll,vv)
      implicit double precision (a-h,o-z)
      complex*16 xi,vv
      common/const/pi,hbarc,hbarc3,amu,alpha,nr,skz,skznn
      xi=(0.0,1.0)
      v1=-65.246
      if(nr.ne.1)v1=-65.246/hbarc
      rfmu=.6329
      if(nr.ne.1)rfmu=.6329*hbarc
      fmu1=rfmu
      z1=(fmu1*fmu1+skp*skp+skpp*skpp)/skp/skpp/2.
      arg1=abs((z1+1.)/(z1-1.))
      const=1./pi/skp/skpp
      vv=const*(v1*.5*dlog(arg1))+xi*0.
      return
      end
****************************************************
      subroutine vofq(q2,vq)
      implicit double precision(a-h,o-z)
      dimension x(200),w(200)
      common/const/pi,hbarc,hbarc3,amu,alpha,nr,skz,skznn
      common/poten/xvq(200),wvq(200),npot
      complex*16 xi,vq

      xi=(0.0,1.)
c      va = -167.34                 ! (MeV) , Model#1
c      b_a = 1.1                    ! (fm) , Model#1
      va = -373.94                 ! (MeV) , Model#2
      b_a = 0.79                   ! (fm) , Model#2
      vr = 246.80                  ! (MeV)
      b_r = 0.82                   ! (fm)
      if(nr.ne.1) then
      b_a = b_a/hbarc
```

```
      b_r = b_r/hbarc
      endif

      b_a2 = b_a*b_a
      b_r2 = b_r*b_r

      nv = 80
      vqa = va*b_a**3./(8.*pi*pi)*dsqrt(pi)/dexp(q2*b_a2/4.)  ! Attractive
      vqr = vr*b_r**3./(8.*pi*pi)*dsqrt(pi)/dexp(q2*b_r2/4.)  ! Repulsive
      vq = vqa + vqr + xi*0.
      return
      end
c**************************************************
      subroutine vlkkp(skp,skpp,lcall,vv)
      implicit double precision(a-h,o-z)
      dimension pol(101)
      common/const/pi,hbarc,hbarc3,amu,alpha,nr,skz,skznn
      common/poten/xvq(200),wvq(200),npot
      complex*16 xi,vq,vv
      xi=(0.0,1.)
      l=lcall+1
      vv=(0.,0.)
      do i=1,npot
      q2=skp*skp+skpp*skpp-2.*skp*skpp*xvq(i)
      call vofq(q2,vq)
      x=xvq(i)
      call pl(x,l,pol)
      vv=vv+vq*wvq(i)*pol(l)
      end do
      vv=vv*2.*pi+xi*0.
      return
      end
*
************************************************************
      SUBROUTINE DGAUSS(Y,WY,N)
c     This routine determines the N/2 positive zeros (x(N/2))
c     of the lengendre polynomial of order N.  Also the N/2
c     distinct weights for gaussian quadrature are calculated.
```

```
c     N is even and less then 101 .
c     The gaussian points  and weights calculated by this
c     routine agrees with the tables of Abrabowitz & Stegun
c     Handbook of Mathematical Functions [ pp. 916-919 ]
c     up to the 8th digit.
c     **NOTE**  this routine needs to call subroutine pl(x,n,pol)
c     to get values of Lengendre polynomials.
c
      DOUBLE PRECISION V,Z,Z1,P,P1,POL,DP,pi
      double precision x,w,y,wy
      DIMENSION X(200),W(200),POL(201)
      DIMENSION Y(1),WY(1)
      NP1=N+1
      M=N/2
      pi=2.d0*dasin(1.d0)
      Z=pi/(2.*FLOAT(N))
      DO 20L=1,M
      DO 5 K=1,100
      CALL PL(Z,N,POL)
      P=POL(NP1)
      DP=N*(Z*POL(NP1)-POL(N))/(Z*Z-1.D0)
      Z=Z-P/DP
      IF(DABS(P).LT.1.D-12)GOTO 15
  5   CONTINUE
      WRITE(6,1000)L
      RETURN
  15  X(L)=Z
      V=2.0D0/((1.0D0-Z*Z)*DP*DP)
      W(L)=V
      IF(L.EQ.M) GOTO 30
      DZ=Z
      IF(L.GT.1)DZ=(X(L)-X(L-1))*.5
      DO 17 K=1,200
      Z=Z+DZ
      CALL PL(Z,N,POL)
      P=POL(NP1)
      Z1=Z+DZ
```

```
      CALL PL(Z1,N,POL)
      P1=POL(NP1)
      IF(P*P1.LT.0.0D0)GOTO 18
   17 CONTINUE
   18 Z=(P1*Z-P*Z1)/(P1-P)
   20 CONTINUE
   30 DO 40 NEG=1,N
      IF(NEG.LE.M)Y(NEG)=-X(M+1-NEG)
      IF(NEG.GT.M)Y(NEG)=X(NEG-M)
      IF(NEG.LE.M)WY(NEG)=W(M+1-NEG)
      IF(NEG.GT.M)WY(NEG)=W(NEG-M)
   40 CONTINUE
      RETURN
 1000 FORMAT(5X,'FAILURE TO GET ZEROS OF LEGENDRE FOR ',I3)
      END
*
**********************************************
      SUBROUTINE PL(X,L,POL)
c     Computes Legendre polynomials of order zero to order
c     L for a given argument [ x=cos(theta) ].
c
      DOUBLE PRECISION S,X,POL
      DIMENSION POL(201)
      POL(1)=1.0D0
      POL(2)=X
      IF(L.LE.1)GOTO 20
      DO 10 JJ=2,L
      S=JJ
   10 POL(JJ+1)=((2.D0*S-1.D0)*X*POL(JJ)-(S-1.D0)*POL(JJ-1))/S
   20 RETURN
      END
c**********************************************
```

VITA

Jinseok Cha was born in Seoul, Korea, on May 20, 1963, the first child of JinGoo Cha and Jungki Lee. He graduated from the Kyung-gi High School in February 1982. He became a physics student at the Soong-sil University, Seoul, Korea, in March 1982 and graduated with an Physics (major) and Mathematics (minor) B.S. degree in February 1988. Within that period, he accomplished his military duties for two years. In January 1992, he began graduate studies at Hampton University, Hampton, Virginia which awarded a Ph.D. degree in Nuclear Physics as of December 2000. In 1995, he was married to Jungran Cho. They have three children, Songhee, Jamin, and Sujung Cha. He and his family currently live in Hampton, Virginia.